

Ice crystal classification using two dimensional light scattering patterns

Christopher James Stopford

Submitted to the University of Hertfordshire in partial fulfilment of the requirements of the degree of PhD

February 2010

Table of Contents

Abstract.....	4
Acknowledgements	5
List of acronyms	6
1. Background and fundamentals	7
1.1. Diffraction	7
1.2. The inverse scattering problem.....	8
1.3. Cirrus & ice crystals.....	10
1.3.1. Classification.....	10
1.3.2. Presence and formation.....	10
1.3.3. Detection and sensing of cirrus	11
1.3.4. Halos.....	13
2. Methods for calculation of light scattering by small particles.....	13
2.1. Mie Theory	13
2.2. Finite Difference Time Domain Method (FDTD)	13
2.3. Discrete Dipole Approximation (DDA)	13
2.4. T-Matrix Method	14
2.5. Geometric Optics (GO)	14
2.5.1. Improved Geometric Optics (IGO)	14
2.6. The Ray Tracing with Diffraction on Facets model (RTDF)	14
3. The Small Ice Detector Mark 2 and Mark 3.....	16
3.1. The SID-2 Instrument.....	16
3.2. Calibration of the SID-2 Detector Response	18
3.2.1. Electrostatic Ejection of Microspheres	18
3.2.2. Nebulising Aqueous Suspension of Microspheres	19
3.2.3. Discussion of Gain Calibration	19
3.3. The SID-3 Instrument.....	20
4. Ice Analogues	22
5. Laboratory equipment.....	23
5.1. Laboratory rig to capture 2D scattering patterns from ice analogues	23
5.1.1. Considerations of the camera.....	24
5.2. Comparison of lab measurements to RTDF	24
5.3. Data formatting from Cartesian images to polar arrays	27
6. The reference database & data manipulation	29

6.1. Conversion from RTDF to SID-2 analogous data.....	29
6.2. Interpretation of scattering patterns and rose plots	30
6.2.1. Intensity scaling	30
6.2.2. Orientation	31
6.2.3. Size and Aspect Ratio.....	35
6.2.4. Basal Indentation.....	37
7. Investigating the accuracy of fitting methods.....	40
7.1. Error calculations	40
7.2. Modelled test data.....	40
7.3. Fitting accuracy dependence on resolution of fitting space.....	41
7.4. Pie-Bubble plots.....	41
7.5. Orientation dependence of goodness of fit.....	43
8. Methods of comparing test data to the modelled reference database.....	45
8.1. Asymmetry Factor.....	45
8.2. Moment invariants	47
8.3. Direct Azimuthal Intensity Pattern Comparison	48
8.4. Fourier Transform Method	49
8.5. Comparison of fitting methods, data ranges and resolutions.....	49
8.6. Orientation determination.....	51
8.7. Effect of removing bins from azimuthal patterns	52
9. Case studies	53
9.1. Case Study: Compact column ice analogue.....	53
9.2. Case Study: Ice analogue Column	58
9.2.1. Comparison of modelled and measured scattering patterns.....	58
9.3. HALO 2 AIDA Cloud Chamber Campaign	62
9.3.1. Individual pattern analysis	63
9.3.2. Aggregated data analysis	65
9.3.3. Analysis of fitting saturated data.....	67
10. Summary and further work.....	69
Appendix A: Processes of the project.....	72
A. 1 Data acquisition	72
A. 2 Generation of reference database	73
A. 3 Fitting test data to a reference database.....	74
A. 4 Data processing graphical user interface	76
A. 4.1 “RTDF output processing”.....	76

A. 4.2 “Image processing”	77
Appendix B: Viewing of fitted results	77
Appendix C: Laser characterisation.....	80
List of figures	81
Bibliography.....	84

Abstract

An investigation is presented into methods of characterising cirrus ice crystals from *in-situ* light scattering data. A database of scattering patterns from modelled crystals was created using the Ray Tracing with Diffraction on Facets (RTDF) model from the University of Hertfordshire, to which experimental and modelled data was fitted.

Experimental data was gathered in the form of scattering patterns from ice analogue crystals with similar optical properties and hexagonal symmetry to ice, yet stable at room temperature. A laboratory rig is described which images scattering patterns from single particles while allowing precise control over the orientation of the particle with respect to the incident beam. Images of scattering patterns were captured and compared to patterns from modelled crystals with similar geometry.

Methods for introducing particles *en-masse* and individually to the Small Ice Detector (SID) instruments are discussed, with particular emphasis on the calibration of the gain of the SID-2 instrument. The variation in gain between detector elements is found to be significant, variable over the life of the detector, and different for different detectors.

Fitting was performed by comparison of test scattering patterns (either modelled or experimental) to the reference database. Representation of the two dimensional scattering patterns by asymmetry factor, moment invariants, azimuthal intensity patterns (AIP) and the Fourier transform of the AIP are compared for fitting accuracy. Direct comparison of the AIP is found to be the most accurate method. Increased resolution of the AIP is shown to improve the fitting substantially.

Case studies are presented for the fitting of two ice analogue crystals to the modelled database. Fitting accuracy is found to be negatively influenced by small amounts of surface roughness and detail not currently considered by the RTDF model.

Fitting of *in-situ* data gathered by the SID-3 instrument during the HALO 02 campaign at the AIDA cloud chamber in Germany is presented and discussed. Saturation of detector pixels is shown to affect pattern fitting. In-flight operation of the instrument involves the variation of gain of the whole detector (as opposed to individual elements) in order to obtain unsaturated images of both large and small particles.

Acknowledgements

I would like to extend my thanks to the following people for their enormous help and support throughout this project:

- Dr Z.J. Ulanowski (Principal supervisor)
- Dr E. Hesse (Secondary supervisor)
- Dr E. Hirst (Secondary supervisor)
- Mr K.Henman (SEM operation)
- My colleagues in the Science and Technology Research Institute of the University of Hertfordshire (Proff. P. Kaye, Dr R.Greenaway, Dr W. Stanley, D. McCall BSc, P.Czaban MSc, and J. Wootton MSc.)
- My partner Stephanie, and my family

Funding was provided by the Natural Environment Research Council in the form of a PhD studentship.

Ice crystal data was recorded at the AIDA cloud chamber, Forschungszentrum, Karlsruhe, Germany. Special thanks to Dr M. Schnaiter and Dr. Ahmed Abdelmonem.

List of acronyms

Af	Asymmetry Factor
AIP	Azimuthal Intensity Pattern
AR	Aspect Ratio
CCD	Charge-Coupled Device
EM	Electromagnetic
FFT	Fast Fourier Transform
GO	Geometric optics
LIDAR	Light Detection And Ranging
PAD	Projected Area Diameter
RADAR	Radio Detection And Ranging
RMS	Root Mean Square
RTDF	Ray Tracing with Diffraction on Facets
SEM	Scanning Electron Microscope
SID	Small Ice Detector
SVM	Support Vector Machine
WMO	World Meteorological Organisation

1. Background and fundamentals

This introductory chapter introduces the project and the current state of research in its subject area. The reasons for the investigation will be discussed, and shortcomings of current knowledge highlighted.

Classification of ice crystals in cirrus and mixed phase clouds is the subject of much interest. Cirrus covers a significant proportion of the earth's surface at any given time, yet the radiative properties of cirrus are still largely uncertain. This is because current climate models do not have access to suitable information on the constituent ice crystals. *In-situ* data is now being collected from a variety of instruments, including those that measure the forward scattering pattern of atmospheric particles.

The two dimensional forward scattering pattern contains a significant amount of information about a particle, but the inverse scattering problem remains a challenge. A complete reconstruction of a particle from scattered light would require the recording of intensity and phase information from all angles. This would be difficult to obtain in a laboratory, and is currently impossible *in-situ*, except in limited form in the case of holographic probes [1],[2]. Current probes, particularly the *Small Ice Detector* (SID) range (which will be discussed in more detail in chapter 3), only capture a small proportion of the forward scattering, and so classification into some pre-defined groups based on morphology and size is a reasonable expectation.

The primary aim of this project is to investigate methods of recovering some information on the size and shape of an individual crystal from its forward scattering pattern. Data has been collected *in-situ* using the SID-2 and SID-3 probes, laboratory and modelled data.

Modelling of scattering from single orientations of crystals is achieved using the Ray Tracing with Diffraction on Facets (RTDF) model from the University of Hertfordshire.

1.1. Diffraction

The study of modern optics is often said to begin with Alhazen of Basra in the 11th century. Alhazen developed an understanding of light by experimentation with pinhole imagery, and refraction in the atmosphere. He correctly refuted the accepted understanding of human vision [3]. At the time, it was believed that the eye was the source and receptor of light.

Later, Da Vinci famously wrote in 1490 about the effect of diffraction on small particles (such as smoke or water) being responsible for the sky being blue [4]. Diffraction was first described as the deviation from the path of propagation when passing an obstruction by Francesco Grimaldi (1618-1695) [5] who observed qualitatively that light did not rigidly conform to the corpuscular theory. It was not until Young (1773-1829) performed his famous experiments on the interference of light [6] that wave theories became more popular, and eventually lead to our current understanding of the dual nature of light.

One challenge faced by those investigating light scattering is to identify the scattered light distribution from a defined scattering object – the *direct* scattering problem. Hecht [5] defines diffraction as below:

A deviation of light from rectilinear propagation. The effect is a general characteristic of wave phenomena occurring whenever a portion of a wave front, be it sound, a matter wave or light, is obstructed in some way.

Christiaan Huygens (1629-1695) presented a principle of wave propagation that is described by Born and Wolf [7] as:

Every point on a wave-front may be considered as a centre of a secondary disturbance which gives rise to spherical wavelets, and the wave-front at any later instant may be regarded as the envelope of these wavelets.

Thomas Young (1773-1829) observed the manner in which waves interfere to produce fringes with his famous ‘dual slit’ experiment. In his original work [8] he in fact used a pair of pinholes to observe interference fringes. Augustin Fresnel used this information to expand Huygens’s principle adding that the wavelets interfere with one another, and that secondary wavelets are of the same frequency as the primary. This is now known as the Huygens-Fresnel principle.

1.2. The inverse scattering problem

The retrieval of information about a scatterer by analysis of the associated scattered light is referred to as the *inverse scattering problem*. It has been likened to the identification of an animal from the tracks it leaves behind [9]. Due to the remote and non-destructive nature of measuring optical disturbance, the applications for solving this problem reach far and wide. The type of data that can be recovered depends upon the method of acquisition, and knowledge of the forward problem. Previous methods of airborne particle analysis tend to involve collecting and analyzing a sample *ex situ*, which would clearly be a complex if not impossible procedure when dealing with cirrus clouds.

By analogy with holography, for a complete inverse solution from the scattering to the scatterer, the complete scattering and phase profile would have to be known, including the phase of the scattered wave. Since in most situations this is not available, and is in fact difficult to obtain even in a laboratory, an approximation or grouping into a range of similar scatterers is often the realistic outcome, as is the case in the remit of this project.

The benefits of classification by observation of scattered light extend over many disciplines – from meteorology to astrophysics, via biology, engineering and geology.

By determining the nature of blood cells, some information can be recovered about the health of an individual. For example, “blood count” is the term used to describe the ratio of different types of blood cell. Initially, this was performed by complex and labour intensive laboratory work which was difficult to reproduce – usually involving a slide, microscope and skilled operator to manually count cells. Latterly, some degree of automation has allowed this process to be made more precise, largely due to the identifiable features of different types of blood cell scattering observed during flow cytometry – a technique which measures scattered light from single blood cells at forward and side angles as well as fluorescence [10]. Forward scattering gives an idea of the cell size, while the side scattering gives a measure of complexity. Further information can be derived by observing the fluorescence once suitably illuminated. This method can be used to rapidly identify such diseases as diabetes by detecting the aggregation of platelets in blood plasma [11].

An advantage that such methods enjoy is the opportunity to prepare a sample prior to testing. By means of such techniques as centrifugation, samples can be roughly selected by particle size.

To provide an example of classification by light scattering, Banada et al. [12] have developed an instrument which uses a laser line scanner to provide the forward scattering from a culture of bacteria on a Petri dish. A 2D image is collected of the scattering, which is then described using Zernike moments¹ to describe the form, and Haralick features² to describe the texture. A support vector machine (SVM) was then used to discriminate between types of bacteria based on the features mentioned above. For the remit of this thesis, the Haralick features are redundant, since they relate to texture detail that is not captured by the SID-2 instrument. They may however be of value in future work with the SID-3 instrument, although will not be discussed herein.

Not all useful light scattering techniques are reliant on results from single particles. As an example within the theme of medical physics, the scattering of near infrared light from tissue can inform the observer of the location of a boundary between oxygenated and deoxygenated tissue [17].

Observation of scattering from particles has been used to size particles in the interplanetary space within our solar system, although since one is limited in the range of observable scattering angles from distant space born particles [18-20], polarization measurement supplements much of the observation.

Other uses of single particle scattering include sizing of sub micron smoke particles, where Chung et al [21] monitored the scattering intensity at 60° and 120°, comparing empirical data with Mie theory [22]. This brings up an interesting point, that with limited azimuthal resolution, the non-sphericity of a single particle would create a large error in sizing. However, for a multitude of randomly orientated particles, this will be azimuthally averaged, giving a reasonable measure of the average size particles in the sample.

For examples of the use of scattered light from groups of particles, one might look to lidar (LIght Detection And Ranging) as an example with a wide remit. In its most basic form, it can be used simply to determine the distance from the transceiver of an optically reflective object. This has seen success in recording data about such geographic features as forests, and ice sheets from both airborne and satellite based instruments [23-26].

The inverse problem requires consideration in other fields of study also, such as the remote sensing of precipitation which can be performed with radar, comparing the reflected intensity of vertical and horizontal polarizations [27].

¹ Zernike moments are derived from a set of radial polynomials. They are invariant to image scale, rotation and translation. Scale and translation are unimportant to this project; however rotational invariance will be discussed in later chapters. Using the derived moments, an image can be represented using relatively few data points, with no redundancy or overlap. These can then be weighted and compared to reference data, or used to reconstruct the original image to a degree of accuracy dependant on the number of moments used [13]. Further discussion can be found in 8.2 - Moment invariants.

² Haralick features were introduced by Haralick et al in 1973 [14] as an easily computable set of measures of grey-tone spatial distribution. The features consist of the probability that a given pixel intensity i is adjacent to a pixel with intensity j over all pixels and intensities. They have been successfully used in such varied applications as classification of pollen [15] and identification of breast lesions [16].

The required information to be determined by solving the inverse problem is largely dependent on the situation. For example, the *scattering coefficient* (i.e. the effective cross section of scatterer per unit volume) of sea water is used to estimate the mass of marine particles in suspension [28]. The ratio of perpendicular and parallel polarization intensities of light has enabled the estimation of particle size in the atmosphere of Saturn's moon, Titan [29] and two dimensional forward scattering can be used to identify particular particle types, such as airborne asbestos [30].

1.3. Cirrus & ice crystals

1.3.1. Classification

Luke Howard (1772-1864) has been hailed as the creator of our current system of cloud classification. Although others had tried before him, his use of Latin allowed the schema to be internationally adopted. In his fifth of seven lectures [31], he said about cirrus:

If we examine minutely the high region, especially after a clear time of some continuance, we shall perceive that it is often occupied by threads or locks and feathers of cloud, descending from above. These form what is called the Cirrus, (a Latin word denoting a lock of hair,) and they are capable of increasing, without any change in aggregation, till they also fill the sky by themselves.

The World Meteorological Organisation (WMO) has since been made responsible, by international agreement, for defining the classification of clouds. The WMO's definition of cirrus is detailed below [32]:

Cirrus: *Detached clouds in the form of white, delicate filaments or white or mostly white patches or narrow bands. These clouds have a fibrous (hair-like) appearance, or a silky sheen, or both.*

Cirrocumulus: *Thin, white patch, sheet or layer of cloud without shading, composed of very small elements in the form of grains, ripples etc., merged or separate, and more or less regularly arranged; most of the elements have an apparent width of less than one degree.*

Cirrostratus: *Transparent, whitish cloud veil of fibrous (hair-like) or smooth appearance, totally or partly covering the sky, and generally producing halo phenomena.*

It is interesting to note that the classification is devoid of any reference to their composition, but is based entirely upon the visual properties noted by Howard. There exists another type of cirrus, identified by its low optical thickness (<0.03 at $0.694\mu\text{m}$), called *subvisual cirrus*. The optically thin nature makes it particularly difficult to detect passively. They are usually higher, and colder than other forms of cirrus, but similar in that they consist primarily of hexagonal ice crystals in various habits.

1.3.2. Presence and formation

Cirrus clouds are formed by warm air being forced higher into the atmosphere, causing adiabatic cooling. This is often at the leading edge of a warm front, or some geological obstacle. Ice nucleation is observed once temperatures fall below -20°C (which occurs at 5.4km according to the International Standard Atmosphere [33]). Nucleation can occur heterogeneously, whereby it occurs on some aerosol particle, such as mineral dust, or homogeneously whereby water spontaneously freezes. The latter requires lower temperatures of around -40°C . Heterogeneous ice formation occurs with relative humidity with respect to ice much lower than is required for homogeneous formation. There are many factors shown to influence heterogeneous

nucleation, such as temperature, rate of ascent or air parcel, relative humidity and nucleus type, size and structure [34].

Once ice has begun to form, crystals grow due to the deposition of water vapour onto the surface of crystals. The hexagonal crystalline structure of water ice leads to the hexagonal columns and plates that are abundant in cirrus. Rosettes are formed of columns growing from a common centre in different directions, each with hexagonal cross-sections. Complex crystals can also form by aggregation.

Crystal concentration is often observed at much higher concentrations than the available ice nuclei. The explanation for this comes from the Hallett-Mossop process, which describes how ice crystals are formed by the splintering of graupel pellets. Graupel is formed by the riming of supercooled water droplets. As the graupel moves through air, splinters form and break loose which then grow into crystals by vapour deposition, or undergo riming and form graupel [35].

Aircraft contrails (abbreviated from *condensation trail*) are also considered to be a form of cirrus, since they too are formed of ice crystals. Exhaust gasses from aircraft engines are moist and warm relative to the surrounding air. Nuclei in the exhaust enable formation of droplets which quickly freeze [32]. They may exist for hours after the passage of the aircraft, spreading out over time.

Despite not always being visible to the naked eye, cirrus is surprisingly ubiquitous. It has been estimated that 30% of the surface of our planet is covered by these optically thin clouds, extending to 50% in the tropical regions [36]. They are more abundant in the summer season of each hemisphere. It has long been known that the crystals comprising these clouds are highly non-spherical [37], with an average of 30% of these being column or plate type hexagonal crystals [38].

1.3.3. Detection and sensing of cirrus

Sensing of cirrus and other atmospheric phenomena can be difficult due to the range of scales involved. Clouds may cover many miles, yet details of the microscopic constituents are of as much interest as the macroscopic traits. For this reason, it is possible to divide this section into two, and consider each method independently.

1.3.3.1 Remote

Remote sensing of cirrus depends primarily on satellite, LIDAR and RADAR equipment. The advantage of remote sensing is that a large area can be observed at once, without the need to reposition equipment.

Meteorologists were amongst the first to make good use of orbiting satellites after the first successful such instrument was launched by the USSR in 1957. In 1959, the Explorer VII instrument was launched to measure the radiation balance of the Earth and its atmosphere [39]. This was shortly followed by Vanguard 2 in 1959 which measured the cloud-cover for a short period and continues to measure the atmospheric density to this day [40]. It was succeeded by TIROS-I (Television and InfraRed Observation Satellite) in 1960.

These satellites paved the way for what is arguably the pinnacle of remote sensing so far: the A-train – a series of five satellites designed to return information on precipitation, cloud cover, aerosols, polarized radiation, ozone layer, air quality, and more [41].

Satellites in general, with a few exceptions, are passive instruments – observing EM radiation reflected by the Earth or the atmosphere. In contrast, ground based remote observation instruments such as LIDAR or RADAR emit EM radiation and observe the effect on the scattered signal.

Other than the wavelength of the EM radiation used, these methods are largely similar. LIDAR uses wavelengths of the order of a micrometer, and RADAR of centimetres.

1.3.3.2 *In Situ*

In situ measurements began with Weickmann [42] who used lacquer coated slides to collect imprints of ice crystals from an open cockpit aircraft. These showed remarkably clear images of hexagonal ice crystals ranging from plates and columns to aggregates and rosettes. Since then, a range of other airborne instruments have been developed to collect information about cirrus *in situ*, such as the Cloud Particle Imager [43], Video Ice Particle Sampler [44] and PHIPS [45] which all image a crystal directly. This method gives tremendously useful information for larger crystals, but the accuracy falls off sharply for smaller particles due to resolution constraints. Also, surface detail is often un-resolvable. Probes such as the Small Ice Detector range of instruments are well suited to retrieving information from those particles that cannot be directly imaged, since they record the scattered light from a particle. This will be discussed further in Chapter 3.

Instruments using CCD detectors are able to image at a higher resolution than instruments with parallel readout detectors, however the latter are able to sample at a much higher rate.

Some useful information regarding a selection of instruments currently in use is briefly summarised in Table 1. The inlet type is declared as open for instruments such as SID-2, or closed for those more likely to cause crystal shattering, such as SID-1.

Instrument name	Size range	Frequency	Inlet	Description of instrument
2 Dimensional Particle Size Spectrometer (2DC)	50-800 μ m	5Hz	Open	Shadowgraph is recorded on a linear array of 32 pixels as a series of intensity readouts as particle passes through beam [46]
Cloud Droplet Probe (CDP)	2-50 μ m	0.1-10Hz	Open	Intensity of laser light scattered from 4-12 $^{\circ}$ used to assign individual particles to one of four sizing bins [47]
Cloud Particle Imager (CPI)	>10 μ m	~2000Hz	Narrow	Direct imaging of up to 75 frames per second, and 25 particles per frame at 2.3 μ m resolution [48]
2D-S (Stereo) Probe	>10 μ m	50Hz	Open	Two shadowgraphs captured on 128-photodiode linear arrays from orthogonal directions [48]
Fast Forward Scattering Spectrometer Probe (Fast-FSSP)	2-100 μ m	50kHz	Narrow	Scattering from 3-12 $^{\circ}$ used to size particles into 255 bins [49]
SID-1	1-100 μ m	10kHz	Narrow	6 detectors arranged azimuthally record spatial information scattering at 30 $^{\circ}$ [50]
SID-2	5-100 μ m	10kHz	Open	24 azimuthally orientated photodiodes between 9-20 $^{\circ}$ and an inner ring of 3 pixels at 7-9 $^{\circ}$ capture 2D forward scattering information
SID-3	1-100 μ m	20-25Hz	Open	CCD array of 780x582 pixels images 2D forward scattering information

Table 1 - Useful information regarding other *in situ* particle probes

It is an interesting point of note that very little exists in the literature in the way of accurate characterisation of these instruments, and instruments like them. Where such characterisation exists, they confirm the need for detailed investigation [46],[48],[50].

1.3.4. Halos

Halos are a phenomenon unique to cold clouds, since they form due to the hexagonal nature of the water ice crystals. Halos are more often observable than they are observed. Once one is aware of their existence, and knows where to look, they will be noticed more often. The most common halo is the 22° one, followed by the 46°. The latter is generally somewhat less bright, and more difficult to observe.

The 22° halo is caused by rays passing through two prismatic (side) facets of a hexagonal prism experiencing the minimum angle of deviation for the prism (Figure 1, left). The halo is formed because a high intensity of scattered light is refracted through this minimum angle of deviation. This also leads to the phenomenon known as a sundog. This is similar to a 22° halo, but only forms bright patches either side of the sun. These form when the sun is low in the sky, and plate crystals are aligned with their basal facets horizontal. This is in contrast to the halos caused by randomly aligned particles.

The same effect produces the dimmer 46° halo, although a different ray path is responsible - Figure 1, right.

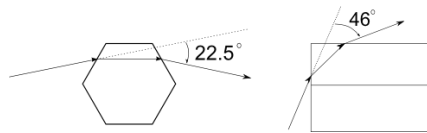


Figure 1 - The ray paths which cause 22° (left) and 46° (right) halos [9]

2. Methods for calculation of light scattering by small particles

This section will look at some of the frequently used methods of calculating scattering, and identify the area of applicability of each.

2.1. Mie Theory

Independently derived by Love (1899), Gustav Mie (1908), Ludvig Lorenz (1890) and Debye (1909) (Michael I. Mishchenko, 2000). This method solves the spherical wave equation using a separation of variables method with boundary conditions set at the surface of the scatterer. It has since been extended and applied to modified spheres, such as those with concentric layers, and also to cylinders and homogeneous isotropic spheroids. The size of the particle in question can be, up to a size parameter³ of thousands [51].

Although an exact method for spheres, this method is not a good approximation when dealing with faceted ice crystals.

2.2. Finite Difference Time Domain Method (FDTD)

This is an approximate method which directly solves Maxwell's equations [52]. The particle may be arbitrarily shaped, although approximate boundary conditions are assigned to it. Electric and magnetic fields are calculated over discrete time intervals, for a grid of spatial points.

2.3. Discrete Dipole Approximation (DDA)

Originally by Purcell & Pennypacker [53] the method assumes that a given particle is divided into a number of discrete dipoles, usually of the order of 10s per wavelength. The state of the dipoles initially is known, and

³ The conventional method for assessing the size of a particle is the *size parameter* - defined as $\chi = 2\pi a \div \lambda$ where a is the effective radius of the projected area of the crystal, and λ is the wavelength of incident light.

subjected to an EM field. The exiting field is the superposition of the field from each dipole and the external field.

Although applicable to arbitrarily shaped particles, DDA is computationally expensive, and limited to very small size parameters.

2.4. T-Matrix Method

The Transformation Matrix (T-matrix) method was developed by Waterman [54]. It is so called, because it uses a transformation matrix to relate the coefficients of the vector spherical wave functions of incident to scattered light. A nice feature of the T-matrix method is that it reduces to Lorenz-Mie theory for spheres. One of the main advantages of T-matrix is that it can in principle be applied to arbitrary shaped particles. However, as the complexity of the scatterer increases, the accuracy decreases, and the computational requirement increases rapidly. Computation time also increases at a rate greater than linear with respect to size parameter [55].

2.5. Geometric Optics (GO)

Geometric optics is an approximate method that assumes that the incident plane wave can be represented as a collection of independent parallel rays. The laws of Snell and Fresnel then describe interaction of the rays with the particle. This provides a good approximation when the size of the particle is very large in comparison to the wavelength [56]; performs poorly for smaller size parameters. Diffraction is not considered by GO.

2.5.1. Improved Geometric Optics (IGO)

To increase the accuracy of GO, Muinonen [57] introduced an improvement to GO that determines the electric and magnetic fields at the surface of the scatterer, from which the far field is derived. This improves the accuracy, and brings the applicability of GO down to size parameters of around 20 [58].

2.6. The Ray Tracing with Diffraction on Facets model (RTDF)

This section will detail the methods used in the RTDF model developed at the University of Hertfordshire. The model is used to compute scattering patterns from pre-defined crystal geometries in single orientations.

The RTDF model [59-61] traces a ray through a crystal, considering each facet essentially as a set of slits, each of which contributes to the direction of diffraction in proportion to the distance from the edge of the plane. For example, a ray passing through a rectangular facet will be deflected in two orthogonal directions – once for each pair of parallel edges. The formula for the deflection angle is derived from an asymptotic approximation of far-field scattering by a half-plane [59], namely Eq. 1.

$$\varphi = \arctan \left(\frac{\lambda}{4\pi^2 x} \right) \quad \text{Eq. 1}$$

Where φ is the far field scattering angle, λ is the wavelength of incident light, and x is the distance from the edge to the incident ray. For a parallel slit the formula takes the form shown in Eq. 2

$$\varphi = \arctan \left(\frac{\lambda}{4\pi^2} \left(\frac{1}{x} - \frac{1}{2a - x} \right) \right) \quad \text{Eq. 2}$$

where a is the slit half-width.

However, the above approximation overestimates forward scattering, and loses accuracy for particles with size parameters below about 50. To determine the deflection angles more accurately, the electric field between two half planes (i.e. in the slit) is considered. As per Prosser's approximation [62], this is considered to be the sum of the electric fields of the individual planes minus the electric field in free space.

Once the electric field is calculated, the energy flow lines and far field deflection angles of these lines are calculated. The far field deflection angle is a best fit function of slit width, angle of incidence and distance from the edge of the slit.

Using this method the first order minima and the zeroth order maximum are accurately represented, as is the envelope for angles beyond the first minima. [60]

The calculated diffraction angle of a ray passing through a facet is multiplied by the sine of the angle between the diffracting facet and the adjacent facets. This eliminates diffraction between coplanar facets, while maintaining the full diffraction angle for perpendicular facets. Such a modification permits the modelling of scattering from particles with curved surfaces, such as spheres, ellipsoids or cylinders [63].

To summarise, RTDF is a relatively recently developed method of calculating the scattering from a particle in a single orientation. It has the advantage of being computationally inexpensive while remaining accurate at size parameters well below that of GO. For high size parameters, it becomes equivalent to GO. No other methods are able to compute the scattering from complex particles in the size parameter range of interest to this project, while maintaining sufficient speed and accuracy.

3. The Small Ice Detector Mark 2 and Mark 3

The Small Ice Detector Mk2 is an instrument developed at the University of Hertfordshire for the purpose of gathering 2D light scattering data from in situ single cloud particles. This chapter will describe the form of the instrument, the calibration and use of data.

3.1. The SID-2 Instrument

The SID-2 instrument is designed to be mounted on an aircraft. It consists of a cylindrical core of electronics headed by a probing arm (bottom right of Figure 2) and a detector mounted in the head (top right of Figure 2.) The instrument is capable of sampling ~9000 particles per second, limited by the speed of the electronics.

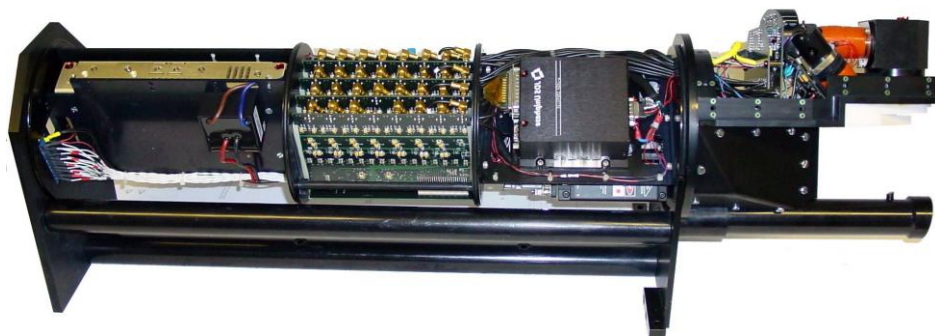


Figure 2 - SID-2 Instrument with electronics exposed.

Two dimensional forward scattering is recorded from individual particles. As a particle enters the scattering volume (Red arrow, Figure 3) scattered light is detected by the trigger detectors (blue lines). Each trigger is focused on a small volume within the beam. These partially overlap to define a scattering volume. Recording of the forward scattering by the main detector is initiated only when a peak is detected on both triggers simultaneously – i.e. when a particle is in the scattering volume.

The scattering volume has a cross sectional area of 0.88mm^2 for crystals around $25\mu\text{m}$ [64], which limits the likelihood of multiple particles in the scattering volume at the same time to campaigns in all but the most dense of clouds. Data can be captured for particles down to around $3\mu\text{m}$. The dynamic range of the SID series of instruments is about 200.

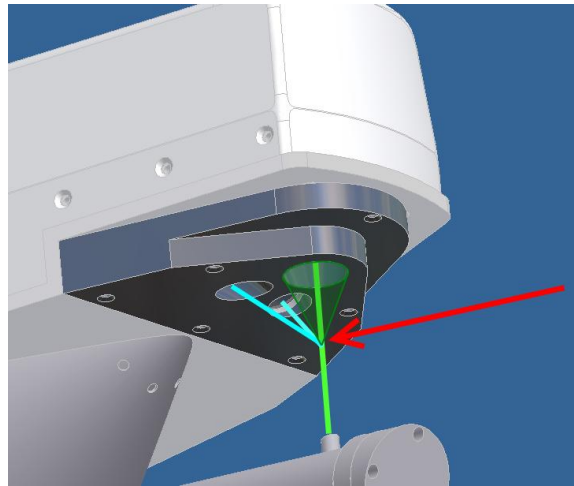


Figure 3 - Diagram of SID-2 optical path. Red arrow indicates the incoming particle. Light blue lines indicate the path from scattering volume to trigger detectors. Green cone indicates the captured forward scattered light.

In the original implementation a hybrid photodiode detector is used, consisting of a set of 24 azimuthally distributed pixels in an ‘outer’ ring, and another six paired within these forming an ‘inner’ ring of three pixels (Figure 4, left). This enables capturing of azimuthal and some radial information. A limitation of this detector is that each pixel has a slightly different gain value, which must be characterised prior to analysis (more on this in section 3.2.3.)

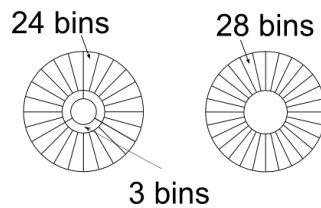


Figure 4 - SID-2 (left) SID-2H (right) detector layouts showing inner and outer rings of azimuthal bins

The inner ring captures scattered rays between 5.5° - 9° elevation angled, and the outer ring between 9° and 19.8° .

For this project, the inner ring of the SID-2 detector is not used at all. The data in the outer ring is referred to as the *azimuthal intensity pattern* (AIP).

As this document was being written, an upgrade to the SID-2 instrument was taking place. This involved replacing the hybrid photodiode detector with a multi-element photomultiplier linked via an optical fibre bundle, and with a similar azimuthal distribution as is currently in use. Unlike the earlier detector there is no inner ring, but instead four extra azimuthal elements, bringing the total number of bins to 28 – see Figure 4, right. The polar range is identical to that of the SID-2 outer ring. This arrangement is characterized by much smaller gain variability (discussed in section 3.2.3). Analysis of the effect of increasing azimuthal resolution will be covered in a later chapter. The detector allows data from smaller particles to be recorded ($\sim 1\mu\text{m}$). The dynamic range, sensing volume and bit depth of recorded data are all similar to SID-2.

Large ice particles are prone to shatter prior to image collection on probes with narrow inlets or detection volumes close to the surface of the probe [65]. For this reason, the SID-2 and 3 probes have a very open path to the detection volume.

3.2. Calibration of the SID-2 Detector Response

In order to retrieve meaningful results, the gain of the detector elements must be identified and corrected for. The gain can be defined as the ratio of a pixel response to the flux through the pixel. In order to normalise the response of the detector, it is necessary to quantify the gain for each pixel. This could be performed by illuminating each pixel equally and normalising them against each other.

However, illuminating the SID-2 detector evenly is non-trivial since the instrument only records the response while a particle is in the scattering volume. For this reason, spheres were introduced to the scattering volume, since the 2D scattering pattern produced by spheres is rotationally symmetric about the optical axis.

Two methods of introducing spheres into the scattering volume of the SID-2 instrument were tested – electrostatic ejection of individual spheres from a needle, and nebulisation of a large number of spheres. The benefits and drawbacks of each method are discussed below.

3.2.1. Electrostatic Ejection of Microspheres

Firstly, individual spheres were collected on a needle⁴ and suspended directly above the scattering volume. A potential difference was then applied between the needle and a SEM grid directly below the scattering volume, propelling the crystal towards the grid. The SEM grid is a fine meshed (3 μ m) grid of copper, employed for its conductivity. The spacing of the grid is small enough that the spheres would not pass through. The electric field accelerates the sphere through the scattering volume, triggering detection and data acquisition.

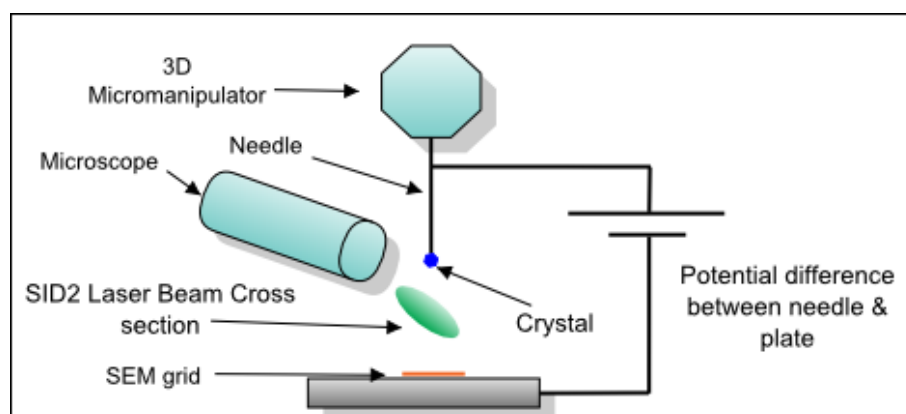


Figure 5 - Electrostatic Ejection setup: Crystal is ejected from needle to SEM grid through the scattering volume of the SID2 laser while being observed by microscope

The advantage of this method is that the particle⁵ can be measured, either with an optical or scanning electron microscope, before being ejected. Additionally, the particle can be recovered occasionally, although in practise this is only true approximately 30% of the time. The main benefit of this method however is that

⁴ By bringing a needle into contact with the sphere, the sphere can be lifted off the surface of a slide, due to attraction forces.

⁵ This method has been successfully applied to ice analogue crystals and atmospheric mineral dust as well as microspheres.

there is just one particle in the scattering volume during any given trigger event, and no supporting hardware is involved in the scattering.

3.2.2. Nebulising Aqueous Suspension of Microspheres

The second method involved using a nebuliser to disperse a suspension of spheres in a mix of ethanol and the fluid in which they are supplied. Once nebulised, the spheres are passed to a drying chamber where they are suspended long enough for any remaining fluid to evaporate. Filtered air is then pumped into the chamber, forcing the spheres out through a nozzle into the scattering volume of the SID-2 detector.

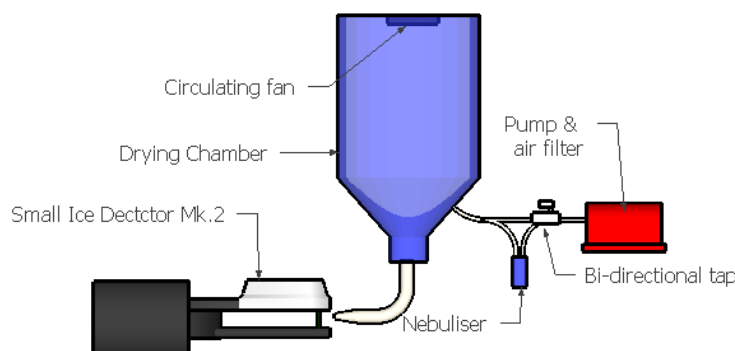


Figure 6 - Laboratory setup used to nebulise a suspension of microspheres for calibration of SID-2 detector

The advantage of this method is that a much larger sample can be recorded over a short period of time. Unfortunately, the likelihood of individual spheres triggering the detector is reduced by a tendency of the spheres to stick together in clusters. It is also possible that due to the airflow, such bundles may be aligned in some manner, which would bias the result. It has also been observed that the fluid in which the particles are supplied leaves a residue on the surface of the particle, which distorts the scattering pattern. For individual particles, it is possible to reduce this phenomenon with a series of ethanol rinses on a slide, but it is clearly not possible to do this for nebulised spheres.

3.2.3. Discussion of Gain Calibration

The response from the electrostatic ejection experiment showed that the gain difference between detector elements was significant. The expected result for an equal gain per detector element for spherical particles would be an equal response; however this was not the case. For a given set of spheres, the response varied between about 40 and 160, as can be seen in Figure 7. Furthermore, the gains have been observed to change significantly over the lifetime of the SID-2 detector [66].

The importance of accurate determination of the detector gain stems from the fact that the relative difference in intensity between detector elements holds the information required for classification. Without correction, significant differences between modelled and empirical data would exist. All data quoted in this document have been corrected for the gain variation.

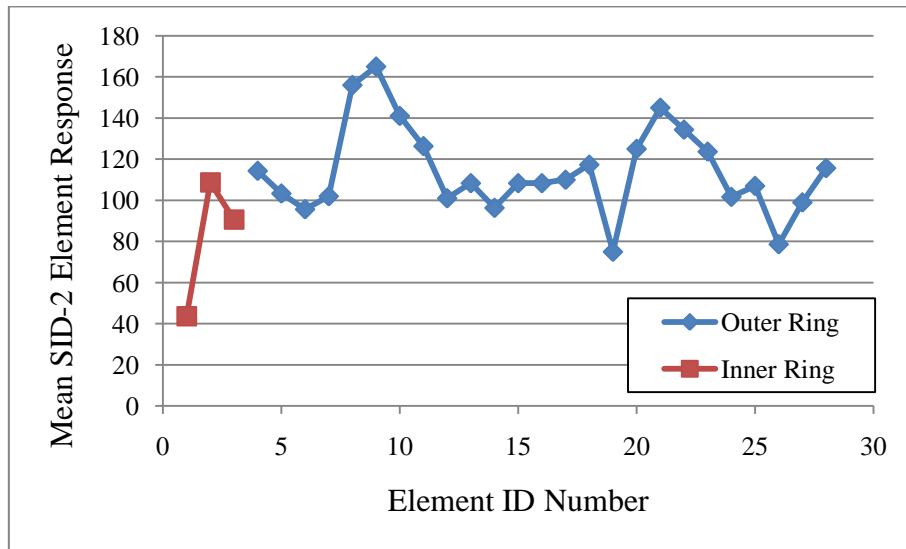


Figure 7 – Mean response of SID-2 instrument to spherical particles

Averaging of large numbers of randomly orientated spherical or non-spherical particles (such as *in situ* cloud chamber or in-flight data) is a useful manner in which to determine the gain of the instrument. However, it should be noted that due to particle alignment in laminar flows, an error is introduced. This was observed during the nebulising experiment with clusters of spheres.

3.3. The SID-3 Instrument

The next iteration of the *Small Ice Detector* range of instruments consists primarily of a laser of increased power, and a detector in the form of an intensified CCD. The CCD has a resolution of 780x582, which can observe scattering angles between about 6.8° and 25.5° from the optical axis. CCDs are much slower to record data than the photodiodes of SID-2 instruments which lowers the number of particles that can be imaged per second to 30 per second (currently limited to 20-25s⁻¹ by the rate images can be saved to disk); however the trigger detectors record each trigger in the same manner as SID-2. Other similarities to SID-2 include the dynamic range, the physical layout of triggers and detector, the open path of the instrument and the sensing volume.

The instrument fits into the same type of canister as the SID-2 probe for use on aircraft, and another version has been modified for laboratory use [67]. In addition, data can either be sent via Ethernet link to a remote PC, or stored internally on a Microsoft Windows XP based single-board computer.

It is worth pointing out that the larger maximum scattering angle will now allow including the 22° halo in the recorded scattering pattern. The effect of this on fitting will be discussed later in this thesis.

For the purposes of modelling, the range of effective angle will be reduced and rounded to 7°-25°. This allows for the roughness of the SID-3 beam stop and aperture to be truncated.

The increased resolution of the SID-3 detector gives a much clearer idea of the shape of particles. At the radius of the beam stop, there is approximately 0.7° between pixels in the azimuthal direction, and 0.2° at the outside. In the polar direction it is 0.1° .

4. Ice Analogues

Working with ice crystals is inherently difficult. Maintaining the appropriate temperature and water vapour pressure to grow water ice crystals of the desired morphology is a technically demanding and time consuming and imprecise process [68]. Thankfully, an alternative is available in the form of ice analogue crystals, developed by Ulanowski et al. [69]. These analogues are stable at room temperature, form similar habits as ice, and have a refractive index comparable to ice ($1.310-1.315 \pm 0.002$ at $612\mu\text{m}$). They are also strong enough to be easily manipulated using sharpened tungsten needles. Figure 8 shows a selection of crystals imaged by *scanning electron microscopy* (SEM). Optical microscopy was used to measure the crystal's dimensions, while SEM allowed detailed examination of the surfaces and symmetry of the crystals. Note that the cross section of the crystals is hexagonal similarly to ice. Image *d* shows an indentation in the basal facet of the crystal. The exposed surface is the side of the crystal which was in contact with the petri dish in which it was grown.

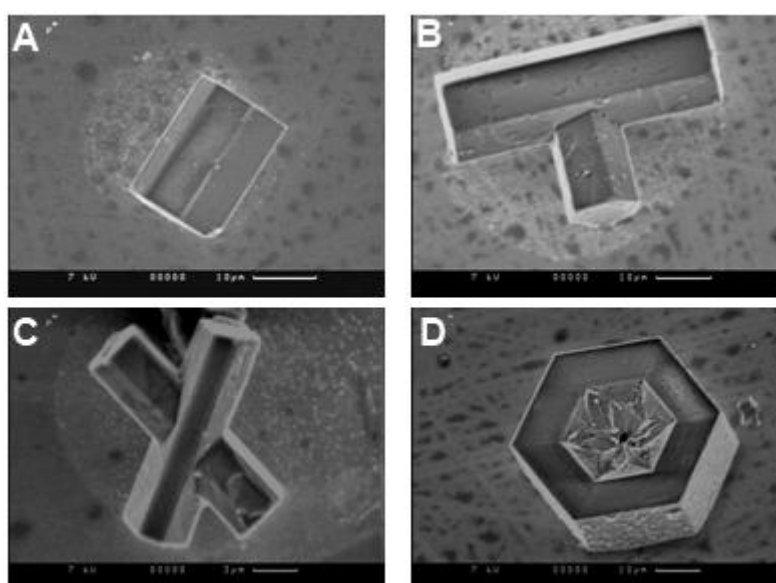


Figure 8 - A selection of ice analogues imaged by SEM

Ice analogue crystals are resistant to pressure and temperature, allowing them to be manipulated with a micromanipulator under intense illumination without concern. They also adhere to glass and Perspex, enabling the user to rotate the plate without the crystal falling off. This bond is not so strong as to resist rapid air flow however.

An alternative to using ice analogues is stretched glass rods [70]. This involves polishing a glass rod until its cross-section is hexagonal, then heating until it is viscous enough to stretch while maintaining the cross section. However, this method does not reproduce such morphologies as rosettes, or basal indentations and as such is not as versatile as using analogues. Also, the refractive index differs from that of ice in air, so the glass would have to be submerged in water during measurements.

5. Laboratory equipment

In order to obtain experimental data in the form of scattering patterns, and data from the SID-2 instrument, customised laboratory rigs were used. This chapter will describe the design and implementation of such equipment.

5.1. Laboratory rig to capture 2D scattering patterns from ice analogues

This section describes the hardware and set-up of the laboratory equipment designed to capture 2D scattering patterns from ice analogue crystals.

Since there are no suitable exact scattering models in existence, to verify the 2D scattering patterns of the RTDF model and SID-2 data, a method of imaging the 2D scattering patterns from ice analogues was devised. To do this with real ice would have been a more complex and in some ways less precise task, however since the analogues have the same refractive index as ice they may be deemed a suitable substitute.

It was important that the solution should allow repeatable experiments on crystals in known and adjustable orientations. Additionally, the crystals should be retrievable for later use. An ellipsoidal reflector was used to capture the scattering pattern. This is shown in Figure 9. The purpose of having an ellipsoidal reflector is so that by positioning the crystal at one focus and the camera lens at the other, near-specular reflections can be collected (since light originating at one focus of an ellipsoid passes through the other.)

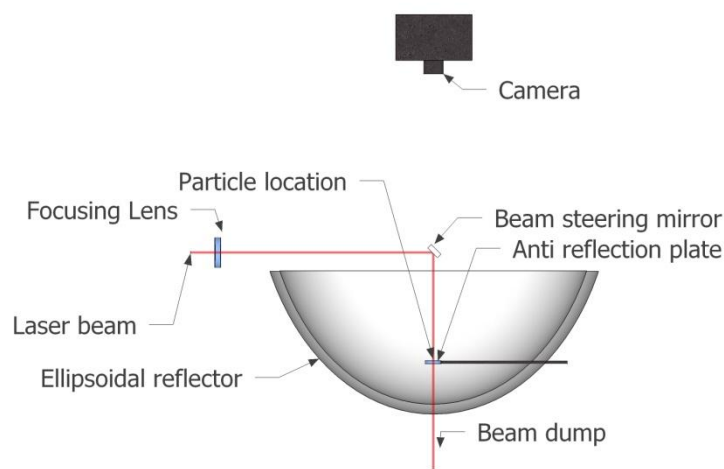


Figure 9 – Schematic showing laboratory rig layout

The matt coating of the ellipsoid permits less stringent precision of the surface than for pure specular (mirror) reflection, and the surface is easier to produce. However, the reflection is not isotropically diffuse, thus the most intense reflection is still received by positioning the camera at the upper focus. The remaining portion of the incident light will be scattered with some deviation from the specular angle of reflection, which causes an increase in background illumination across the surface of the ellipsoid. This background is approximately azimuthally homogeneous. Since a small low polar range is used in the scope of this study, it has not been necessary to quantify the nature of this background, although the effect will be seen in later chapters.

The crystal is placed on a 5mm diameter glass plate with an antireflection coating. This was supported on a thin copper rod passing through a hole in the ellipsoid to a mount with tilt, rotation, and three orthogonal translation stages. This allows precise positioning of the crystal.

The use of a glass plate to support the crystal allows manipulation of the crystal, with only relatively small interference with the scattering pattern caused by reflections between scattered light and the plate. An alternative method of supporting the crystal on a fibre was considered, but rejected due to the strong scattering arc produced. In addition, the plate method allows the crystal to be re-used in other instruments or microscopes, which would allow inter-instrument comparison.

The laser used is of the helium neon variety with wavelength of 612nm, and power 4mW. The beam is focused on the crystal, by means of an external lens. The focusing of the beam is discussed in Appendix C:. The laser was mounted horizontally just above the rim of the ellipsoid, some distance away. The lens is then placed at the appropriate distance from the laser and the ellipsoid to form the correct beam profile at the crystal. Beneath the hole in the base of the ellipsoidal reflector there is an optical beam dump.

Just above the rim of the ellipsoid, a 45° mirror is used to steer the beam from the laser to the crystal. The mirror is supported on another thin rod that in turn allows rotation, tilt and positioning of the mirror. It also acts as a beam stop for the reflection of the beam towards the camera.

5.1.1. Considerations of the camera

A choice of two cameras was available for this set up; a Pixelink PL-B741U or a Xillix Microimager 1400. The Pixelink camera has a high tolerance for saturation of the image, and is connected to a PC via a USB cable. This camera proved to be too noisy to distinguish fine details at the exposure time necessary to obtain a useful image. The Xillix camera has a cooled CCD and is attached to a PC via a PCI frame grabber. Although heavier and more difficult to mount at the height required by the size of the reflector, it provides relatively noise free images. However, the Xillix is more prone to blooming, which makes it difficult to image the low angle details in the presence of a relatively high intensity halo peak.

Comparison of the images indicates that a low-noise image is essential to the accurate capture of detailed patterns. Blooming should be avoided by lowering the exposure time. However, the halo peaks at 22° tend to cause the pattern to saturate sooner than the rest of the image. Should the region below this be of interest, it may be necessary to impose a beam stop over the halo peaks in order to remove the associated blooming.

5.2. Comparison of lab measurements to RTDF

In order to ensure the RTDF was a suitable method for modelling some comparisons were made between similar crystals in similar orientations. Although this has been done previously [71], one particular example will be discussed here in the context of fitting between modelled and measured 2-dimensional scattering patterns. First, a crystal was selected, and examined by SEM to ensure it was *pristine* - i.e. symmetrical, with sharp edges and as free as possible from surface roughness - Figure 10.

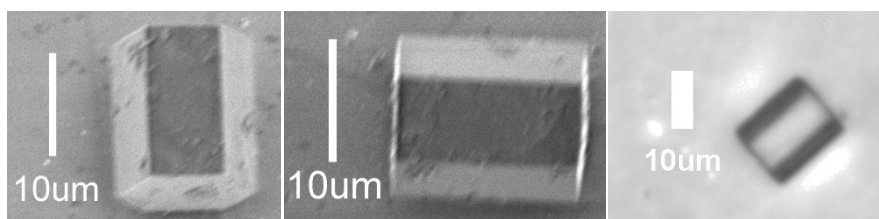


Figure 10 – Three images of crystal sem11_cry04. Left: SEM image with basal facet shown. Middle: SEM image from directly above. Right: Optical image for measurement.

This crystal was then placed into the laboratory rig on the antireflection plate. The plate was rotated by 10° to avoid reflection of the laser toward the camera lens. Using the optical microscopy image to measure the crystal length and diameter ($14.3\mu\text{m}$ and $11.4\mu\text{m}$ respectively), a model representation was created. The representation does not include any surface roughness or chamfering of the edges, and is geometrically regular. Light scattering by this model representation was compared to the observed scattering.

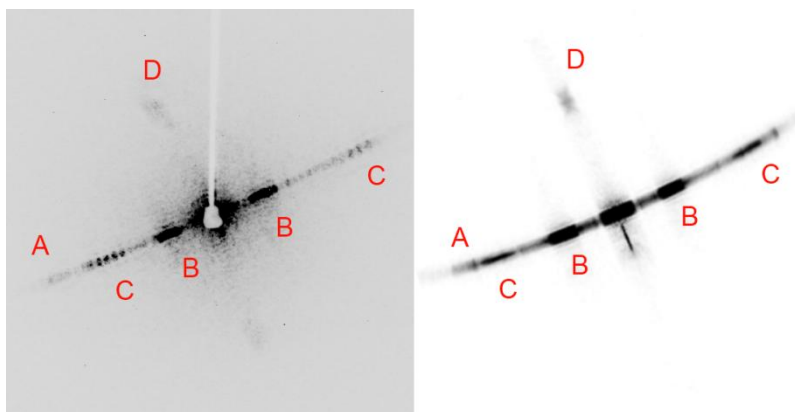


Figure 11 - Comparison of SEM11_cry04 (left) measurement and RTDF model (right). From point A the main arc extends via C (46° halo peak) and B (22° halo peak) through the image centre. Point D indicates the position of light diffracted through a basal facet.

Figure 11 shows a comparison of lab images and corresponding RTDF scattering patterns for a modelled crystal in a similar orientation. It can be seen that the RTDF model faithfully reproduces some of the major features of the measured scattering pattern, including the main arc, primary and secondary halo peaks, and secondary peaks around the halo. The latter are due to the diffraction encountered as rays leave the crystal through a down-facing prism facet. Seen in the more saturated images (Figure 11, A and B), there is a peak caused by scattering from the basal facets. This is wider, and dimmer than those by the longer facets, and is less prominent in the RTDF than the lab images.

Also, the interference fringes along the arc are missing from the RTDF model: this is because the RTDF model does not include interference in calculations. It will not affect this project, since the SID-2 instrument has large polar-range bins over which the maxima and minima will be averaged.

The region of particular interest is between scattering angles 9° and 20° , since this is the angular region recorded by the outer ring of the SID-2 detector. In order to compare the RTDF and the measured patterns more closely, annuli about the pattern centre were considered, for both sets of data (laboratory and modelled). These were individually normalised to the mean intensity of the annulus, and plotted as a function of azimuthal angle - Figure 12 .

In all images of Figure 12, the main arc of the pattern, caused by scattering from prism facets, is clearly well represented by peaks at approximately 110° and 290° . The top row shows the annulus at 13° polar angle, where it can be seen that although the peaks at the main arc fit well, there is detail between the arcs that needs attention. To emphasise low intensity detail, the square root of each pattern is taken and then compared (middle column.) This improves the comparison of the low intensity regions, while maintaining the main arc as a prominent feature. The far right images show the logarithmically scaled intensity patterns. The patterns are again, show a better comparison of the low intensity region as well as the main arc. However, there is a large discrepancy introduced where the logarithm of the RTDF intensity value becomes very strongly negative

in comparison to the laboratory data. This is because the laboratory crystal is much less pristine than the modelled version, and despite the mean subtraction does not dip so low as the RTDF.

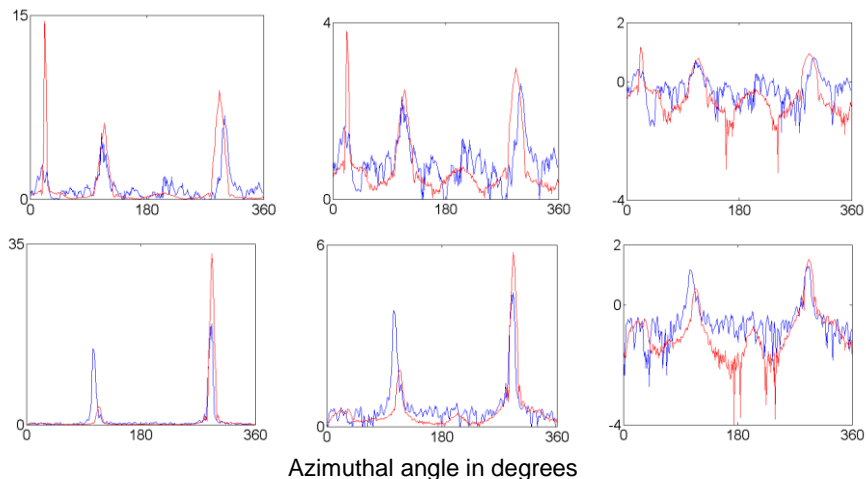


Figure 12 - Comparison of RTDF (red) and laboratory (blue) azimuthal patterns at narrow polar angle ranges. Top: Polar angle 13°. Bottom: Polar angle 23°. Left: linear intensity pattern. Middle: Square root scaling of intensity pattern. Right: Log10 scaling of intensity pattern.

Close to the 22° halo region, the prominence of the main arc is increased. Although outside the imaging range of the SID-2 instruments, this will affect the patterns produced by SID-3 type instruments. Since the halo is common to all regular hexagonal prisms and orders of magnitude stronger than the rest of the pattern in terms of intensity, this region may not provide significant morphology discrimination, beyond perhaps giving an indication that the ice crystal has smooth rather than rough surfaces [69],[72]. Rather, unless the detail in regions of lower intensity, (usually at lower scattering angle) is preserved, the halo may prove to be a hindrance to fitting.

The RTDF code does not at present implement external diffraction for all crystal orientations. For crystals with perpendicular incidence it is however possible to include the effect of Fraunhofer diffraction. Scattering was computed and compared for normal incidence of the crystal with and without Fraunhofer diffraction, and for laboratory data - Figure 13.

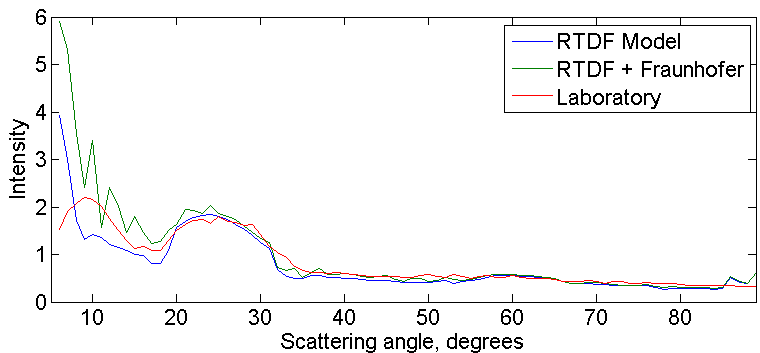


Figure 13 - Comparison of phase functions for RTDF, laboratory and Fraunhofer for crystal SEM11 cry04

As can be seen from Figure 13, the contribution of Fraunhofer diffraction is most significant at low angles, including those of particular interest here. For this project, the Fraunhofer diffraction will not be considered, although future work should place some importance on including this in the model.

Finally, we look at the profile of the main arc of the scattering pattern - Figure 14. There are some differences in alignment and relative intensities between the patterns, which can be associated with small details in the symmetry of the crystal, and the modelled equivalent. The major points of difference to note are the lack of interference pattern in the RTDF pattern (the small oscillations in the pattern are due to the resolution of the RTDF applied to a Cartesian grid to standardise the areas of interest in the pattern) and the increased background in the laboratory image. The latter is most likely due to the matt coating applied to the reflector.

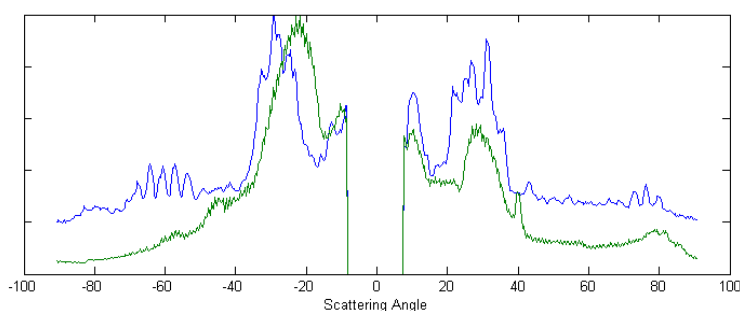


Figure 14 - Comparison between imaged (blue) and modelled (green) scattering pattern along the main arc.

To summarise, a test crystal which resembles a modelled crystal well can be placed in the laboratory rig, and its associated 2D scattering pattern measured. The imaged patterns were compared to the RTDF result of a modelled crystal in similar orientations. The 2D patterns show the same major features as the laboratory image, including main arc from long edge facets, secondary arc from basal facets, primary and secondary halo peaks, and appropriate curvature of both arcs.

Azimuthal cross sections of the scattering pattern and of the main arc show a good agreement between RTDF and imaged results, with major features being well represented by the RTDF model. The square root of the pattern is shown to effectively increase the prominence of lower intensity features by comparison to the main arc.

Fraunhofer diffraction on crystal outline is shown to be of negligible importance in the region of interest of this project.

5.3. Data formatting from Cartesian images to polar arrays

As has been previously mentioned, the SID-2 instrument records data from 24 azimuthal bins between 9° and 20° polar (scattering) angle. The aim of this section is to describe how the Cartesian pixel array of the Xillix CCD (and/or the SID-3 image data) is transformed into the polar coordinate system of a SID-2 instrument. This method also applies to data from the SID-3 instrument. It is worth noting here that the CCD arrays of the SID-3 and the laboratory rig are capable of higher azimuthal resolution than the SID-2 instrument (from 0.2° to 0.7° depending on polar angle.)

The nature of CCD arrays is that they suffer from pixel vignetting – the fall off of recorded intensity with increased incident angle. This effect is most pronounced in the corners of the image, and as such is not allowed for in the post processing of images. Both the SID-3 and laboratory rig images are approximately centred on the CCD, and as such are not greatly affected by the effect.

The first step in data formatting is to remove any background reading from the data, since in both the SID-3 instrument and the lab rig there is a constant measureable background. In both cases, this can be attributed to stray light from the optical system and dirty optics, particularly the plate on which the crystal sits, since the beam is focused here.

For laboratory tests, a background image was recorded for each of the crystal scattering pattern images. This was done by moving the crystal out of the scattering volume of the laser and recording an image with the same gain and exposure time as for the image of the scattering pattern.

The centre of the image must also be found. With the SID-3 instrument, this can be done with a microsphere. The microsphere is placed on the glass plate, which is then manoeuvred into the centre of the scattering volume. The centre of the scattering volume can be found by monitoring the trigger detector levels while moving the particle through the beam. An image of the scattering pattern is then recorded. The centre of the concentric rings indicates the centre of the image.

A similar procedure is used for the laboratory rig, with the main difference being that the position of the crystal is determined by observing the intensity of the scattering pattern as the particle is moved through the beam.

Finally, the image is binned into azimuthal bins analogous to the SID-2 outer ring. Any (CCD) pixel that spans the boundary of two (azimuthal) bins is accurately dissected. The intensity of the pixel is then divided between associated bins in proportion to the respective pixel area in each bin.

Normalisation is performed to the mean of the azimuthal pattern, as it is with modelled data.

This procedure is also used to bin data from the SID-3 probe into azimuthal intensity patterns.

6. The reference database & data manipulation

This section describes the process of creating a database of reference crystals, and the limits placed upon it. It will provide details on the resolution of the parameters involved in setting up the database, and the effect each one has.

The modelled database is a set of two dimensional scattering patterns calculated from the RTDF model. Each pattern has 1° resolution in both the azimuthal and polar (scattering) angles, with the azimuthal range being 1° - 360° and the polar range from 1° to 90° . This range allows selective binning into arrays to approximate the physical layout of the SID-2 detector, or other similar arrays.

Each orientation is modelled with one million rays, and 100 interactions per ray. The wavelength is $0.612\mu\text{m}$ (to match that of the laboratory set up) and the refractive index is set to 1.311 – the refractive index of both the ice analogue crystals and water ice crystals at this wavelength.

The morphology of the modelled crystals is limited to single pristine hexagonal prisms. Parameters that are modified are the basal indentation depth, size and aspect ratio. The aspect ratio of the crystals is defined as length/diameter where the diameter is twice the edge length of a basal facet. Size is defined as the diameter of a circle with the same area as the average projected cross section from a large number of random orientations of the crystal (known as the *projected area diameter* – PAD). Basal indentation is the pyramidal indentation formed by moving the point at the centre of each basal facet along the crystal axis toward the centre. It is given in terms of the percentage of the length of a crystal for which the indentation of a single basal facet extends toward the centre. For symmetry, it is assumed that the basal indentation is identical at both ends of the crystal – see Figure 15.

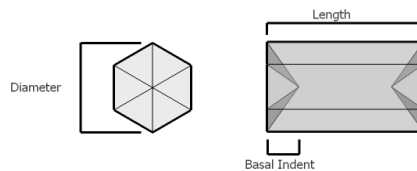


Figure 15 - Crystal dimensions. Basal indentation is referred to as a percentage of the length. Length and diameter are both referred to in micrometers.

With the above mentioned three parameters, a database is built with the following limits

- Size: $6\mu\text{m}$ to $38\mu\text{m}$, 9 divisions
- Aspect ratio: 8:1/8, 9 divisions
- Basal indent: 0% to 49%, 8 divisions

This gives a total of 72 crystal shapes, each in 9 sizes to be modelled. Each crystal is modelled for 133 orientations. The orientations of modelled crystals are described in terms of Euler angles, using the notation in[56].

6.1. Conversion from RTDF to SID-2 analogous data

This section will describe the required considerations in converting from the output of the RTDF to SID-2 type bins.

In the straightforward case, a crystal is modelled for its 133 orientations and then binned into required azimuthal bins, within a designated polar range. Additionally, a second set of 133 orientations are formed by

rotating the bin mask one half of a bin width. Rotating the mask with respect to the pattern causes local peaks to be spread over more than one bin, and vice versa. In total, there are now 266 orientations of azimuthally binned data.

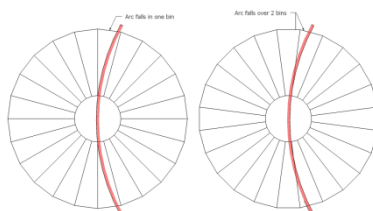


Figure 16 - Rotating the mask with respect to the pattern causes local peaks to be spread over more than one bin, and vice versa

Since the mirror support of the lab rig shadows the image, this has to be taken into account. This is done by removing any affected bin from consideration. Since at the lower SID-2 polar angle, the azimuthal range of the shadow is approximately 40° , three bins are removed from the lab data. This is done by removing every combination of 3 consecutive bins from every orientation, for every modelled crystal. For a single crystal with 266 orientations and 24 azimuthal bins, this equates to 6384 unique patterns. This causes a considerable increase in the time taken to compute the fitting.

The range of polar angles covered by the outer ring of the SID-2 detector is 9° - 19.8° . In order to reduce the amount of processing required for the RTDF model, the polar resolution is set to one degree. Because of this, the maximum polar angle will be assumed to be 20° when comparing against modelled data.

The more advanced SID-3 instrument's range of visible scattering angles is 6.8° to 25.5° . The SID-3 detector has some unevenness to the beam stop - and to the field stop, causing both stray light and variation in the angular range. For this reason, calculations will be performed only on the 7 - 25° polar region.

6.2. Interpretation of scattering patterns and rose plots

This section is intended to aid the reader in the visual interpretation of 2D scattering patterns and the associated rose plots from a range of crystal sizes, aspect ratios and basal indentations.

Scattering patterns of hexagonal prisms share certain similarities, irrespective of size and aspect ratio. The orientation of a crystal is often evidenced by the curvature of scattering arcs, or the predominance of a single arc from prismatic facets as opposed to a six pointed star shape from the hexagonal basal facet. Indentations of the basal facet often cause secondary arcs to form, superimposed on the simpler pattern of a pristine crystal.

6.2.1. Intensity scaling

The whole scattered intensity range is difficult to visualise. At the high end of the scale are the forward scattering region, and the halo peaks. However, as has already been discussed, there are many important details at lower intensities. To display these, some scaling should be applied.

For the following discussion, maximum intensity is represented as black to aid in visualisation after printing.

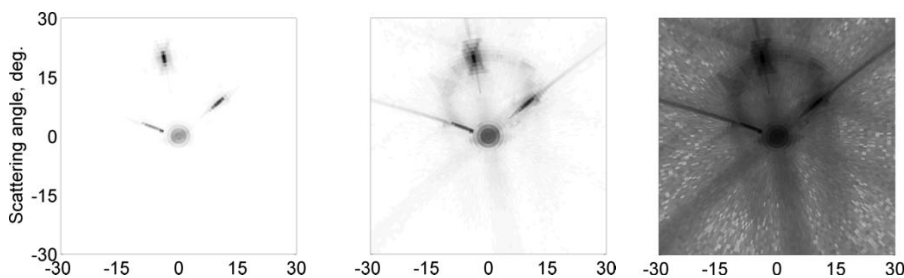


Figure 17 - Comparison of scattering pattern intensity scaling. Left: Linear. Middle: Square root. Right: Log10

From Figure 17, one may realise that the closer one looks, the more detail can be observed. Since the square root scaling shows the majority of the relevant scattering detail while maintaining a reasonable similarity with the linear pattern, it will be used for the rest of this discussion. This weighting has the advantage of having a physical link to the size of the particle, since the square root of the intensity scales with particle size. The maximum displayed intensity will occasionally be capped so that lower intensity detail is highlighted.

6.2.2. Orientation

Orientation is possibly the single largest contributor to scattering pattern variation.

The description of the crystal orientation is provided in terms of the Euler angles. The Euler rotation theorem indicates that any orientation can be described by three rotations. There are multiple conventions for the definition of each angle; however in this project the convention used is taken from the RTDF code as described below.

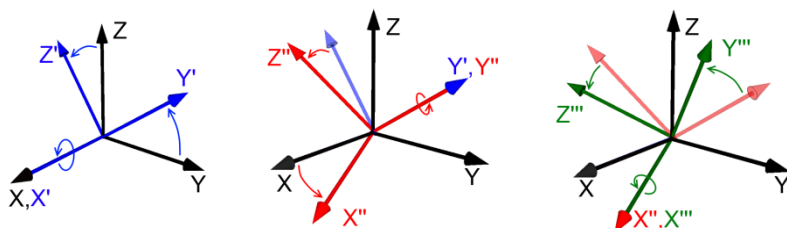


Figure 18 – Euler angles of rotation in order of execution

The laboratory reference frame consists of a Cartesian coordinate system, $L(X,Y,Z)$. The initial conditions for the RTDF code have the long axis of a column parallel with the X axis with two facets normal to the Z axis. Rays propagate along the negative X axis. A rotation about the X axis constitutes the *alpha* (α) rotation - Figure 18, left. The reference frame of the particle moves with the rotation, to $P(X',Y',Z')$, where X' remains parallel to X. The *beta* (β) rotation is about the Y' axis (Figure 18, middle), transforming the reference frame of the particle to $P(X'',Y'',Z'')$. The final *gamma* (γ) rotation (Figure 18, right), is about the X'' axis, which from the reference frame of the particle is identical to the alpha rotation.

The crystals and orientations shown in this chapter are all included in the modelled database. Angles close to 0° , 90° and 30° have been replaced with 2° , 88° and 28° respectively. The rose plots shown have a bin width of 5° , and a polar range of 7° to 25° .

6.2.2.1 Beta orientation

The orientation dependence will first be described for the simplest and most common of the crystal classes considered– the column. Table 2 shows the modelled scattering pattern from a crystal, with the rose plot superimposed on the top. The crystal is $41.5\mu\text{m}$ long, and $7.5\mu\text{m}$ in diameter, giving a projected size of $18\mu\text{m}$, and an aspect ratio of 5.5. Progression down the table decreases the beta angle, and from left to right increases the gamma angle.

In the simplest and most recognisable form, where the beam is incident approximately normally to a prismatic facet ($\beta=88^\circ$, $\gamma=2^\circ$), the scattering pattern is a simple straight line across the detector. The halo peaks are clearly visible in the 2D scattering pattern, and the width of the arc is well represented in the rose plot. The majority of the scattering occurs from the long prismatic facets, and thus the 2° shift in alignment is barely evident.

Following Table 2 down the first column ($\gamma=2^\circ$) the crystal is rotated to a beta angle of 50° , and the scattering arc begins to curve. This is very apparent in the 2D pattern, but the corresponding change in the rose pattern is more subtle. The curvature is indicated by a broadening of the peaks, and a redistribution of the brightest point to the edge of the peak, rather than the centre. The hexagonal basal facets have very little influence at this set of orientations. This curvature would be better represented if the detector were more able to resolve in the polar dimension.

At a beta orientation of 30° the curvature of the main arc is increased, and the full length of the halo peak becomes exposed within the limit of the range of scattering angle. The curvature of the scattering arc is demonstrated by the width and the skew of the peaks on the polar plot more than it is by changing of the angle of the centre of the peaks. Secondary peaks are visible on the rose plot, caused by diffraction from the edges of the basal facets (Table 2, $\beta=30^\circ$; $\gamma=2^\circ$: vertical peaks. $\gamma=28^\circ$: Peaks at 45° to the vertical).

For a 20° β orientation, the orientation becomes more obvious in the rose plot, where the main peaks begin to move towards each other. The 10° β orientation pattern barely resembles the prior ones, due to the sudden appearance of a bright spot between at the top middle of the pattern. This is caused by light entering through one basal facet, and exiting through the other having been reflected once on a prismatic facet - Figure 19.



Figure 19 - Ray path of bright spot at 20° at 10° beta orientation

Furthermore, the curved arc has been replaced by two straight lines with 120° between them. At this point, the basal facets are responsible for more of the scattering than the prismatic ones.

At the final orientation shown, $\beta=2^\circ$, the basal facets are almost normal to the beam. The only identifiable features are diffraction peaks from the edge of the basal facets, which are small by comparison to the rest of the azimuthal bins. The majority of the intensity is scattered below 5° from the direction of propagation.

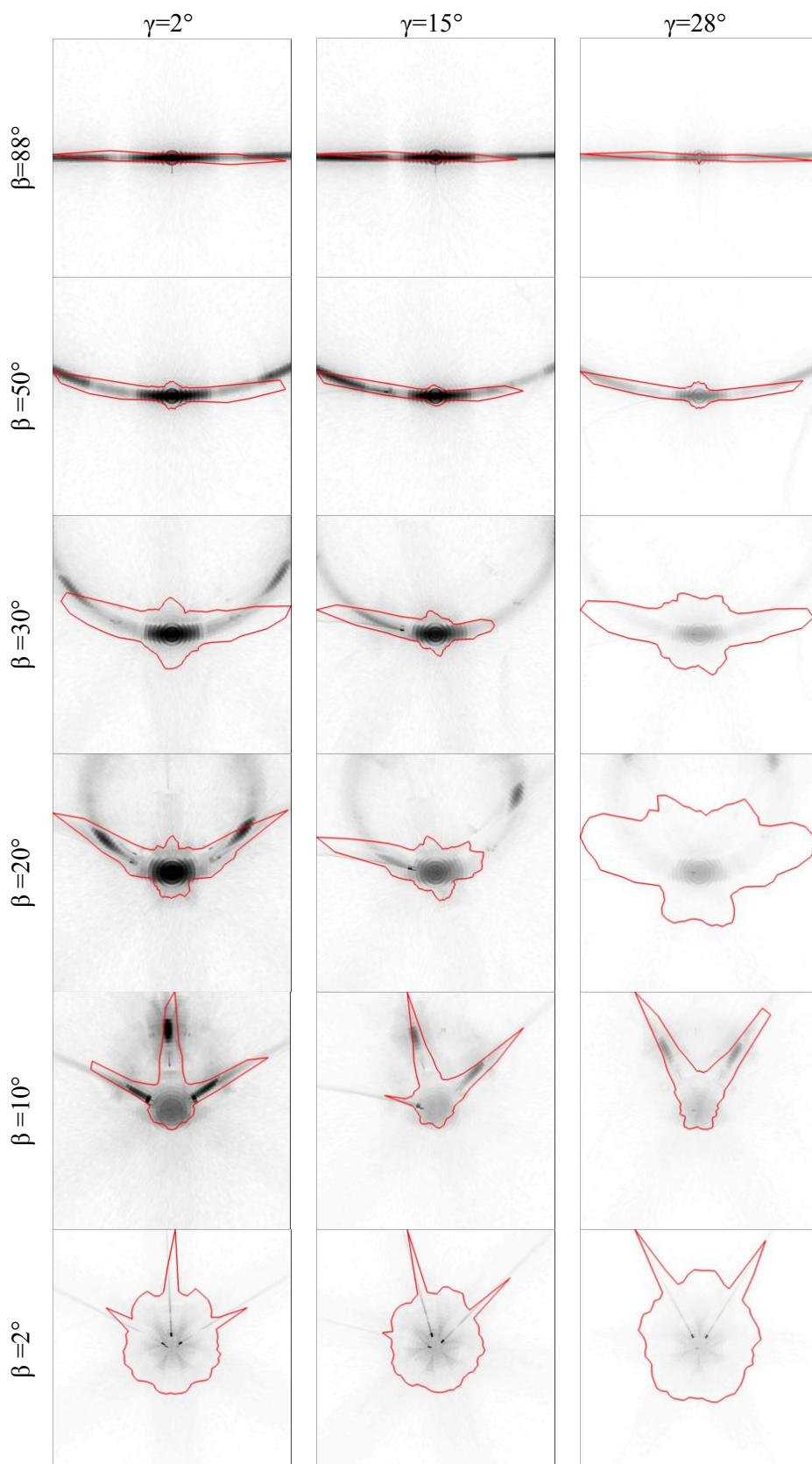


Table 2 - Comparison of beta and gamma rotation influences on the square root weighted scattering pattern from an 18 μ m column. Intensity capped at 70% of maximum. Maximum polar (scattering) angle is 30 $^\circ$.

6.2.2.2 Gamma rotation

The gamma rotation is applied after the beta rotation, and is performed along the axis of the crystal passing through the centre of both basal facets.

When the beam is incident approximately normally to a prismatic facet (Table 2, $\beta= 88^\circ$, $\gamma=2^\circ$) or the edge between two prismatic facets ($\beta= 88^\circ$, $\gamma=28^\circ$), the pattern appears symmetrical. In between these cases ($\beta= 88^\circ$, $\gamma=15^\circ$), the pattern becomes asymmetrical. It can be seen in Table 2 that the relative intensity of one side of the main arc is increased with respect to the other. This is due to the larger cross section of one entry facet, which increases the intensity (number of rays) exiting on the opposite side - Figure 20.

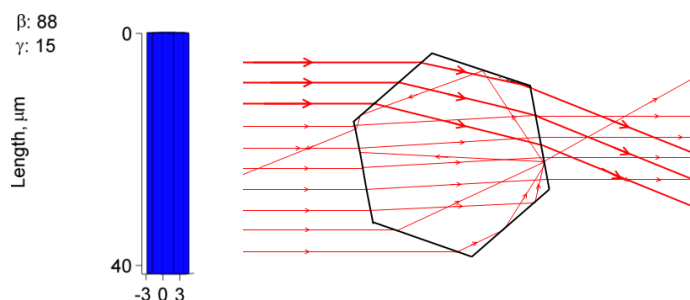


Figure 20 – Geometric optics representation to demonstrate that increasing the visible cross section of one side facet increases the scattered intensity on the opposite side.

This effect is similar for all instances where the prismatic facets are responsible for the majority of scattering ($\beta > 20^\circ$).

Between $\beta=20^\circ$ and $\beta=10^\circ$ at $\gamma=15^\circ$ a shift in the pattern asymmetry occurs, from higher intensity on the left, to higher intensity on the right. This is where the hexagonal facet becomes dominant, rather than the prismatic facets. The hexagonal edge of the basal facet furthest from the laser source dominates the scattering pattern. Figure 21 indicates how the decrease in beta angle increases the proportion of the cross section marked by the basal facets, compared to that of the prismatic facets.

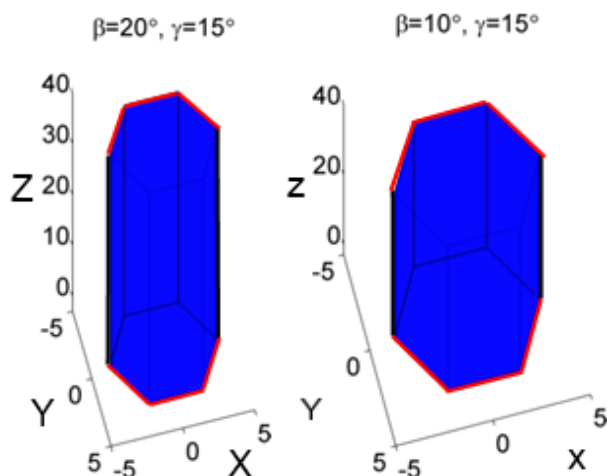


Figure 21 - Comparison of two views of the same column at different beta orientation angles. Red lines indicate region of border of the cross section from basal facets. Incident beam normal to the page, passing from front to back. X, Y and Z are width, depth and height in laboratory frame in microns.

6.2.3. Size and Aspect Ratio

The size and aspect ratio of a crystal are the features of most interest in this project. Table 3 shows a comparison of a range of crystals at the same orientation ($\beta=30^\circ$, $\gamma=2^\circ$).

For an aspect ratio of 8, the clearest change between scattering patterns as the size decreases is that the breadth of the main arc increases. Also, the vertical arc (caused by diffraction from the basal facets) decreases.

As the aspect ratio decreases (going down a column of Table 3), the source of the brightest features of the scattering pattern shifts from the prismatic to the basal facets. This is shown by the gradual removal of the curved arc seen at the top of Table 3, to be replaced by the six less curved arcs from the hexagonal basal facets seen towards the bottom of the table.

An interesting example is that of the pattern shown for a size of $34\mu\text{m}$ and an aspect ratio of 3 (or to a lesser extent, 8). Looking at the rose plot, we can count six peaks (at 12, 3, 4:30, 6, 7:30, and 9 o'clock). Usually, six peaks on a rose plot can be associated with a plate, however; this is clearly a column.

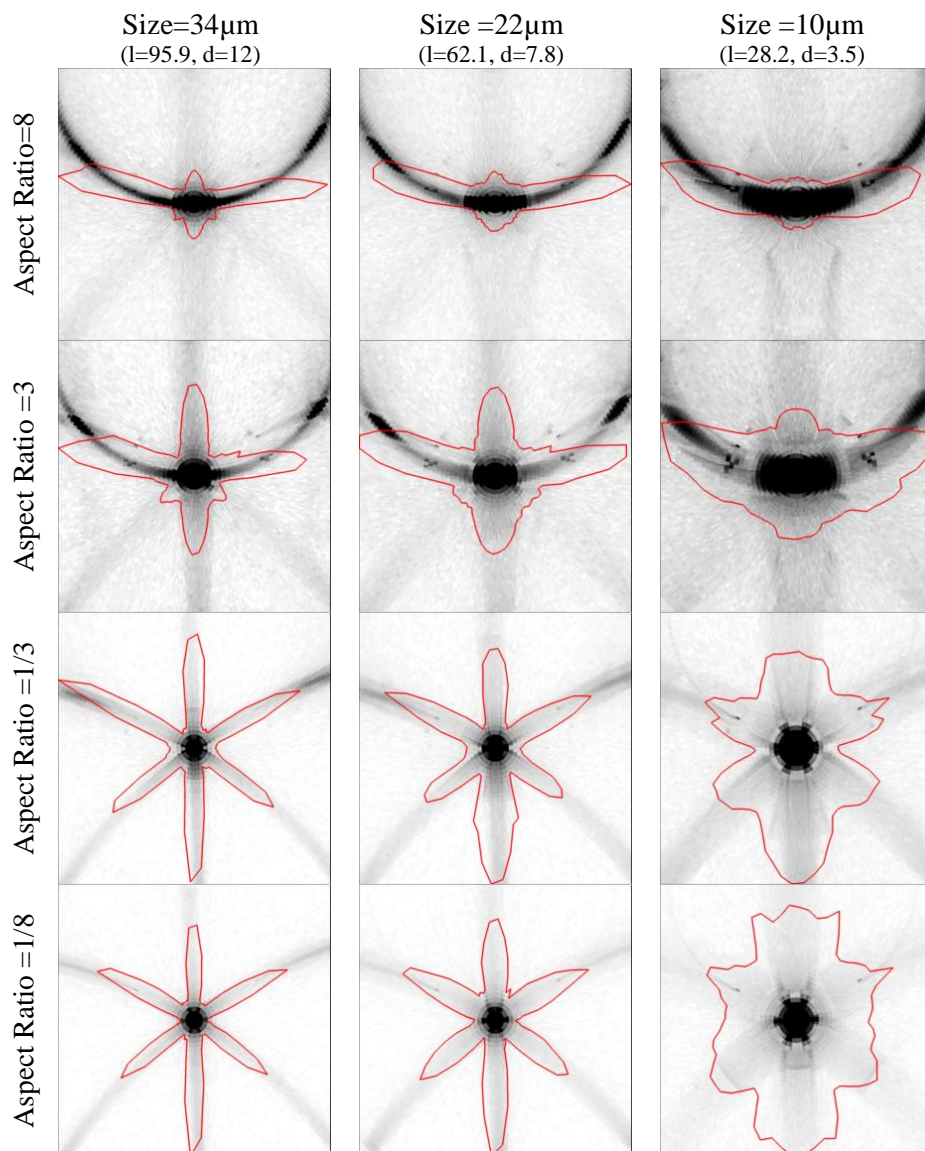


Table 3 - Comparison of size and aspect ratio on the scattering pattern from a crystal in the $\beta=30^\circ$, $\gamma=2^\circ$ orientation. Intensity is capped at 15%, 25% and 40% of maximum for size of 34 μm , 22 μm and 10 μm respectively. Maximum scattering angle shown is 30° along the vertical/horizontal.

6.2.4. Basal Indentation

The influence of basal indentation on the scattering pattern is most clearly represented for columns in an orientation where diffraction is dominated by the prismatic facets. The main arc is augmented with a pair of secondary arcs that do not pass through the centre of the scattering pattern. On the rose plots these arcs are represented by broad peaks.

These secondary arcs have been observed (Figure 22) by a SID-3 instrument in AIDA, Germany, during the ACI03 campaign. They compare very favourably to the modelled equivalents shown in Table 4 (AR 5.5, $\beta=30^\circ$).

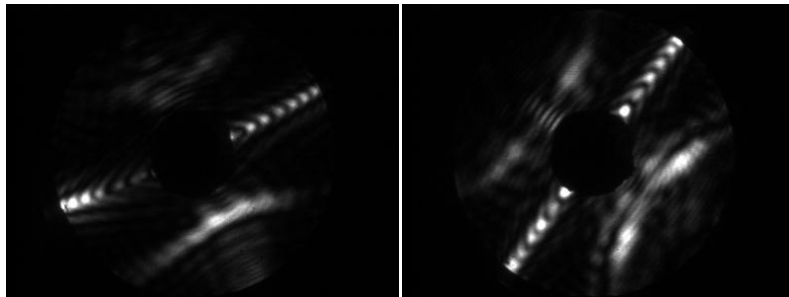


Figure 22 - Examples of scattering patterns from crystals with basal indentations. Taken by SID-3 at the ACI03 experiment

Similarly for plates, the increase in basal indentation removes the dominance of the main scattering arcs, to the point where the rose pattern appears almost round in the extreme case (Table 4).

The 2D scattering images show that as basal indentation increases, the brightest region moves from the centre outwards. The basal indentation of the crystal gives it a cross section similar to a concave lens, causing the incident beam to diverge – Figure 23.

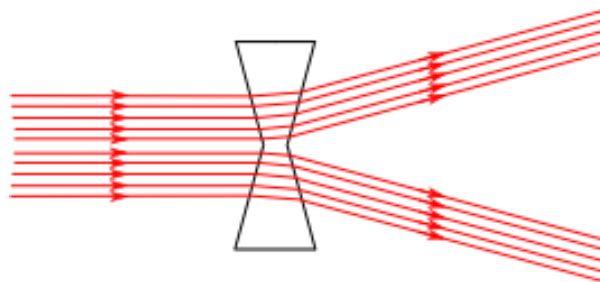


Figure 23 - Low aspect ratio crystals with basal indentation acts as a concave lens

This effect can clearly be seen in Figure 24, where a pair of scattering patterns from a similar crystal differing only in its basal indentation shows how the intense region of the pattern moves away from the centre with increased basal indent.

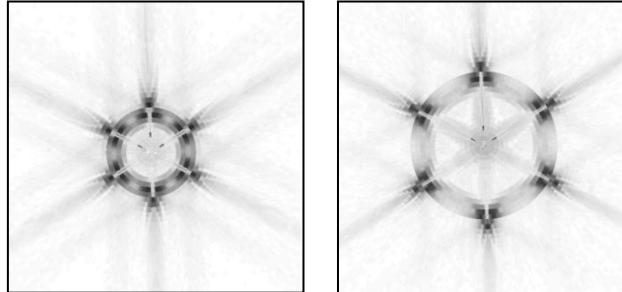


Figure 24 - Scattering pattern from 38 μ m crystal with aspect ratio 0.3 and basal indentation of 28% (left) and 49% (right)

An important note to make regarding Figure 24 is that fine detail in the most intense regions is due to scattering from triangular facets. The current RTDF model does not accurately compute such scattering; however for comparison of binned data such as is used in this project the fine detail is lost, and so does not affect the results. Work is currently being undertaken to resolve this issue in future versions of the RTDF code.

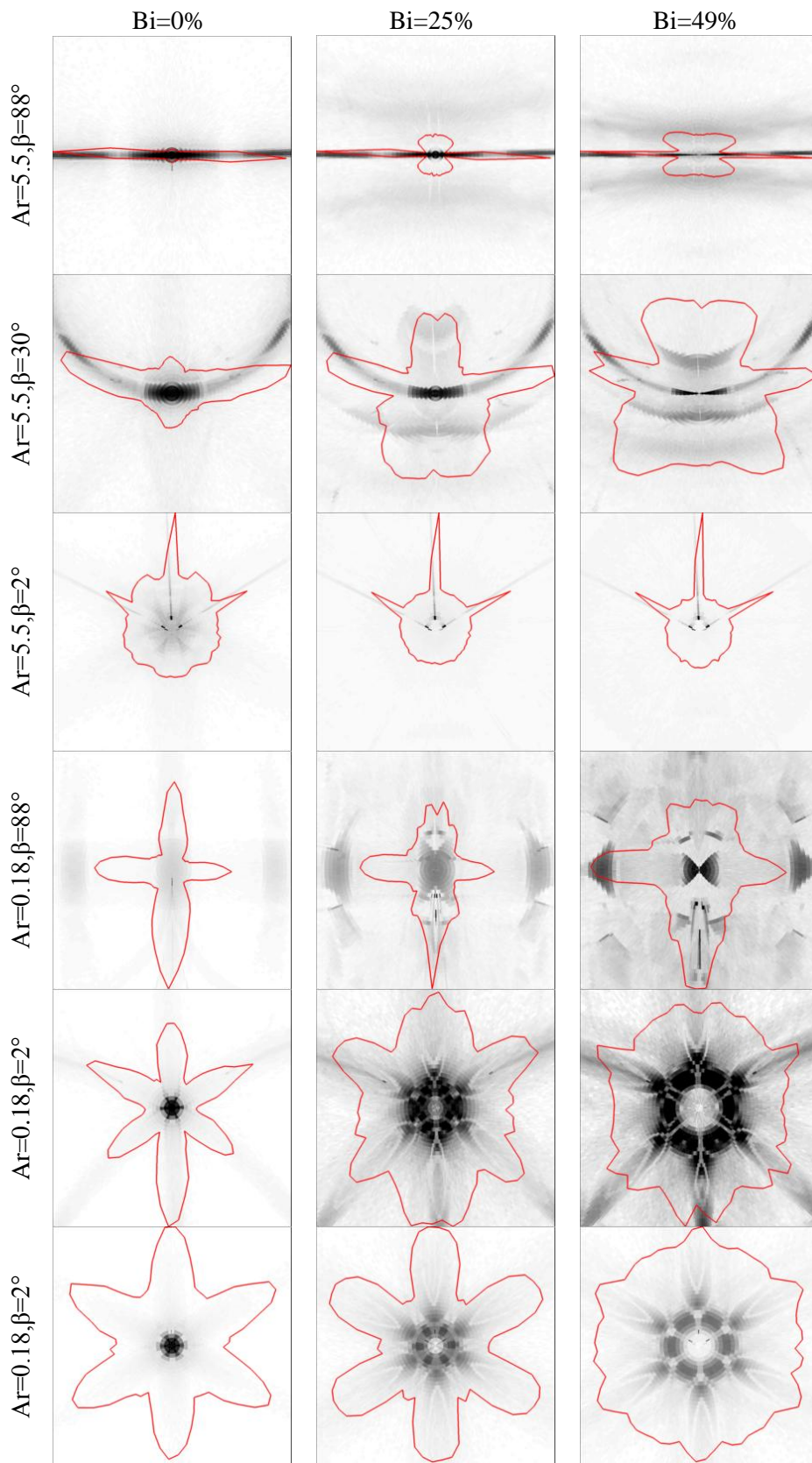


Table 4 - Comparison of basal indentations of 0%, 25% and 49% for scattering patterns from crystals of aspect ratio 5.5 and 0.18, with $\beta=2^\circ, 30^\circ$ and 88° . Crystal size is $18\mu\text{m}$. Maximum polar (scattering) angle is 30° .

7. Investigating the accuracy of fitting methods

In order to test methods of pattern fitting, a method of measuring the accuracy needs to be defined. Also, to allow quantitative comparison between fitting methods, a test data set will be defined.

7.1. Error calculations

The database of reference patterns can be thought of as a three dimensional array of bins. Each bin contains all the scattering patterns (either from multiple orientations of a single crystal, or from multiple crystals) associated with a crystal of a particular size, aspect ratio and basal indentation. The space this array occupies is called the *fitting space*.

An error function is used to determine how well a test pattern is fitted to the database. The fitting error (Δ_F) is defined as the root mean square difference in path length separating the fit to the expected bin in the fitting space - Eq. 3.

$$\Delta_F = \sqrt{\frac{1}{n} \sum_n (l_n - b_n)^2} \quad \text{Eq. 3}$$

$$\Delta_\theta = \frac{1}{n} \sqrt{\sum_\theta (2 - 2 \cos(\theta_{ref} - \theta_{test}))} \quad \text{Eq. 4}$$

Where n is the number of patterns fitted, $l_n - b_n$ is the distance between the expected location of a fit, and the location of the bin to which a pattern is fitted, and $\theta_{ref} - \theta_{test}$ represents the difference in orientation of the crystal.

The fitting error does not include any difference between the orientation of the reference and fitted crystals. Since the objective of this project is to determine the morphology of a crystal, it does not make sense to include this in the fitting analysis. However, since it is a useful piece of information, where referenced, the error in orientation between crystals (Δ_θ) is measured as the Euclidean distance between them, Eq. 4. It should be noted that due to symmetry in the crystal structure, the maximum difference between alpha and gamma angles is 30° , and the maximum difference between beta angles is 45° .

It could be argued that a limitation of the accuracy of the fitting error in terms of the ability to judge a good fit is that the maximum path length (and hence calculated error) for patterns is not invariant with respect to the position of the test pattern in the fitting space. I.e. for a particle at the extreme limit of the fitting space, the maximum path length is greater than that in the centre of the fitting space. However, this is not so significant since if a particle is being incorrectly identified to such a degree that it is limited by the maximum path length of the fitting space, then the fitting method is obviously flawed.

7.2. Modelled test data

In order to perform a series of tests of various modelling data, a set of 45 test particles was generated, with sizes, aspect ratios and orientation not equal to those in the reference database. Selection of these parameters is not random; they are chosen to represent a range of sizes and aspect ratios within the limits of the database.

The 2D scattering is then calculated using the RTDF model as it was for the reference database. This data set can then be manipulated in the same manner as the reference database to provide a benchmark for the various fitting methods to be discussed.

7.3. Fitting accuracy dependence on resolution of fitting space

In the fitting space, a unit of distance is equal to the distance between one bin and its neighbour in any single dimension.

The distance d between the location of a test scattering pattern and its nearest bin in the fitting space is defined by a variation parameter Eq. 5. This will have a range between 0 and 0.5 (0.5 being halfway between two bins.)

$$\Delta d = \frac{\text{distance from nearest bin}}{\text{distance from 2nd nearest bin} - \text{distance from nearest bin}}$$

Eq. 5

To test the reference database, the azimuthal intensity pattern comparison fitting method (which will be described in detail in Chapter 8.3) was used to fit the test set of 45 modelled crystals. The mean fitting error per crystal was plotted against Δd - Figure 25.

There is no trend towards higher error with increased distance from the nearest bin, suggesting that the density of reference bins is not the limiting factor in fitting accuracy, but rather the orientation or the method itself.

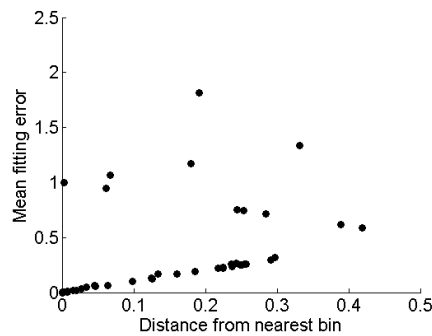


Figure 25 - Mean fitting error plotted against distance from nearest bin in fitting space

The preceding discussion indicates that the accuracy of fitting is not limited by the distance of a test particle from its nearest bin in the fitting space of the database. This is due to the resolution of the fitting space being sufficiently high to be of little consequence by comparison with effects of individual particle scattering profiles.

7.4. Pie-Bubble plots

To visually inspect the results of fitting an arbitrary number of crystals to the database, pie bubble plots are introduced.

Figure 26 (right) shows an example of a fitting to a modelled crystal. The horizontal axis shows the aspect ratio, the vertical represents the projected area equivalent size. Each pie is located according to the best fit in these two dimensions. The radius of each pie indicates the number of fits at this location in the fitting space. The pie sectors are coloured and sized according to the number of patterns fitted to each basal indentation. The colour-bar indicates the relationship between colour and basal indentation. A star is placed at the

expected location, coloured appropriately to its basal indentation. This plot format allows three dimensions to be displayed on a 2D page.

The total error of the fitting is 3.1. The expected location is indicated with a star, and lies at about 6 μ m PAD, unit aspect ratio with no basal indentation. The majority of patterns are fitted to the appropriate size with some spread in aspect ratio, and basal indentation. Patterns fitted to incorrect aspect ratios and sizes tend to be assigned a large basal indentation.

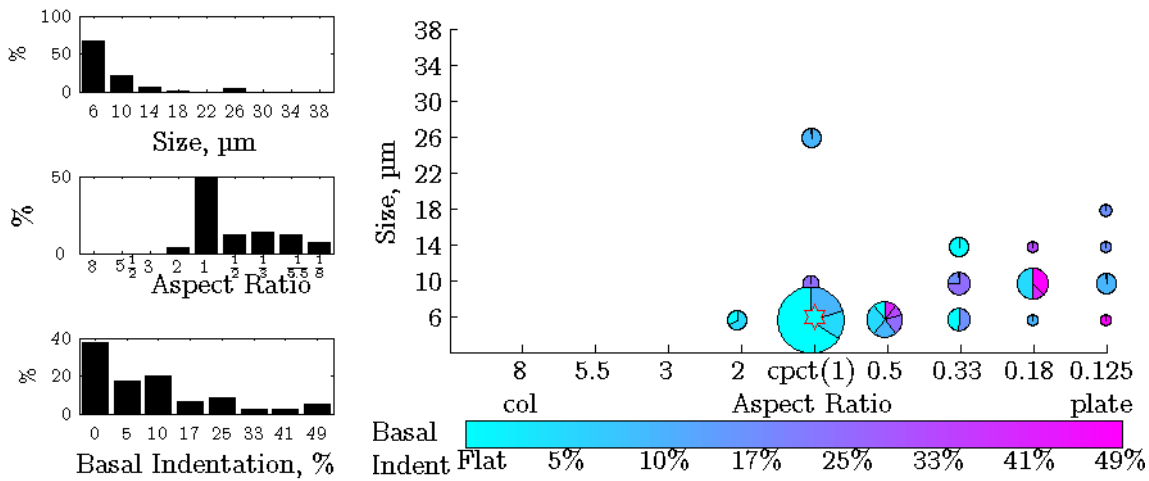


Figure 26- Example of 6 μ m, unity AR, compact crystal - fitted using azimuthal pattern matching

Figure 27 by contrast shows the same fitting method applied to a crystal with a size of about 25 μ m, aspect ratio of 3 and no basal indent. The error is lower than the previous example at 1.0 since most the fits are clustered about the expected location.

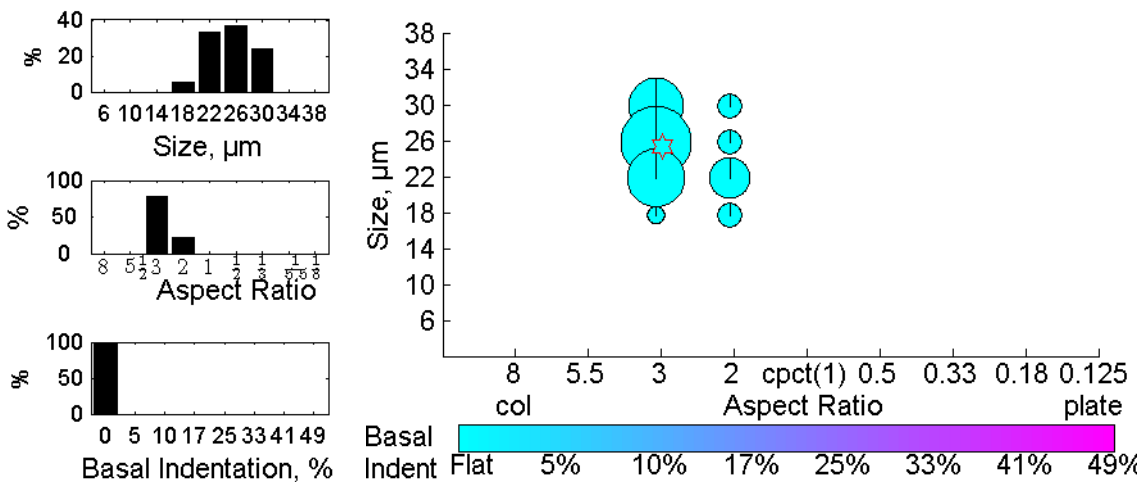


Figure 27 - Example of 25 μ m, 3 AR, flat crystal - variation of 0.16 from nearest reference bin, fitted using azimuthal pattern matching

7.5. Orientation dependence of goodness of fit

Since the computational model allows us to assign any orientation to the crystal being modelled, it is important to find a balance between enough orientations and viable computation times and storage memory requirements.

For comparison, two reference databases were produced with different orientation resolutions. The lower resolution of the two had an orientation angle step of 10°, with ranges between 0° to 90° in beta, and 0° to 30° in gamma. (In fact, the 0°, 30° and 90° were replaced with 2°, 28° and 88° due to the infinitesimal chances of encountering such uniquely symmetric orientations in reality.)

The higher resolution database has a step of 5°. This increased the number of orientations per crystal morphology from 80 to 266, which slows down the processing and increases the amount of computational resources required to run a fitting sample – particularly using a direct azimuthal intensity pattern fitting (as opposed to the FFT method or other statistical measure as discussed in Chapter 8).

A crystal from the reference set was modelled at a range of angles not equal to those in the reference sets, and the resulting patterns fitted back to both databases. For the 10° step database, around 50% of the patterns were fitted to the correct bin, with the next largest bins being its neighbours - Figure 28. The rest of the patterns were spread around the fitting space, particularly in amongst those bins with a similar or slightly smaller aspect ratio.

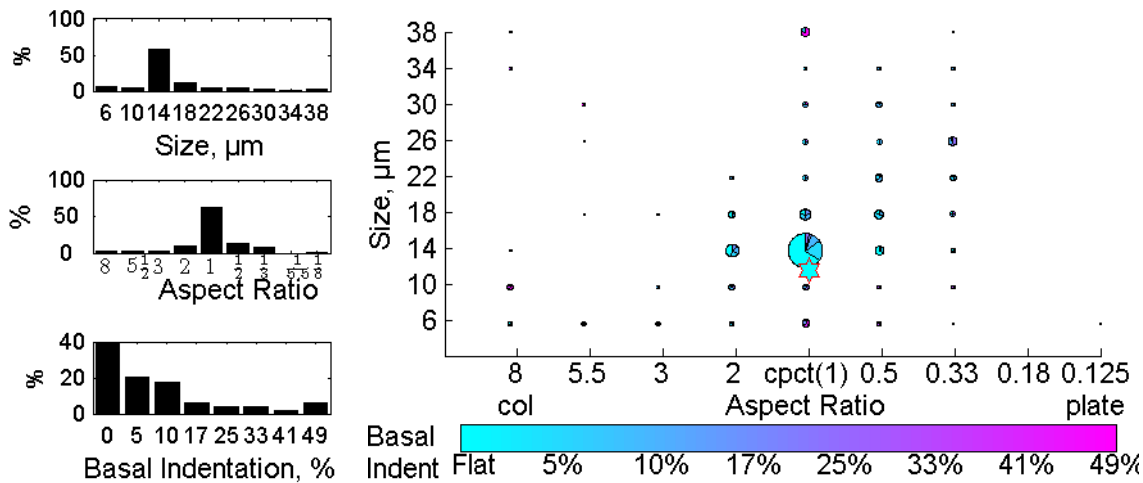


Figure 28 - Off-orientation patterns fitted to the low orientation resolution azimuthal pattern reference set.

The effect of increase in resolution on the accuracy of fitting can be seen in Figure 29 where the spread of fits is much reduced, and the mean error is a low 1.4 compared to the 3.5 of the lower resolution set. 90% of the patterns are fitted to within one bin of the expected position.

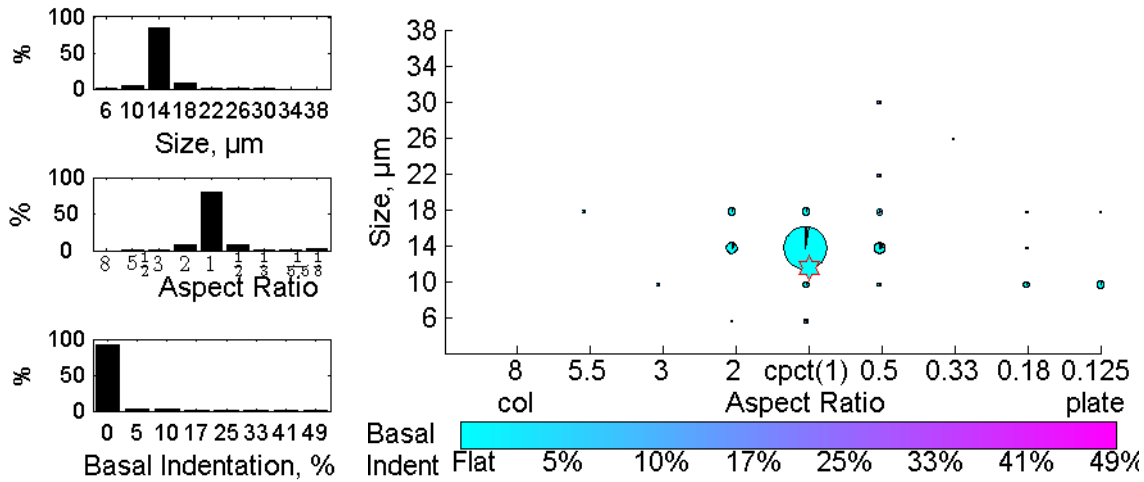


Figure 29 - Off orientation comparison with high orientation resolution azimuthal pattern fitting set.

This demonstrates that there is a large difference between patterns for a small change in orientation which indicates the importance of having to resolve resolution well. It also demonstrates the importance of a model capable of providing the reference data, since it would become very tedious to measure so many orientations physically.

8. Methods of comparing test data to the modelled reference database

This chapter describes several methods of classification, including direct comparison of the AIP, and comparison of the Fast Fourier Transform (FFT) to equivalent modelled reference data. The goodness of fit will be investigated and the reliability and limitations of the method discussed.

Statistical measures of images are often used in machine vision, for purposes such as optical character recognition [73], facial expression recognition [74], counting individual fish species based on silhouettes [75], identifying aircraft [76].

An advantage of using statistical measures of the pattern is that though they become more accurate with higher azimuthal resolution the number of data points do not change. That is, there are always a limited number of points to compare, and so the amount of time taken to fit is based on the number of measures, test patterns and the size of the reference database, rather than the resolution of the AIP. The FFT and direct AIP matching methods (discussed below) have a larger number of data points per pattern for higher azimuthal resolutions which limits their performance.

Some important factors to consider for the following discussion are as follows:

- Azimuthal orientation independence. Unless a method of determining the azimuthal orientation of a scattering pattern on the detector can be found, each fitting method will have to work regardless of the orientation.
- Absolute intensity value independence. Different methods of collecting data inherently incur different absolute values of intensity. These need to be normalised in order to compare to one another. Calibration may be performed on a per-instrument basis, however it should be noted that this calibration may become inaccurate as changes in the instrument detector and/or laser occur [66].

8.1. Asymmetry Factor

The Asymmetry Factor (Af) is a measure of the distribution of intensity around the azimuth of the scattering pattern [77]. It is applied to data binned into discrete azimuthal bins over a pre-determined range of polar angles.

An advantage of using this measure is that a set of properties can be reduced to a single value per crystal, dramatically speeding up the time required to compare it to the modelled database.

The Af is calculated using the expression in Eq. 8 where the coefficient of variation is weighted to cap the maximum Af to 100.

$$Af = \frac{k[\sum_{i=1}^n (\bar{E} - E_i)^2]^{1/2}}{\bar{E}} \quad \text{Eq. 6}$$

Where k is a weighting function to cap the maximum Af to 100

$$k = 100/\sqrt{n(n-1)} \quad \text{Eq. 7}$$

and n is the number of data points in a pattern, E_i is the intensity of data point i , and \bar{E} is the mean of all data points in a pattern.

The Af was calculated for every orientation of every modelled crystal in the reference and test data sets. Each test pattern was then fitted to the reference database by minimising the difference between them. The mean error was calculated for a range of azimuthal resolutions and polar ranges, and the results shown in Figure 30.

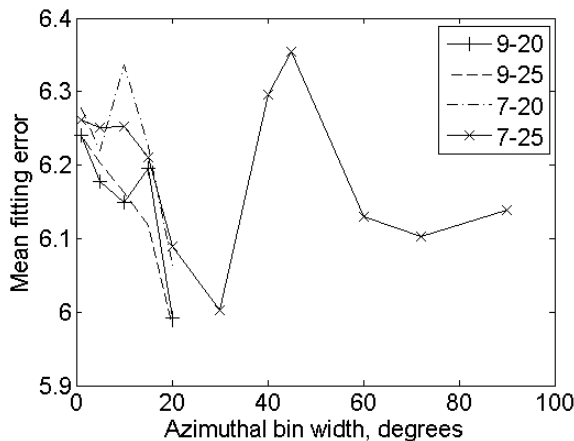


Figure 30 - Mean error for asymmetry function fitting over range of azimuthal resolutions and polar ranges

An example of one of the lower errors in this set – that for a medium sized compact crystal – is 6 for an azimuthal resolution of 20°, and a polar range of 9°-20°. The error is clearly very high, and in fact the case is virtually indistinguishable from a random spread through the fitting space - Figure 31.

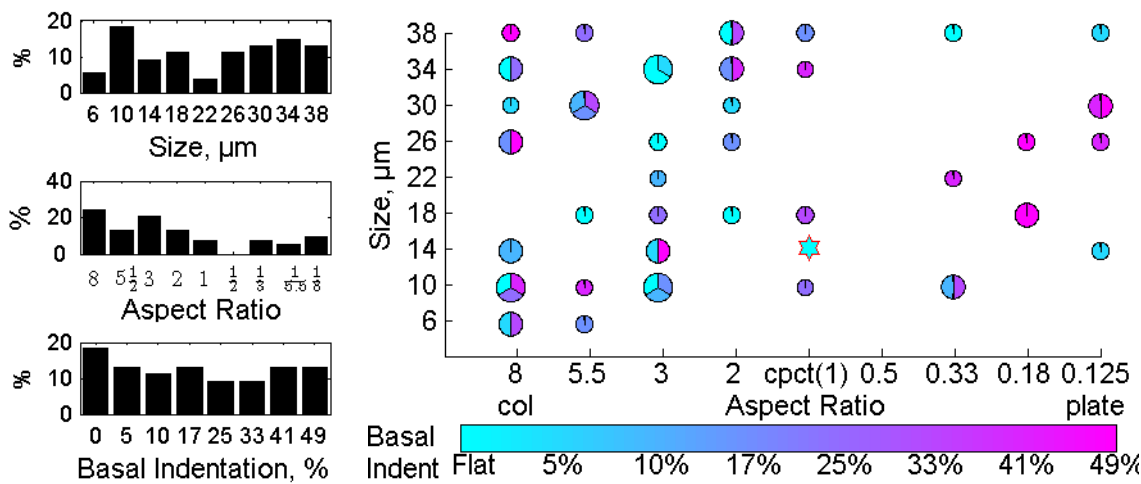


Figure 31 - Example of modelled crystal fitted by asymmetry factor comparison with an azimuthal resolution of 20°, and a polar range of 9°-20°. The error of fitting is 6.

Although previous studies have shown that it is suitable for the separation of droplets from nonspherical scatterers [77], asymmetry factor alone is not a suitable method of differentiating crystal size, length or basal indentation.

8.2. Moment invariants

Moment invariants have been the staple of computer vision since Hu introduced them in 1962 [78]. Since then, they have been corrected [79], improved [80] and applied to a wide array of shape discrimination exercises.

The invariants consist of a set of statistical measures of a 2D image that are independent of scale, rotation and translation. For the purposes of this project, translation independence is irrelevant, since scattering patterns are central to a known point on the detector, which is defined as the origin. A rotational invariant measure of the scattering pattern is essential to an accurate fit, since the orientation of a crystal is as much unknown as its morphology.

The invariant moments are derived from a set of complex moments introduced by Flusser [79]. Equation 5 from Flusser's paper is shown below (Eq. 8), as a method of calculating the complex moments C of the order $(p+q)$ from polar coordinates of an image.

$$c_{pq} = \int_0^{\infty} \int_0^{2\pi} r^{p+q+1} e^{i(p-q)\theta} f(r, \theta) dr d\theta \quad \text{Eq. 8}$$

For the purpose of this investigation, the image function is considered to be a binary image of the rose plot, and equal to one for a radius below the intensity at a given azimuthal bin, otherwise zero. The radius was divided into 50 equal divisions between 0 and the value of the bin with the maximum intensity, after being normalised to the mean.

Flusser suggests a set of 11 invariants that are mutually independent. Each consists of the product of complex moments up to third order. These are calculated for each scattering pattern of each crystal in the reference database for a given resolution, and then normalised to the mean over the whole database. The normalisation values are then used to scale the test data, in order that each invariant will have an equal weight.

A minimization of the RMS between the test data set and the reference database was then performed on a per-pattern basis.

The mean error over the entire test, for an azimuthal bin width of 5° is 8.3. This is higher than would be desirable for a good fit. An example of a fitting for large column is shown in Figure 32. It is apparent that although there is some slight clustering of results in the correct region, the majority of fits are scattered randomly through the fitting space.

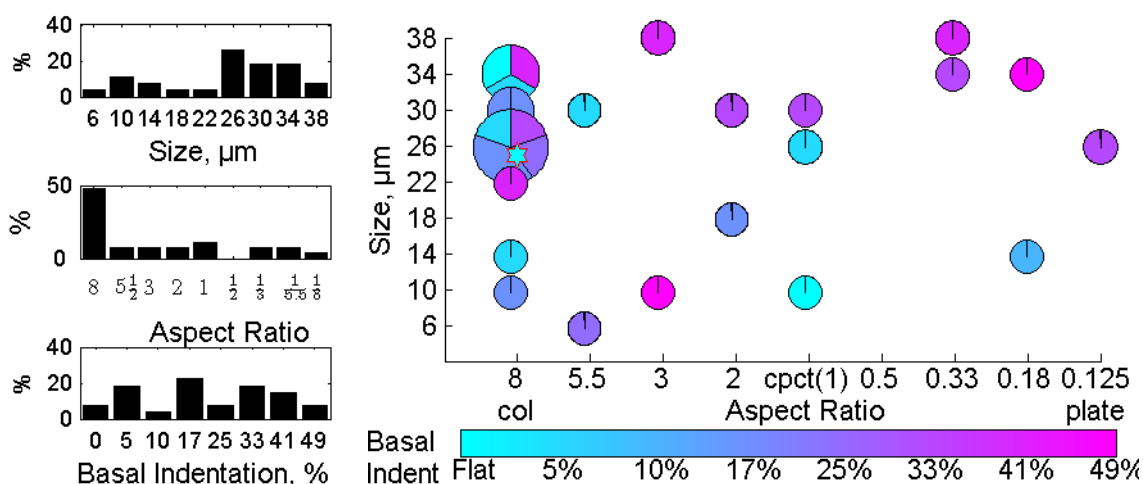


Figure 32 - Example of fitting of column to the reference database based on discrimination by moment invariants.

To summarise; first, second and third order invariant moments were calculated for the reference database, and for a set of test crystals based on azimuthal scattering data with 5° wide bins. The mean value of each invariant was normalised with respect to the reference database. The invariants were then compared between the reference set and the test set, with the minimum RMS between sets of invariants used to determine a best fit. Fitting results were largely random, with a small amount of clustering seen in some cases.

Improved fitting might be accomplished by investigating the discrimination power of each moment invariant, and weighting them in the RMS calculation accordingly. Neural networks are ideally suited to this type of investigation, and have been shown to perform well with light scattering information [12]. Other weighting factors can be trialled manually, such as those suggested by Wong et al [73]. Unfortunately, time constraint and the large number of iterations required for such an investigation prevent this project covering this in more detail.

8.3. Direct Azimuthal Intensity Pattern Comparison

In order to compare one AIP against another, the azimuthal dependence must be removed. In order to do this without performing any mathematical manipulation of the data, the test pattern must undergo a pseudo-rotation with respect to the reference database. For binned azimuthal intensity data, the most accurate manner in which to do this is to shift the last bin of the data set to the beginning and calculate the RMS for as many bins as there are in the pattern. This increases the processing time of the fitting method by a factor equal to the number of bins in the AIP, which is a considerable amount.

As mentioned previously, the data is also normalised to the mean of the AIP, in order to make laboratory, modelled and SID-series instrument data comparable. For the purpose of the current discussion, normalisation may be a hindrance to the fitting process, since both reference and test data are modelled and hence receive exactly the same incident intensity. For objectivity however, normalisation is performed.

As was discussed in section 5.2, scaling the data by means of square root or logarithms increases the prominence of low intensity data. Both these and un-weighted data are compared.

Two methods of comparison were tested to arrive at a fit; minimising the RMS difference between the AIPs, and the maximum difference between individual bins of a pair of patterns. The RMS will allow for small deviations between coefficients while the maximum difference method will be stricter about the differences.

8.4. Fourier Transform Method

The fast Fourier transform (FFT) is an algorithm developed to increase the efficiency of machine computation of the Fourier transform. It was first made popular by Cooley and Turkey in their 1965 paper [81] in which they proposed a robust method for reducing the number of calculations required to compute a given series of N complex data points from N^2 to $N \log_2 N$.

In this investigation, the FFT will be used to represent the azimuthal dependence of scattering in the frequency domain. The magnitude of each (complex) coefficient is used, which effectively removes the phase of the pattern, hence the azimuthal rotation dependence. The zeroth coefficient (equivalent to the mean intensity) is then used to normalise the remaining 12 coefficients - Figure 33. By normalising to the mean this process removes the absolute intensities – leaving only the relative ratios between bins [82].

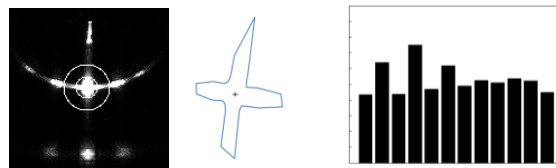


Figure 33 - from left to right – 2D scattering pattern from RTDF modelled column (rings represent area recorded by the SID-2 detector), polar plot of square root intensity of SID-2 pattern, normalised FFT spectrum of polar plot

The FFT is taken for the entire set of modelled reference data, as well as for the test pattern in question. Comparison was performed using the maximum and RMS differences between spectra, as in section 8.3.

8.5. Comparison of fitting methods, data ranges and resolutions

Test data was fitted to the reference database using both FFT fitting and direct azimuthal pattern fitting. For each method, the best fit was determined by minimising either the RMS difference, or the maximum difference between the test and reference patterns. Comparisons were performed at 15° azimuthal resolution, with a polar range of 9° - 20° to be analogous to SID-2 data. The results (Figure 34) show that minimising the RMS is a better indicator of a good fit than minimising the maximum difference, and also that the AIP-fitting improves the accuracy by a factor of 1.5 in comparison to the FFT method.

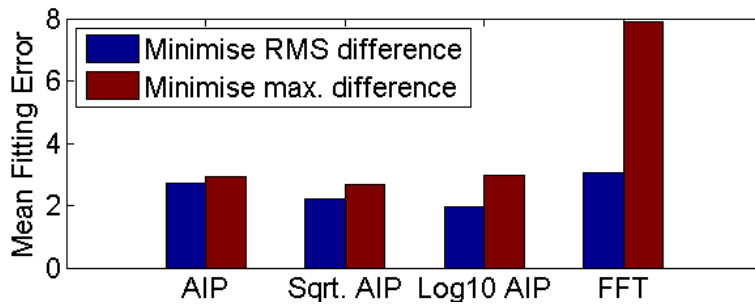


Figure 34 - Comparison of mean error while fitting a test data set to using different measures of best fit.

Although the AIP fitting is clearly more accurate, it does take considerably longer than the FFT method, since the number of data points per pattern is twice that of the FFT, and (more importantly) a pseudo-rotation is required. This pseudo-rotation is required about the azimuth, since the data is not rotation independent. The number of rotation steps is defined by the number of azimuthal bins being considered. E.g. for the SID-2 type detector mask with 24 bins, each test pattern must be rotated 24 times.

To demonstrate the importance of azimuthal resolution, a test was done fitting the same data to databases with different angular resolutions. As is seen in Figure 35 the fitting is much improved by decreasing the angular width of the bins, although there are diminishing returns in accuracy for resolutions below 15° and increased computation times.

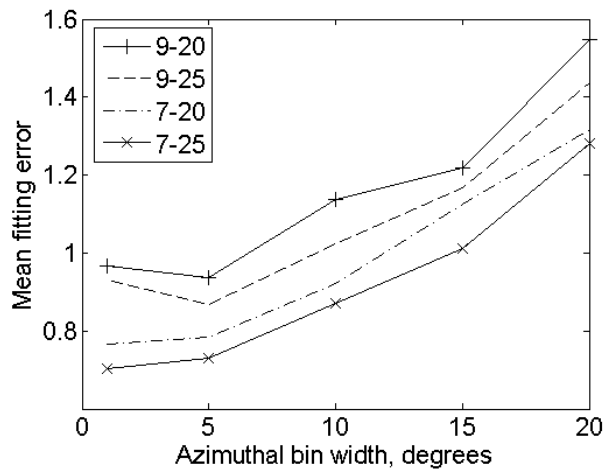


Figure 35 – Comparison of mean error in fitting over different azimuthal resolutions and polar ranges using log10 scaled AIP fitting

Clearly, low angle scattering contains a substantial amount of information relevant to this fitting method. The improvement in accuracy gained by the reduction of the lower polar limit by 2° is greater than by increasing the higher polar limit by 5°. This will be an important point to consider in the design of future instruments.

Also note that an increase in error occurs for the 1° azimuthal bin width, for all but the 7°-25° polar range. This is probably because of the limitation of logarithms used for intensity scaling in this example. Because a finite number of rays are modelled per crystal orientation, some bins will receive zero intensity. To reduce this effect, zero values are set to a very low figure. Data with a larger range of polar angles is less susceptible

to the effect, since there is a higher probability of there being enough information in a single azimuthal bin to avoid the logarithm being too inaccurate.

Scaling intensity using the square root is not affected by this singularity, and so does not show the same increase in error - Figure 36. However, the bias is not so effective at removing the dependence on the high intensity halo peaks, and so the data with a large maximum polar angle is less accurate than that with a lower maximum.

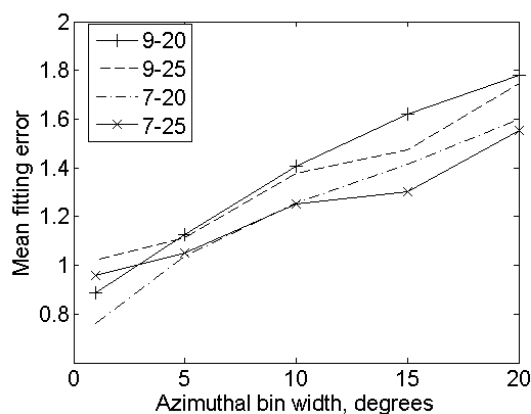


Figure 36 - Comparison of mean error in fitting over different azimuthal resolutions and polar ranges using square root scaled AIP fitting

To summarise, increased azimuthal resolution is an important factor in improving the fitting method. Logarithmic scaling of the data can lead to inaccurate fitting when there is inadequate data in one or more azimuthal bins. This can be countered, in principle, by increasing the polar range of the scattering pattern.

Taking the SID-2 polar range of 9° to 20° with an azimuthal bin width of 15° as a reference point, the decrease in error for increasing the maximum polar limit by 5° is 3%. By decreasing the minimum polar limit by 2° , the error is decreased by 14%. To achieve this without reducing the minimum polar limit one would have to double the number of azimuthal bins.

8.6. Orientation determination

Although the primary topic of interest in this project is the determination of crystal morphology, the methods used are also highly sensitive to orientation as it alters the characteristic scattering considerably. Crystal alignment is known to exist in the atmosphere, as evidenced by the existence of sundogs. Recent discoveries suggest that other atmospheric aerosols may also be aligned [83].

Having fitted the modelled reference data to the reference database, the mean Euclidean distance between orientations was determined for each azimuthal resolution and polar range, as in section 8.5, and is shown in Figure 37.

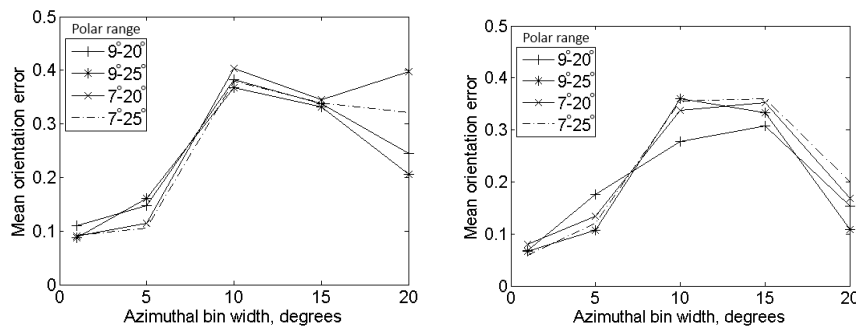


Figure 37 - Comparison of accuracy of orientation determination for various azimuthal resolutions and polar ranges fitted with logarithmic (left) and square root (right) intensity scaling

The minimum possible error is 0.06, due to the difference in orientations between the modelled and reference data sets. The maximum error is 6.93, which occurs when there is a difference of 30° between the alpha and gamma angles, and 45° between the beta angles of the reference and modelled crystal.

Both scaling methods show that the orientation is fitted very well, with both showing that low bin width improves orientation determination. In the case of the 20° bin however, it appears that some improvement is made to the orientation determination despite it being the largest bin width tested. The effect is more pronounced with square root weighting, where all tested polar ranges showed this improvement. This is not due to a large degree of error – at no point does the standard deviation exceed 18% of the mean, with the average standard deviation being around 13%. The mean difference in orientation error between the 15° and 20° bin width is 47%. This minimum is localised, the error increases with increased bin width above 20° .

This effect may be useful in identifying crystal orientation using lower azimuthal resolution detectors. A more extensive investigation into the cause would have to be performed however.

8.7. Effect of removing bins from azimuthal patterns

Since the laboratory rig requires the removal of some of the pixels (and hence azimuthal bins) from consideration due to the shadow cast by the rod supporting the 5mm plate, the effect of this on fitting is investigated.

For 45 modelled crystals, the scattering was calculated and binned to 36 azimuthal bins. From these, 5 consecutive bins were removed from each pattern, in every possible permutation. The data was fitted to the reference pattern before and after the removal of the bins, and the mean error compared.

As expected, the accuracy of the fit dropped with the removal of bins. In this case, the mean error of fitting without shadowed bins was 1.6, while with the bins removed it increased to 2.0. This corresponds to a 25% increase in error for a 14% reduction in data points.

Although the removal of bins has a significant effect in reducing the accuracy of fit, it is a necessary compromise to enable the controlled positioning of a particle.

9. Case studies

This section will present a series of case studies demonstrating the fitting methods applied to ice analogue crystals in the laboratory and ice crystals from the SID-3 probe.

9.1. Case Study: Compact column ice analogue

To investigate the viability of these methods for characterising real crystals, as opposed to modelled equivalents, it is necessary to perform tests in the laboratory. For these purposes ice analogues (see section 4) were used.

The crystal used was a hexagonal prism 14.3 μm long, and 11.4 μm in diameter (the same crystal as described in section 5.2, Figure 10). SEM shows that it is symmetrical, with no basal indentation, and minimal surface roughness. The aspect ratio is 1.3, with an orientation averaged projected area equivalent diameter of 13 μm . The Δd (distance from the nearest modelled bin) is 0.39. The crystal is a good candidate for a trial since modelled crystals can approximate it well, and it is well within the range of parameters covered by the reference database, while not precisely fitting any one bin.

The crystal was placed in the lab rig, and the resulting scattering pattern was imaged a total of 8 times at 5 degree increments of the theta rotation angle described in 5.1. Unfortunately the crystal was lost before any further orientations were performed, but the data retrieved was sufficient for this discussion.

The data was transformed into SID-2 type data, of 24 azimuthal bins between 9° and 20° polar angles. Three of these bins were then removed from consideration, due to being partially shadowed by the supporting arm. The mean pixel intensity over the region of interest was subtracted from each pixel, and any value below zero was neglected. This has the effect of truncating the lower values of the pixel range, with the intention of removing noise. This will also effectively reduce the width of any scattering peaks, which may introduce a bias towards larger sizes.

Table 5 shows a selection of the measured SID-2 equivalent plots after removal of the shadowed region compared with the RTDF modelled equivalent. The rose plots show the azimuthal scattering pattern, while the bar plots show the FFT of the same pattern. Three bins were removed from the RTDF pattern in order to calculate the FFT spectra in a manner that is comparable to the lab data. Crystal orientation is also shown – the top facet as seen from above in the first orientation is coloured grey in all images, to aid in determining the proper perspective.

The missing points in the lab data plot correspond to the shadowed region of the image. These points are not removed from the RTDF in this table, other than for calculation of the FFT.

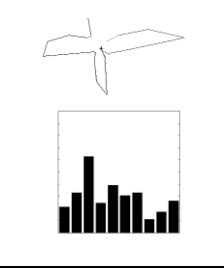
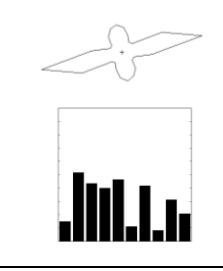
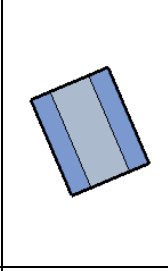
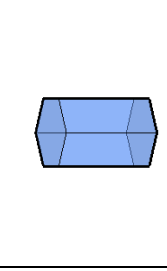
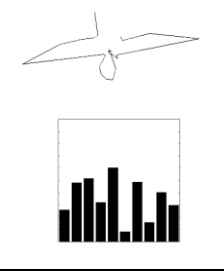
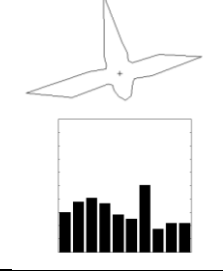
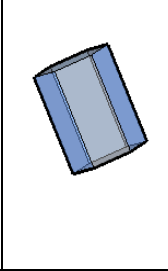
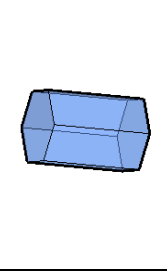
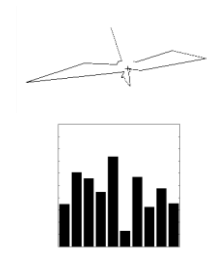
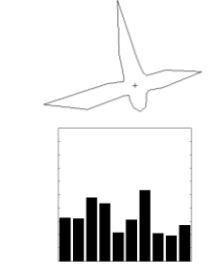
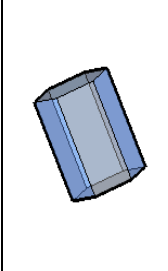
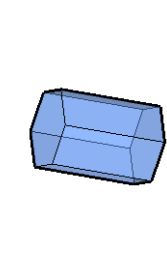
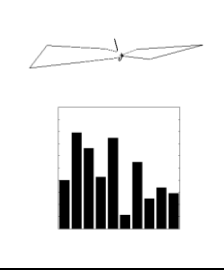
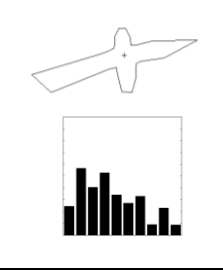
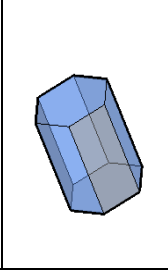
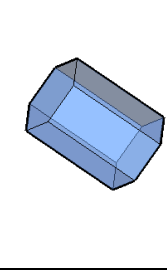
Euler angles	Lab pattern	RTDF pattern	View from above (incident beam)	View from left
$\alpha: 23$ $\beta: 90$ $\gamma: 0$				
$\alpha: 23$ $\beta: 85$ $\gamma: 2$				
$\alpha: 23$ $\beta: 80$ $\gamma: 4$				
$\alpha: 23$ $\beta: 58$ $\gamma: 14$				

Table 5 - Rose plots of azimuthal scattering patterns and bar plots of FFT from laboratory rig and RTDF model for four orientations of the SEM11_cry04 crystal. “View from above” gives the orientation from which the laser is incident, and “view from left” is from the left as seen in the first view.

A visual inspection of the azimuthal patterns shows common features between the lab and RTDF data. The main and secondary arcs are generally well presented, although the latter appears more prominently in the RTDF data. This is most likely due to surface roughness on the basal facets of the ice analogue.

In contrast, the RTDF FFT patterns show very little resemblance to their laboratory counterparts.

Figure 38 shows the results of fitting SEM11_cry04 using the FFT method. Although there appears to be a cluster of some patterns around the target star in the 2D aspect ratio & size plane, there is a large discrepancy in the basal indentation selections. The error of this fitting is 7.6.

Figure 39 shows the results of the direct pattern matching to the modelled database. The Δd (distance) for this crystal is 0.39, and the error of the fitting is 5.2. Clearly, despite the ice analogue crystal being regularly symmetrical and free from irregularities, fitting is still poor.

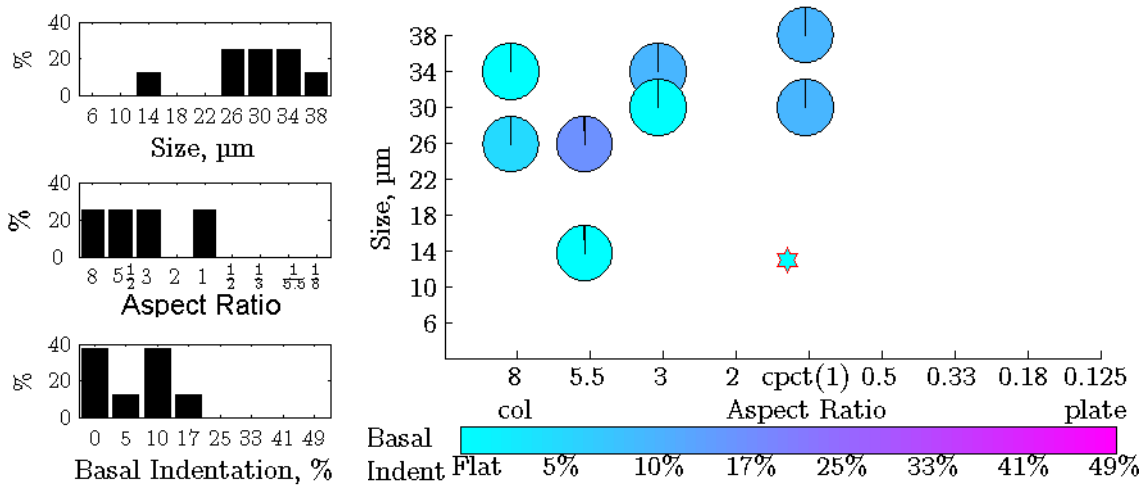


Figure 38 - Results of FFT pattern fitting of SEM11_cry04 to reference database. The Δd is 0.39, and error is 5.2.

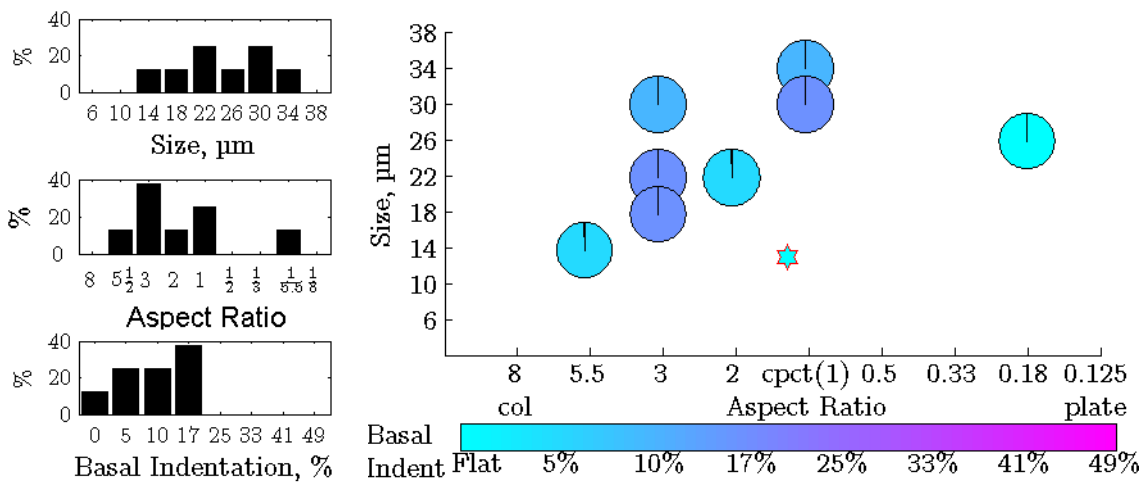


Figure 39 – Results of direct pattern matching for SEM11_cry04. The Δd is 0.39, and error is 4.3.

The laboratory test patterns and the modelled reference to which it was fitted are very similar, (Table 6) despite not being fitted correctly. This suggests that for crystals of largely different morphology differences between scattering patterns can be very subtle in the 9° to 20° region.

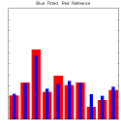
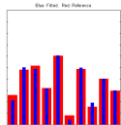
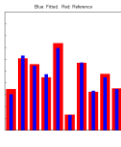
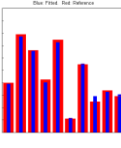
Direct azimuthal pattern matching	FFT fitting method
 $\Delta_{\theta}1.8 \quad \Delta_F5.2$	 $\Delta_{\theta}2.7 \quad \Delta_F5.2$
 $\Delta_{\theta}2.9 \quad \Delta_F4.1$	 $\Delta_{\theta}2.8 \quad \Delta_F5.0$
 $\Delta_{\theta}2.6 \quad \Delta_F5.6$	 $\Delta_{\theta}2.1 \quad \Delta_F6.6$
 $\Delta_{\theta}2.0 \quad \Delta_F2.9$	 $\Delta_{\theta}2.8 \quad \Delta_F2.7$

Table 6 – comparison of test (red) and best fit (blue) azimuthal and FFT data for SEM11_cry04. Δ_F indicated fitting error, Δ_{θ} orientation error.

The fitting process was then applied to a modelled crystal of the same dimensions, in similar orientations. The results are compared to the laboratory fitting in Figure 40, where it can be seen that modelling provides a much better fit than the laboratory data for azimuthal fitting. Orientation fitting accuracy is also more accurate using azimuthal fitting than FFT fitting, other than in the laboratory case.

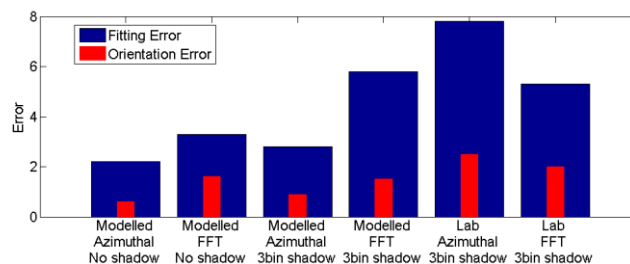


Figure 40 - Comparison of fitting error (blue) and orientation error (red) for SEM11_cry04 and modelled equivalent fitted using 15° azimuthal and FFT methods with and without shadowed region

Modelled data fitting carried out without the shadow applied shows a significant improvement over the same fitting with a number of bins removed. The more significant improvement is between modelled and laboratory fitting. The modelled data provides a much better fit than the laboratory equivalent when fitting with the azimuthal pattern method. This indicates that the model database does not represent the “real” crystal very well in this case, possibly because of a strong dependence of scattering patterns on how pristine the

crystal is. Interestingly, the FFT method appears more accurate for the laboratory data than the modelled one. This suggests that the FFT may be less accurate for the unusual case of pristine crystals, but more “forgiving” for crystals with surface details such as those seen on the crystal in question.

In order to further improve fitting accuracy, the azimuthal resolution was increased from the 24 azimuthal bins of the SID-2 detector to 36 and then 72. These resolutions are easily achievable using the SID-3 instrument and the laboratory rig. In the same manner as with the SID-2 equivalent direct pattern matching, rather than rotating the scattering pattern with respect to the angular bin mask, the angular bins were rotated themselves, in single bin increments. This means that the number of azimuthal orientations increased with increased azimuthal resolution. Computation time is increased too, since there are more data points to consider per scattering pattern, as well as more orientations. The total number of comparisons per test pattern can be calculated as the product of the number of crystal sizes, aspect ratios, basal indentations, reference pattern orientations and the square of the number of azimuthal bins in the case of direct pattern comparison, or FFT coefficients for FFT comparison. The reason for squaring the number of azimuthal bins is that there are an equal number of azimuthal orientations per pattern as there are bins. Each bin is then compared to its equivalent on the test pattern.

The mean fitting and azimuthal error for these results is shown in Figure 41. Interestingly, the FFT for 10° wide azimuthal bins provides a superior fit to the 5° equivalent in this case. However, the 5° and 10° resolution patterns both showed dramatic improvement over the 15° case – with mean fitting errors of below 5.

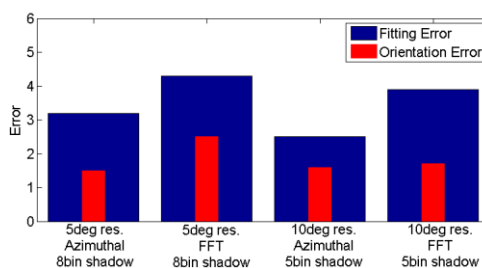


Figure 41 – Fitting (blue) and orientation (red) error for fitting of laboratory data binned into 5° and 10° wide azimuthal bins for azimuthal and FFT fitting.

Since the crystal is fitted well with higher resolutions compared to the low 15° (SID-2) azimuthal resolution, it seems that accurate fitting will be difficult to achieve using this instrument. However, this evidence has been obtained using data from the laboratory rig, which by necessity removes some information affected by the shadows, as mentioned previously.

We have seen with this case study that the direct pattern matching works better than the FFT fitting. Also, the increase of azimuthal resolution from 15° to 10° and 5° improves the fitting.

9.2. Case Study: Ice analogue Column

Another case study was performed using an ice analogue with a higher aspect ratio than in the previous section. At $29.4\mu\text{m}$ projected area equivalent diameter it is also somewhat larger. The length of the crystal is $40.4\mu\text{m}$, and the diameter $18.8\mu\text{m}$. This gives an aspect ratio of 2.1, and the basal facets are not indented. Figure 42 shows some images of the crystal, both optical and SEM. The SEM images show the surface of the crystal is not smooth, neither is the basal facet shown free of some detail. It is approximately symmetrical, although in the left image in Figure 42 one can see that the widths of the prismatic facets are not equal.

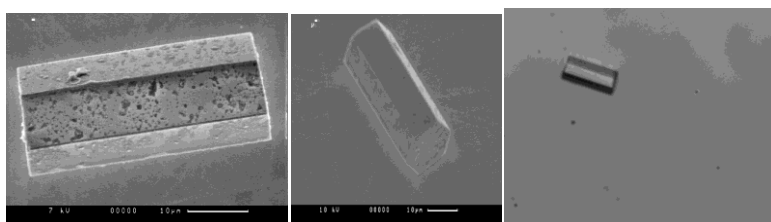


Figure 42 -SEM (left) and SEM (right) images of crystal SEM02_cryN1

The crystal was placed in the laboratory rig, and rotated in a similar manner to the crystal in the previous section.

9.2.1. Comparison of modelled and measured scattering patterns

The measured scattering patterns are compared to modelled equivalents in similar orientations. This provides some information on the difference between ideal crystals and those with surface detail or non-symmetry.

Figure 43 shows the comparison for some orientations of SEM02_cryN1 with a 5 degree azimuthal orientation in a rose plot format. It is clear that the patterns are dominated by the intense arc formed from the prism facets of the column, and that the ratio between this arc and the fine details is greater in the modelled than the measured data. In order to include the lower intensity region the patterns were scaled by taking the square root.

By comparing the square rooted scaled patterns, it becomes apparent that there is more detail in the off-arc areas of the patterns in the laboratory patterns than in the modelled patterns. There are many potential sources of this difference, such as surface roughness, asymmetry and/or camera noise. In order to reduce this effect, the mean value of the laboratory camera pixels in the region of interest is subtracted from each pixel. This has the effect of extracting the stronger details from the smoothed image.

Once both processes have been applied, the patterns compare much more strongly, which should provide a better fitting.

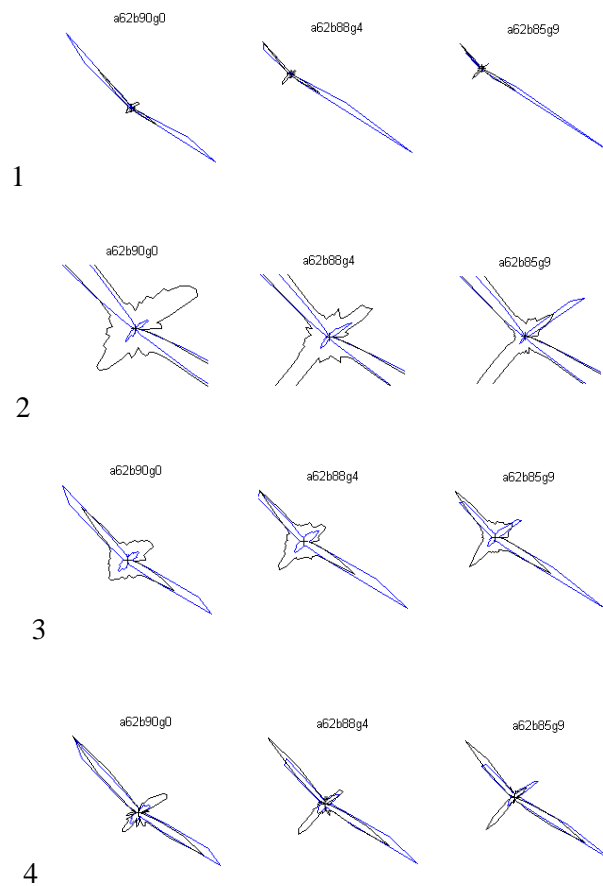


Figure 43 - Comparison of laboratory measured scattering pattern with modelled. 5° azimuthal resolution, and no square root or mean subtraction. Blue is modelled, black is lab. Row 1 is full pattern, 2 is a close up of the centre, 3 is scaled by square root 4 is mean subtracted and square rooted.

To see the effects of the above data cleaning, the patterns were fitted before and after the corrections. The calculated error reduction is from 7.2 to 3.0. From Figure 44, we can see that the fitting after the process matches the basal indentation and aspect ratio much more accurately, losing only some of the size information. The size information is dependent upon the absolute mean intensity of the scattering. Since the patterns are normalised against the mean, it is expected that some information about particle size will be lost here, since the intensity of forward scattered light is proportional to the particle size.

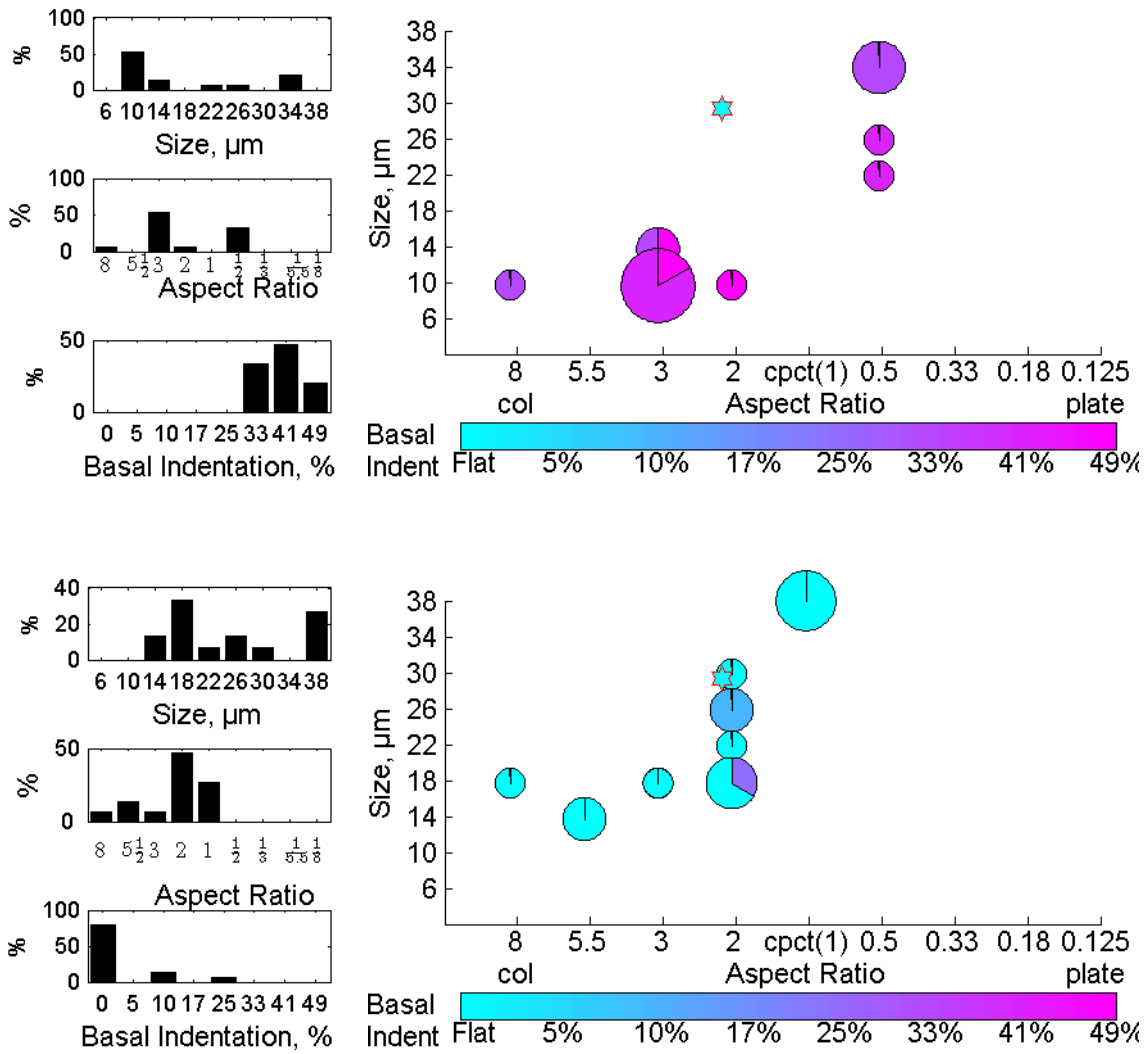


Figure 44 – SEM02_cryN1 data fitting before (top) and after mean subtraction and square root corrections (bottom)

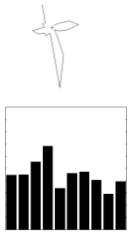
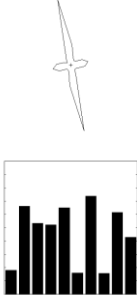
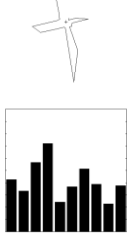
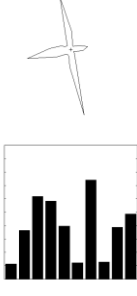
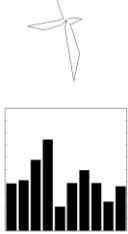
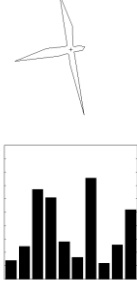
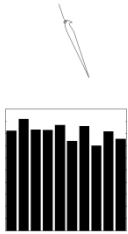
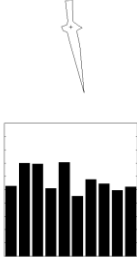
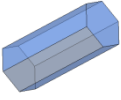
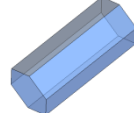
Euler angles	Lab pattern	RTDF pattern	View from above (incident beam)	View from left
$\alpha: 298$ $\beta: 90$ $\gamma: 0$				
$\alpha: 298$ $\beta: 86$ $\gamma: 2$				
$\alpha: 298$ $\beta: 81$ $\gamma: 5$				
$\alpha: 298$ $\beta: 55$ $\gamma: 19$				

Table 7 - Rose plots and bar plots of azimuthal scattering patterns and FFT from laboratory rig and RTDF model for four orientations of the SEM02_cryN1 crystal. “View from above” gives the orientation from which the laser is incident, and “view from left” is from the left as seen in the first view.

It is pleasing to note that there is now a similarity in terms of the FFT between the modelled and reference data as well as a good correlation between the azimuthal patterns. This indicates a high degree of accuracy in

the RTDF modelling of the scattering, as well as accurate representation of the size, shape and orientation of the crystal. However, features that attract the eye as being similar do not necessarily indicate a similar pattern overall.

Comparing the fitting in Figure 44 to the results from a fitting performed in the same manner (Figure 45), only on modelled data from a crystal with the same dimensions as the ice analogue, and in the same orientations, we see that the modelled fitting is significantly more accurate. This can be attributed to the imperfections on the surface of the crystal, which suggests that for real ice crystals which are rarely pristine, the fitting method is somewhat oversensitive to fine detail.

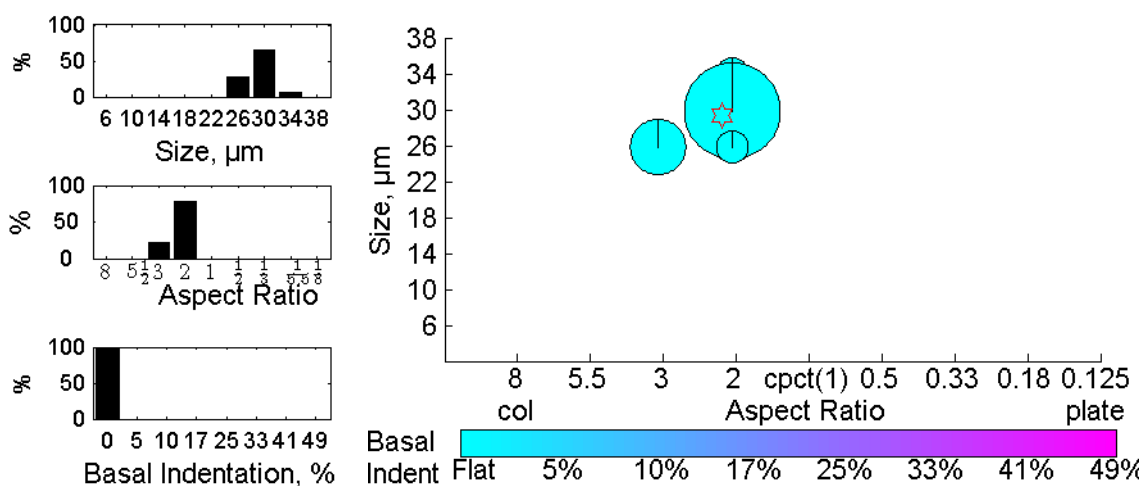


Figure 45 – As Figure 44 for modelled representation of SEM02_cryN1

9.3. HALO 2 AIDA Cloud Chamber Campaign

The AIDA facility at Forschungszentrum, Karlsruhe, Germany houses a cloud chamber capable of simulating the atmospheric conditions responsible for the formation of mixed phase and cirrus clouds. The SID-2 and SID-3 instruments (amongst a wide range of other single and multiple particle detectors) can be employed simultaneously to provide data.

The HALO 2 campaign was focused on ice crystal characterisation, using a variety of probes (including SID-2H and SID-3) [84]. Two experiments during this campaign were of particular interest, since relatively pristine hexagonal prisms were observed. This is demonstrated by the PHIPS instrument - see Figure 46. The PHIPS is a direct imaging instrument also attached to the AIDA chamber [85]. It comprises of two microscopes at 30° to one another, which image the particle simultaneously once a particle is detected in the sensing volume of the instrument. Unfortunately for the experiment in question the calibration for size has not been done at the time of writing, and so the images can only indicate aspect ratio.

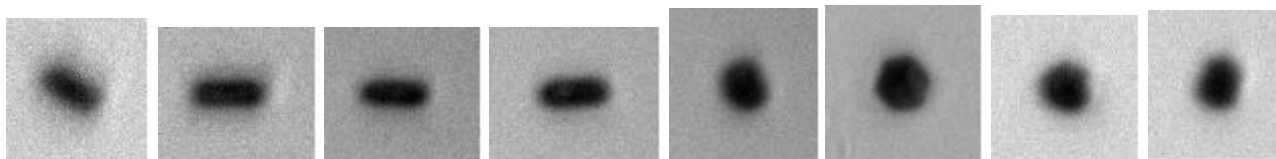


Figure 46 - PHIPS images from HALO 02, experiment 8⁶.

⁶ Data provided by Dr A. Abdelmonem

9.3.1. Individual pattern analysis

Data acquired by the SID-3 probe has been converted to AIP and fitted using the log scaling, with a bin width of 5° . The following is a discussion of similarities and differences between the modelled and test data of fitted patterns. The comparison of SID-3 image and RTDF 2D pattern is shown alongside a representation of the modelled crystal and orientation and a comparison between the AIP rose plots from both the modelled and test data.

Figure 47 shows a SID-3 pattern, which has been fitted to a small ($10\mu\text{m}$) column (aspect ratio of 5.5) with flat basal facets. The pattern is slightly curved upwards, indicating the top of the crystal is tilted away from the beam. The increased intensity on the left of the image indicates a rotation on the γ axis. Both of these features are represented in the RTDF plot, which has a similar curvature and asymmetric intensity along the arc to the SID-3 image. The rose plots are also similar, although the experimental pattern (red) shows a sharper secondary arc from the basal facets. This may indicate that the crystal has a lower aspect ratio than has been selected by the fitting method.

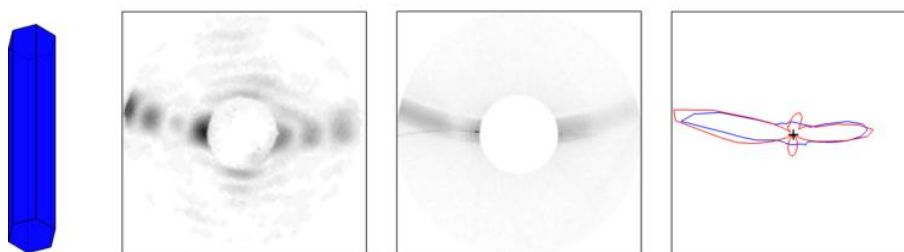


Figure 47 – SID-3 data compared to a best fit pattern from a $10\mu\text{m}$, 5.5 aspect ratio column with no basal indentation. Left to right: Representation of crystal as seen by incident beam; Image from SID-3 instrument; RTDF modelled representation of best fit pattern, logarithmically scaled; Comparison of experimental (red) and modelled (blue) rose plots.

From the same dataset, another column is selected - Figure 48. This column is in a similar orientation with a larger aspect ratio (8) and size ($14\mu\text{m}$). The basal indentation is clearly represented in both the RTDF and the SID-3 pattern by the broad arc below the centre of the pattern. This is represented in the rose pattern very clearly, although without a priori knowledge of the 2D pattern it would be difficult to correctly attribute the bulge at the bottom with a basal indentation. Another interesting point to make about this pattern is that the SID-3 pattern is at the lower limit of intensity. Large regions are without any form of scattering at all, and the JPEG compression artefacts are clearly present.

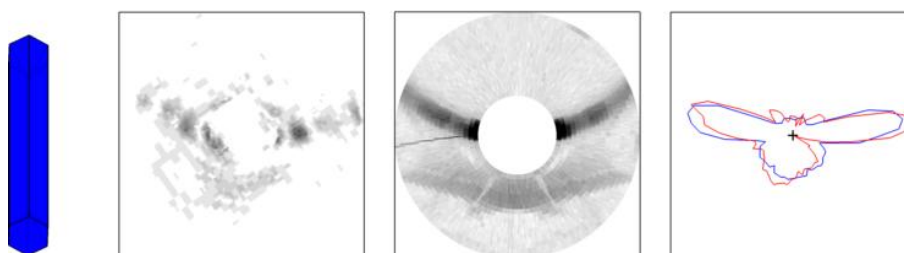


Figure 48 – As Figure 47 but for a $14\mu\text{m}$ crystal with an aspect ratio of 8 and basal intent of 14%.

As will be shown in the following section, an aspect ratio close to unity was more commonly observed using the AIP fitting from SID-3 data during this experiment - Figure 49. A small compact was fitted with a broad asymmetric arc indicative of a small crystal, and a rotation about the γ axis. The shape of the main arc in the rose pattern fits very well, although once again the secondary arc is not so well fitted.

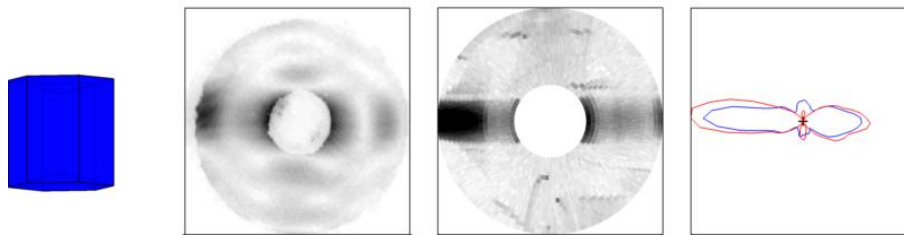


Figure 49 - As Figure 47 but for a 10 μ m, compact crystal with 14% basal indentation.

A somewhat larger compact is shown in Figure 50. The main arc is much less broad, and the secondary arc is more accurately represented in the rose plot. The continuous interference bands around the pattern seen in the SID-3 image indicate that the crystal likely has rounded edges, possibly due to the crystal beginning to melt.

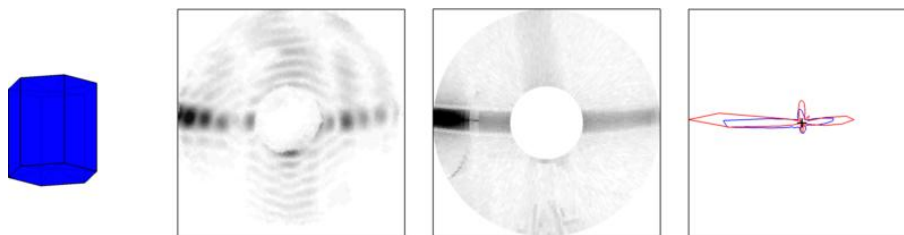


Figure 50 - As Figure 47 but for an 18 μ m compact with 7% basal indentation.

Not all AIP-fitted patterns appear correct when comparing the 2D patterns. The top row of Figure 51 shows a best fit pattern. The RTDF pattern has been oversaturated to show that it does not match the SID-3 one. Similarity in the rose pattern is brought about by bright spots above 20° scattering angle in the RTDF, rather than the solid arcs seen in the SID-3 image. One would expect to fit such a pattern to something more similar to the lower row of Figure 51, where a larger plate, with a lower aspect ratio causes a familiar six-pointed star. The increased intensity of three of the arcs suggests that the crystal in question is not regularly hexagonal in cross section, but rather that three of the basal sides are longer than the other, leading to three-fold symmetry. This crystal type is not represented in the current database.

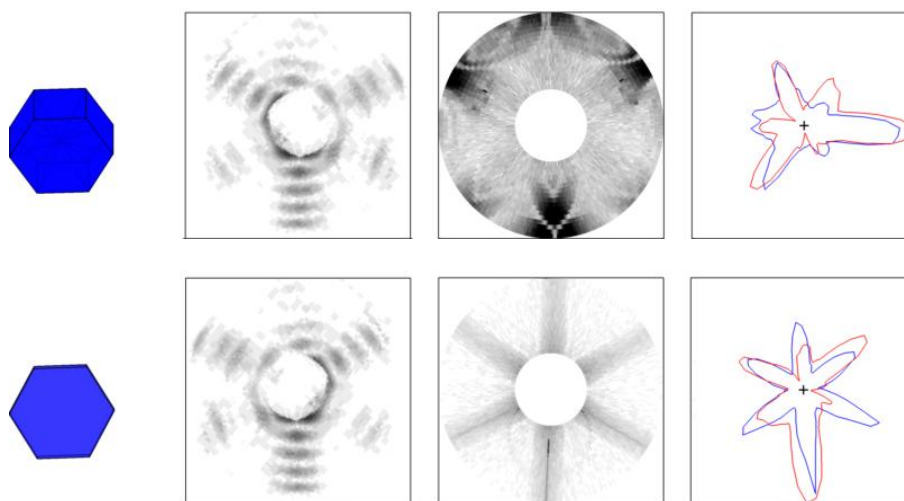


Figure 51 – As Figure 47 but for a (top) 14 μ m, 0.5AR plate, with 49% basal indentation $\beta=35^\circ$ and (bottom) a 22 μ m, 0.125AR plate with flat basal facets

Figure 52 shows a pattern fitted to a compact with a low β angle. The SID-3 pattern strongly resembles a plate, with six clear arcs emanating from the centre. The RTDF equivalent matches the SID-3 in breadth of peak, and in the relative intensities, as is clearly demonstrated in the rose pattern. However, it is likely that the crystal is in fact a plate, since none of the detail visible across the width of each arc is apparent in the SID-3 image. The basal indentation enhances the intensity offset of top two peaks, while smoothing the troughs. In this case, the basal indentation is perhaps mimicking the roundness of the edges of the crystal with this smoothing, since the roundness is creating a visible concentric pattern in the SID-3 image.

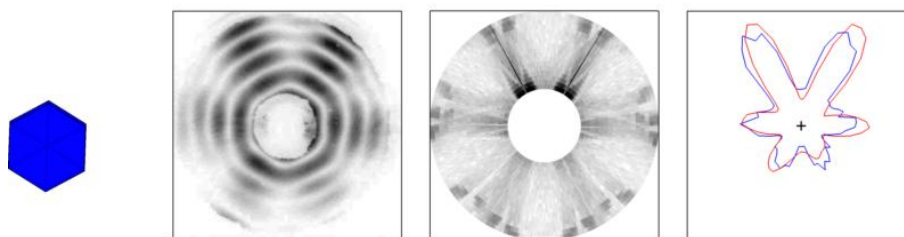


Figure 52 - As Figure 47 but for a 38 μ m compact with 49% basal indentation

Large compact crystals can result in an interesting effect. The rose plot derived from the SID-3 data (red) clearly shows eight peaks – four large and four somewhat smaller. Such patterns might be attributed to a rosette of two orthogonal prisms, but this fitting shows that this is in fact very likely a compact crystal, tilted such that two strong arcs run vertically and horizontally, caused by scattering from the prismatic facets and the horizontal edges shown on the crystal representation. The smaller peaks originate from the facets edges tilted at $\pm 45^\circ$ to the vertical (or horizontal).

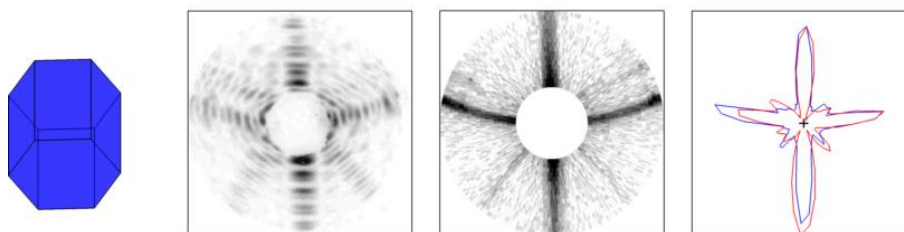


Figure 53 – SID As Figure 47 but for a 38 μ m compact with no basal indentation, with $\beta=45^\circ$

9.3.2. Aggregated data analysis

Some data was selected from the experiment to fit to the database. Images were classified as too saturated if they contained more than 10 pixels at the highest recordable intensity value (i.e. 255 for 8-bit data). A similar constraint was applied for pixels with a value of zero. In addition, images were chosen by eye to represent scattering from crystals, rather than droplets or other aerosols. Examples of discarded images are shown in Figure 54. Because of this selection process, it is to be noted that the following data does not fully represent the crystals present during the experiment.

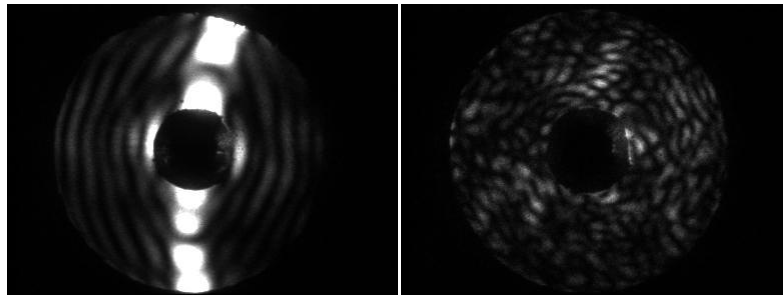


Figure 54 – Rejected patterns. Left: example of oversaturated scattering pattern. Right: scattering from large aerosol or rough ice particle.

An example of the effect of noisy data is shown in Figure 55. The noise in the SID-3 image causes the AIP to be smoothed. The crystal is fitted to a 6 μ m plate (AR: 0.3) with 28% basal indentation. The arcs are visible to the eye, and by their width and interference pattern the crystal can be identified as being somewhat larger than 6 μ m. The actual crystal may have had rough surfaces, as evidenced by patterns obtained from ice analogue crystals [69].

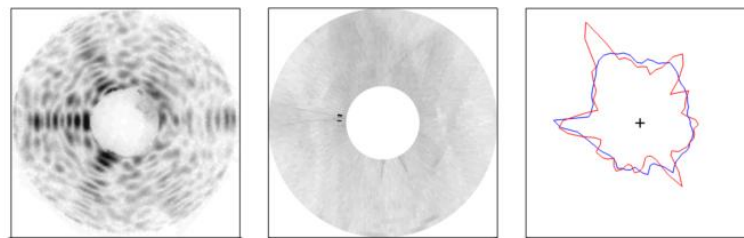


Figure 55 - As Figure 47 but for as an example of fitting noisy data

Small compacts make up the majority of the fits from this experiment, according to the SID-3 instrument (Figure 56). The same method was applied to the same data, but the angular ranges altered to those of the SID-2H instrument (azimuthal bin width of 12.9° and polar range of 9° to 20°), see Figure 57. The results are less well defined using the SID-2H equivalent data, as would be expected, however the fittings are very similar, both showing clustered solutions in a similar region, although there is more ambiguity in the SID-2H results.

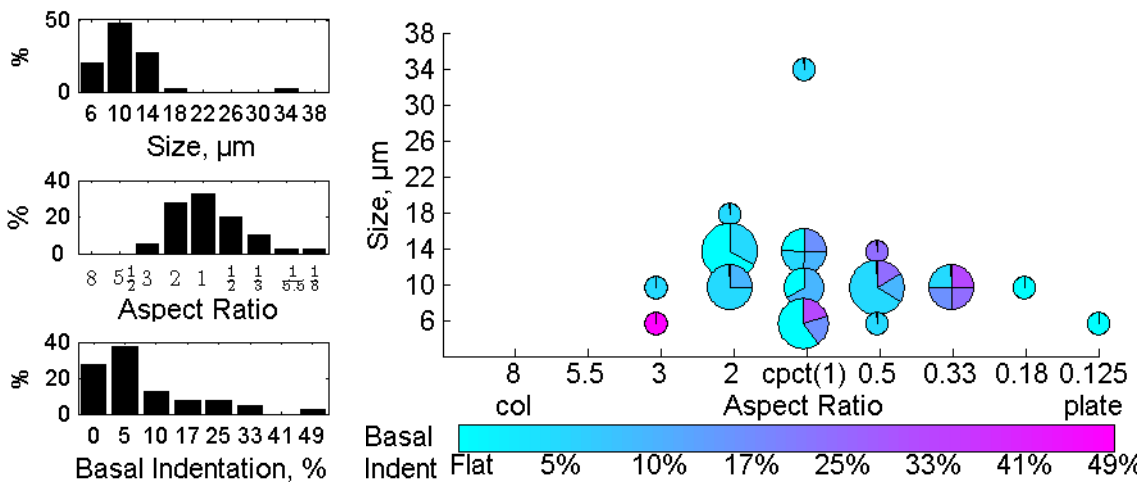


Figure 56 – Fitting of data from HALO 2, experiment 8 using 5° bin with AIP fitting method with polar range of 7° to 25°

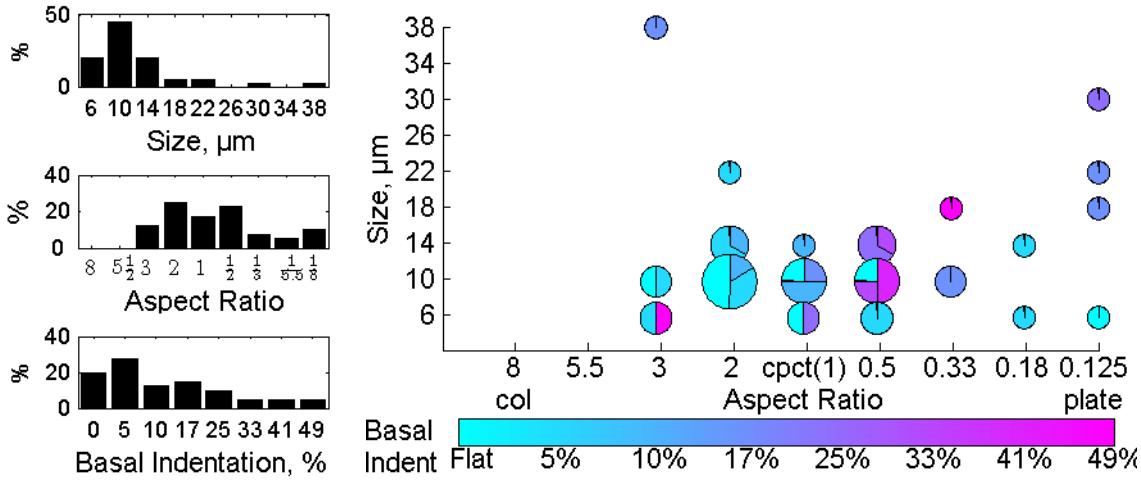


Figure 57 – Identical data source as Figure 56 using the SID-2H detector mask

9.3.3. Analysis of fitting saturated data

Localised high intensity regions of scattering patterns often saturate the pixels of the SID-3 detector. Saturation of the image causes the peaks of the AIP to be truncated. To investigate the effect of this, the data from the previous section was artificially saturated. AIP comparison was then performed using the same logarithmic scaling as for unsaturated data. The fitting results were compared for increasing percentage of saturated pixels per image.

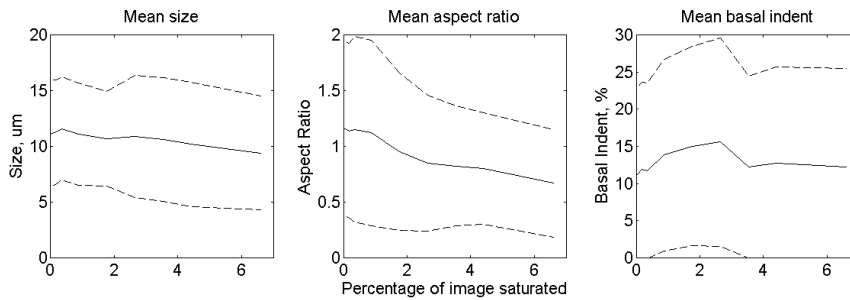


Figure 58 – Relationship of mean size, aspect ratio and basal indentation to percentage of image saturated. Dotted lines indicate the mean plus or minus the standard deviation.

Figure 58 shows that as the number of saturated pixels decreases, so does the mean aspect ratio of the fitting. The standard deviation of the aspect ratio also falls, indicating that a larger percentage of the crystals are fitted to plates. The range of sizes and basal indentations remains similar. It should be noted that in this case, the mean size is already close to the minimum value of the database (6µm).

Saturation of the image causes the scattering peaks of the AIP to be broadened. For plates orientated with a large β angle (i.e. the prismatic facets are close to normal incidence with the beam) reducing the aspect ratio causes a similar broadening of the intensity peaks.

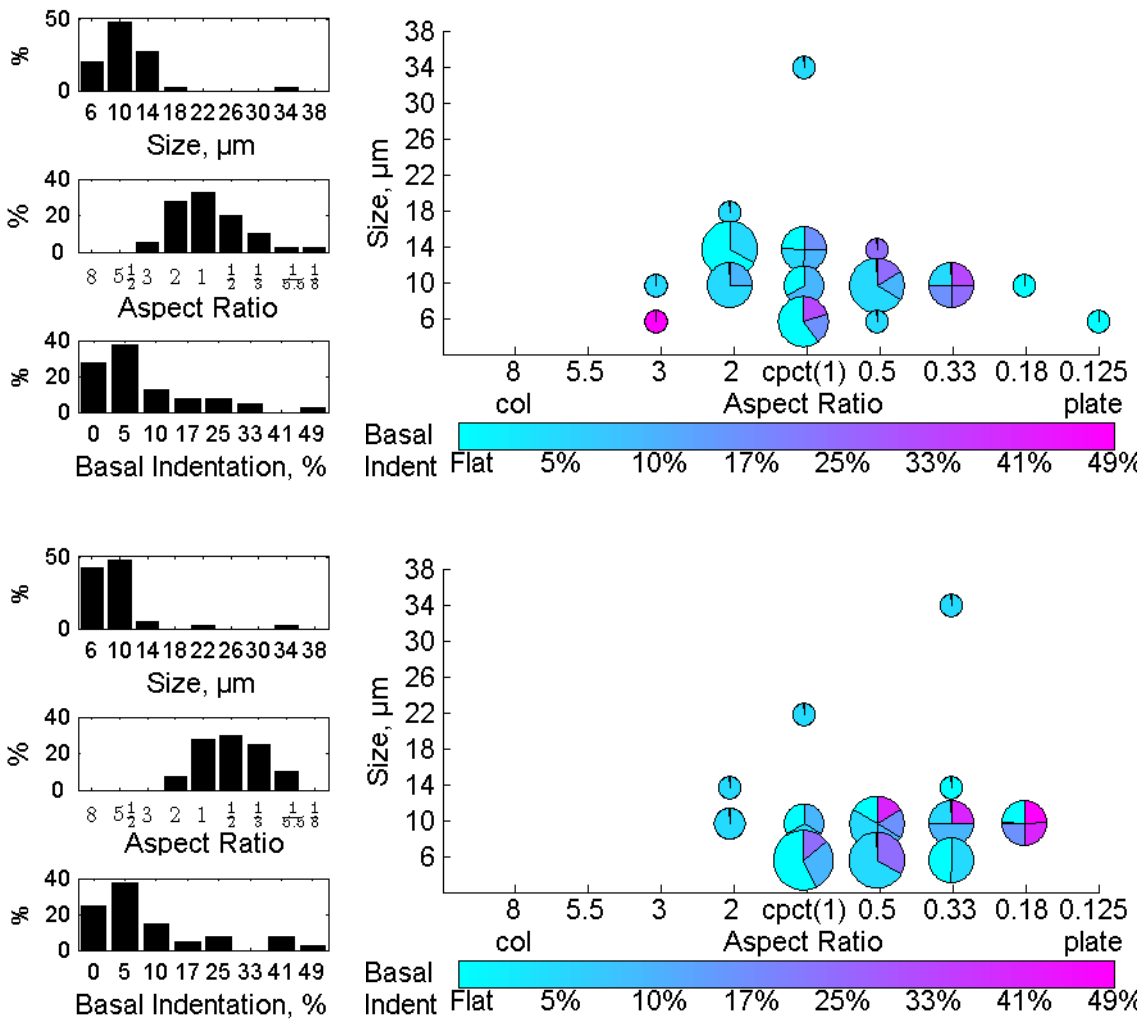


Figure 59 – Top: Fitting of unsaturated data from HALO 2, experiment 8 using 5° bin with AIP fitting method with polar range of 7° to 25°. Bottom: The same data with 6.6% of each scattering pattern saturated.

Figure 59 shows a comparison of the data fitted with unsaturated and saturated data. The cluster has moved down in aspect ratio, and slightly in size. Basal indentation is largely unaffected. The cluster remains intact and so the fitting technique may be deceptive, should the saturation of images not be accounted for.

10. Summary and further work

Data collected by the Small Ice Detector (SID) range of instruments has been gathered from numerous campaigns but has not had size and shape information recovered for individual patterns. This thesis has considered some of the challenges in solving the inverse scattering problem for cirrus ice crystal morphologies by comparison of 2D scattering patterns to modelled reference data.

A database of modelled scattering patterns was created using the *Ray Tracing with Diffraction on Facets* (RTDF) model for a range of hexagonal prisms. The RTDF model was chosen for its computational efficiency, effective size range, and accuracy in computing scattering patterns for single orientations. The database consists of scattering patterns from hexagonal prisms of various aspect ratios and sizes, with pyramidal basal indentations to approximate hollowness. The efficiency of the RTDF model allowed the database to grow to over 86 thousand unique scattering patterns.

The reference database allowed investigation into the relationship between crystal morphology and orientation, and scattering pattern. The basal indentation of a plate crystal clearly acts as a convex lens when the beam is incident on the base, diverting much of the intensity away from the centre of the scattering pattern. For columns with basal indents, secondary arcs are formed which do not pass through the centre of the pattern. For columns orientated with a β angle⁷ below 20°, the basal facets start to dominate the scattering pattern, causing a departure from the familiar arc caused by a tilted slit. The gamma angle is responsible for causing asymmetry in the pattern at all angles other than those close to 0° or 30°. For low aspect ratio (plate type) crystals, the opposite is true.

Data available from the SID-2 instrument detector layout bins the scattering pattern between 9° and 20°, with 24 azimuthal segments. By comparing the output of the RTDF model to similarly binned data, we see that many features of the scattering pattern are represented. The intense main arc from columns is represented strongly, however as the arc curves the peaks become wider, rather than angled. Small columns have similarly broad peaks, which could cause some ambiguity in interpretation.

Ice analogue crystals were employed to allow laboratory data to be collected in the form of scattering patterns from individual crystals in known orientations. The analogues are stable at room temperature, resistant to damage from manipulation, and have the same refractive index as ice. Importantly, they also grow with the same hexagonal symmetry seen in ice crystals.

To collect images of scattering patterns, an ellipsoidal screen was designed and used in conjunction with a digital camera and laser. The design of the reflector allows the capture of forward scattering in the region used by the SID-2 and SID-3 probes, as well as a narrow range of back scattered data for use in future work. Ice analogue crystals were manually selected for their size, symmetry and facet smoothness, using SEM and optical microscopy to check these criteria and to measure crystal dimensions. These measurements allowed accurate representation of the crystal geometry and orientation to be provided to the RTDF model.

Introduction of particles to the SID instruments was also investigated for the purpose of calibrating the detector response using calibration spheres in the case of SID-2 as well as for obtaining data from individual ice analogue crystals. The investigation showed that for the SID-2 instrument, gain calibration is an essential operation, since each detector element has a unique response. Particles suspended below the point of a needle can be ejected by imposing an electric field between the needle and a plate below the particle. This method allows data to be collected without interference from supporting structures, however the chance of recovering

⁷ For details of the orientation scheme, see chapter 8.2.2

the particle after ejection is low, and the orientation of the particle is unknown as it passes through the scattering volume. For valuable particles, the particle should be suspended on an anti-reflection plate such as is used in the laboratory rig described in chapter 5.1, whereby orientation can be controlled, and the particle is less likely to be lost.

Comparison of laboratory and modelled data for single orientation scattering patterns has shown good agreement. The model reproduces the two dimensional scattering pattern faithfully, including accurately producing features such as halo peaks. The shape of the halo peaks to the arcs is in agreement with laboratory data.

Fitting was performed using a variety of methods; the most successful of which is the direct comparison of binned azimuthal intensity patterns (AIP). This involves dividing the 2D pattern from the imaged scattering patterns from the laboratory rig or SID-3 probe into azimuthal segments which are binned over a polar range, analogous to data from SID-2 instrument, although a higher azimuthal resolution and greater polar range are possible. These patterns are then fitted to equivalent data from the modelled database by selecting the reference pattern with the smallest RMS difference to the test pattern. Increased azimuthal resolution shows improved accuracy, as does increasing the polar angle range of the bin – reducing the lower limit in particular. The resolution of the reference database of modelled scattering patterns was increased until there was no dependence on the accuracy of the fitting to the distance of a pattern to the nearest bin in the fitting space. In addition to the fitting of morphology, the orientation can be recovered using this method.

Scaling of the intensity of binned patterns was investigated, by either the square root or the logarithm. This removed the dependence of fitting on the highest intensity regions of the pattern, allowing low intensity regions of patterns to influence the fitting. Logarithmic scaling showed a greater improvement to fitting than square root for modelled data. Comparison of the magnitude of the fast Fourier transform of the AIP was also considered as a fitting method. It would remove the azimuthal dependence of a pattern, dramatically improving the efficiency of the fitting code, however proved to be highly inaccurate in practise.

Testing the fitting with a modelled database allowed investigation into the effect of increasing the polar range. It was found that including the low angle scattering provides a better fit of the data, to a larger degree than a similar increase in the maximum polar angle.

Moment invariants and asymmetry factor were discussed as possible parameters for discrimination. In the case of asymmetry factor, the discrimination power is too low to provide an accurate fit. Moment invariants may prove to have some use, however a suitable weighting of individual moments would have to be derived. Genetic algorithms or other forms of machine learning may be useful. Support vector machines have been used in the literature for such purposes.

Laboratory case studies show that small imperfections on the crystal surface influence the ability of the AIP fitting method to accurately fit a pattern. Scattering patterns were modelled for crystals with similar orientations and geometries to the laboratory crystal, and fitted to the reference database. The modelled data were fitted with a significant increase in accuracy over the fitting of laboratory data. This suggests that the role defects on the surface of ice and ice analogue crystals play on the accurate fitting to data from pristine modelled data is not insignificant.

Data from the SID-3 instrument was compared to the SID-2H instrument during the AIDA cloud chamber campaign HALO 2. Optical imagery of crystals present during this experiment confirmed the presence of morphologies included in the reference database. The fitting results are similar for each instrument, although the SID-2H results are less well defined than the SID-3 results which is due to the lower azimuthal resolution

and narrower polar range of the SID-2H instrument. This information will be useful in determining the configuration of the detector in future instrument designs.

This project has begun investigation into comparison of experimental data to a modelled database; however to further this work, the inclusion of more crystal shapes and other features should be included in the modelled database. In particular, prisms with less axial symmetry, surface roughness, and hollow bubbles within are all frequently witnessed in nature. Not all these features are currently trivial to model. In particular, surface roughness and triangular prisms are not currently supported by the RTDF model, although current work is targeted toward making this possible.

Beyond simple prisms, droxtals, rosettes and aggregates are common constituents of mixed phase clouds. Rosettes and aggregates pose a significant challenge in building a database of reference patterns, since an almost infinite number of possible geometries exist.

For the future of the SID range of instruments, and other particle detectors based on imaging of 2D scattering patterns, this project highlights the importance of an appropriate polar range, and azimuthal resolution. Direct comparison of the azimuthal patterns provides the most accurate method of fitting data, although real time fitting is not currently feasible. The lack of pristine crystals in nature makes the current state of the fitting method limited in applicability. The methods discussed can be used for other fields of study, wherever a model capable of producing an appropriate reference database exists.

Appendix A: Processes of the project

This appendix will detail the processes involved in gathering data, creating a reference database and fitting the test data in the form of annotated flowcharts.

A. 1 Data acquisition

The first stage of the process is to collect scattering patterns from individual ice analogue crystals.

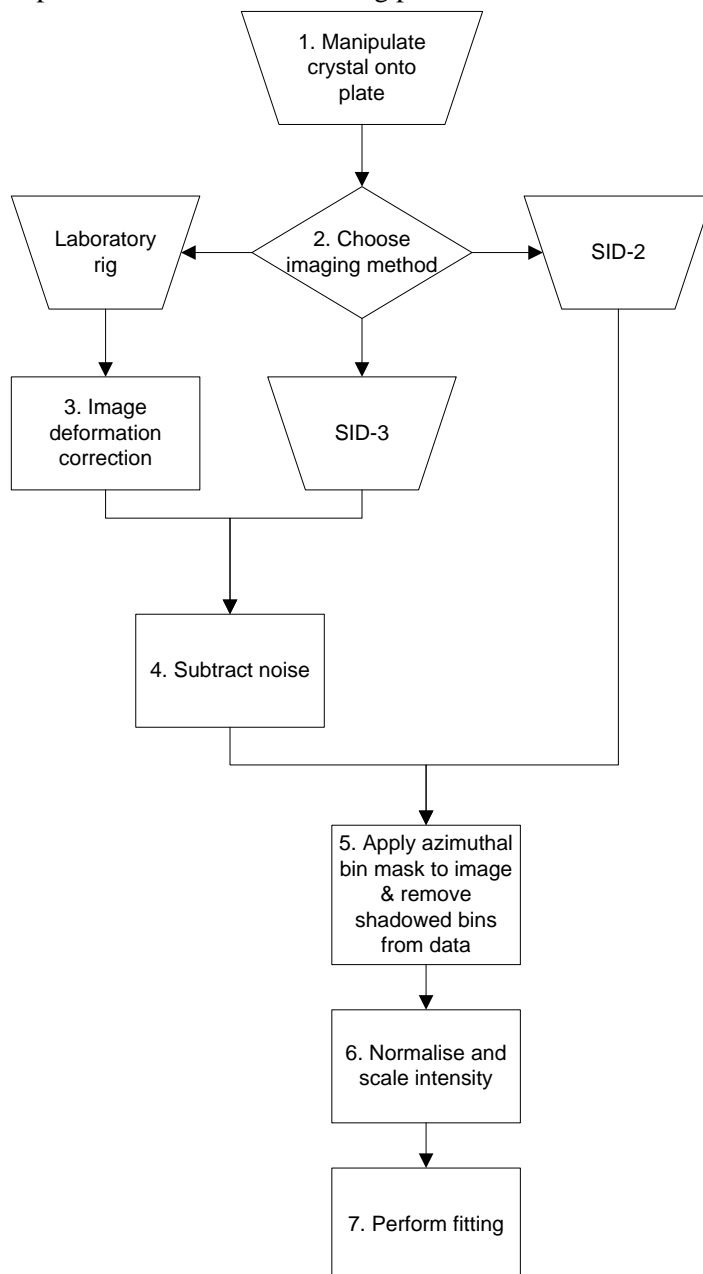


Figure 60 - Process involved in gathering scattering patterns from ice analogue crystals

1. The crystal first has to be manipulated onto the glass plate. This is done using a transmission microscope, since the contrast is higher than using a stereo or reflection microscope, and so the crystals are easier to see. The manipulation is performed using a sharpened tungsten needle attached to a micromanipulator. Touching the needle to the crystal causes the crystal to stick to the needle.

For larger crystals, a 3.5% glycerol solution was applied to the needle. To move the crystal from the needle to the plate, a second tungsten needle is used.

2. Either the laboratory rig (Chapter 5.1) or one of the SID instruments (Chapter 3) is used to collect the scattering pattern. When using the SID instruments, the triggering mechanism is bypassed, and instead data capture is initiated from a signal generator.
3. The lens used in the laboratory rig introduces image deformation. This is corrected using the Matlab script `imdefcorrection.m`. This corrects for barrel distortion and centres the image.
4. Noise can be subtracted from a laboratory or SID-3 image by subtracting the mean pixel intensity from every pixel. This is part of the same Matlab script as point 5 - `img2as_mask_forgui.m`.
5. The Cartesian grid of pixels is binned using a pre-determined azimuthal mask (created using `createASMask_forgui.m`). Pixels on the boundary of azimuthal bins have their intensity divided between both bins relative to the area of the pixel in each bin.

For laboratory or SID-3 data the shadow caused by the supporting rod of the plate is removed automatically, by comparison of a blank image to a binary image of the reflector with the supporting arm in place. In the case of the SID instruments, the effected bins are manually determined by triggering the probe with the rod in place, but no particle in the scattering volume. This is done in Matlab script `img2as_mask_forgui.m`.

6. At the expense of storage space it is possible to normalise and scale the data at this point. Doing so reduces the computation time of the fitting program for normalised and/or scaled data. Matlab script `as2cpp.m` or `as2cpp_norm.m` is used.
7. The data is now in a suitable state to be passed to the fitting program.

A. 2 Generation of reference database

There are three main steps to creating the crystal database. Firstly crystal geometry files are created for input to the RTDF code. The RTDF code creates a 2D scattering dataset with 1° resolution in both azimuthal and polar dimensions, up to 90° polar angle. This is then binned between the polar angles and at an azimuthal resolution (such as those of the SID-2 instrument) decided upon by the user. This data represents the azimuthal intensity pattern, which can then be transformed using the FFT method, or other methods as required, or used directly by the fitting program.

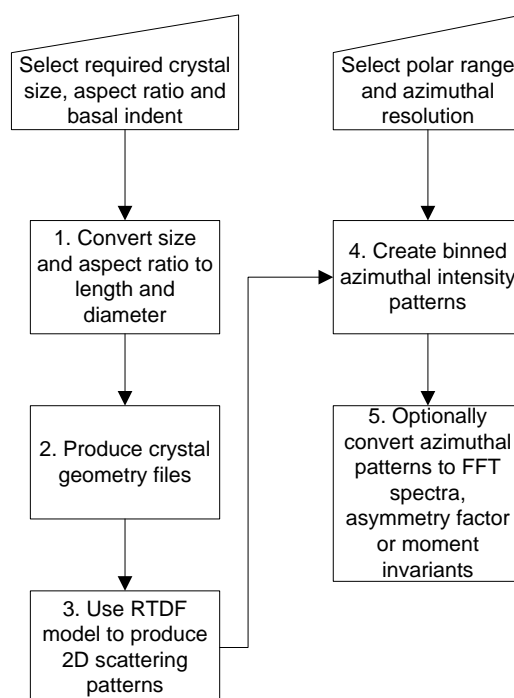


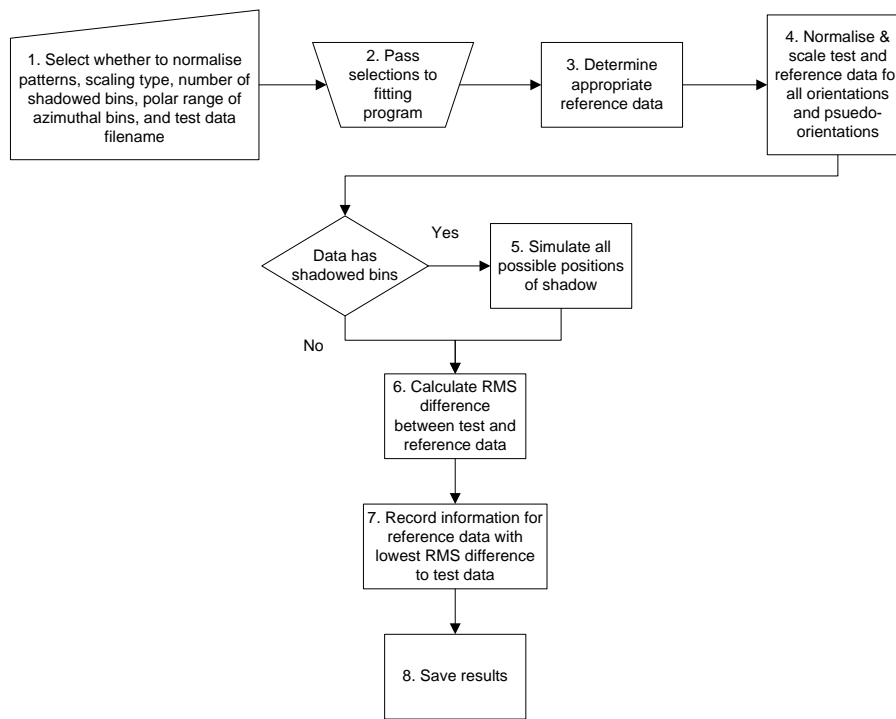
Figure 61 - Process involved in creating reference database

1. Conversion to projected area equivalent diameter (size) and aspect ratio from length and diameter is accomplished with the Excel worksheet `crystal sizes.xlsx`. A conversion factor from aspect ratio and size to length of a prism has been determined from analysis of the size of a range of crystal geometries using the FORTRAN program `d_rt_new_diff.f90` provided by E. Hesse.
2. Crystal geometry files are created using a modified FORTRAN program provided by D. McCall named `allhexcolumn_CJS.f90`. This takes a list of crystal length and diameter in microns and basal indentation as a percentage of length, and outputs a crystal geometry file for each.
3. The RTDF code provided by E. Hesse has been modified to run multiple crystal geometry files consecutively and independently. It is named `scattering0408.f90`, which relates to the April 2008 version of the program. It takes approximately an hour to run a single crystal geometry file through 133 orientations, one million incident rays, 10 ray interactions and 100 total internal reflections on a single 2.33GHz core. For the 648 geometries present in the reference database, this was done on eight cores over 92hours. This only needs to be done once per crystal geometry, since the azimuthal patterns can be extracted from this data as required – see point 4.
4. The modelled data is binned into azimuthal scattering patterns, which can be used in the fitting program. Files are saved for each geometry, azimuthal resolution and polar range combination separately, and accessed automatically by the fitting program.
5. The data can be converted into FFT, asymmetry factor or moment invariant data using `as2fft.m`, `as2af.m` or `as2mi.m`.

A. 3 Fitting test data to a reference database

This section will describe the processes used for fitting test data to the reference database. The method detailed below is written in C++. In initial tests the entire database was loaded into Matlab as a four dimensional array (binned intensity values for size, aspect ratio and basal indent). This manner of fitting is very slow to start, and very memory intensive, however once loaded is very fast to run. The move to a C++ program and loading the reference files one at a time was made to enable expansion to a larger database, and

to move from a single computer to a cluster of processors. The fitting now takes approximately 1.5 seconds per crystal for an azimuthal array with an azimuthal resolution of 5° .



1. Inputs to the program are chosen manually.
2. At this point, a Matlab script (`run_fitting_func.m`) splits the input file into eight approximately equal files. This enables the fitting program to be run as eight separate instances, thus making the most use of the eight cores available to a single machine of the processing cluster.
3. The fitting program (`main.cpp`) determines the appropriate reference data based on the azimuthal resolution of the data, the polar range and whether or not it has shadowed pixels.
4. The test and reference data is normalised and/or scaled, as required. Each test crystal/orientation is compared individually against each of the reference crystals and orientations. Pseudo-orientations are required to remove azimuthal dependence. This step is skipped for non-azimuthally dependent data, such as FFT or asymmetry factor.
5. If the data has shadowed bins, then the appropriate number of bins is removed from the pattern, in all possible permutations. This may be performed on the reference data, and saved as a separate reference file, to trade storage space for decreased computation time.
6. The RMS difference between the test pattern and the reference pattern is computed.
7. For the reference crystal with the lowest RMS difference to the test pattern, size, aspect ratio, basal indentation, RMS value, alpha, beta and gamma Euler angles are recorded.
8. The output data is saved by the C++ program for the files it was passed by the Matlab script in point 2. The Matlab script then re-combines the output files in the reverse of the process used to run multiple instances of the fitting program. The filename of the output file will be the input filename appended with `_output.dat`, as well as information regarding the scaling and fitting type.

A. 4 Data processing graphical user interface

In order to streamline the processes outlined in the sections A. 1 and A. 2, a graphical user interface (GUI) was created - Figure 62. This GUI allows the majority of the data processing to be performed without calling the Matlab scripts individually. The scripts responsible for each stage were turned into functions to allow them to be called by the GUI. Often the same file is used as both a script and a function.

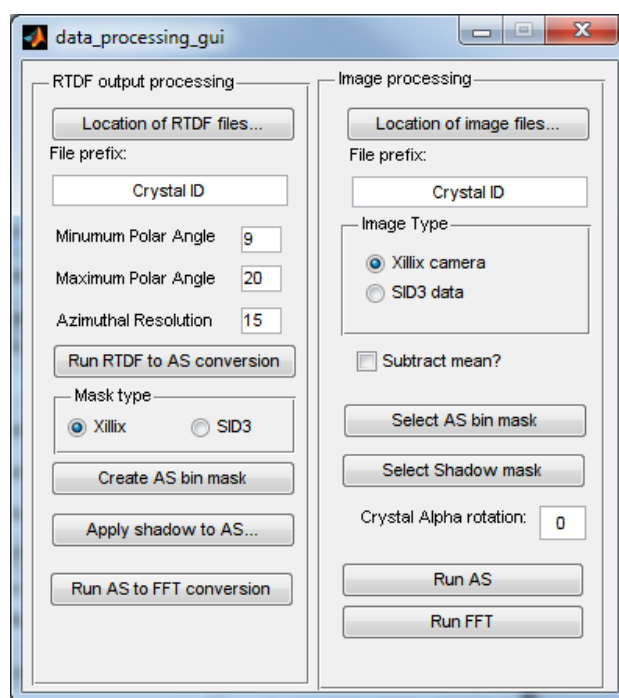


Figure 62 - GUI used to process and fit data

The discussion will follow the data flow from conversion from RTDF modelled output to displaying output of the fitting.

A. 4.1 “RTDF output processing”

The first function of this GUI is to convert the data from the RTDF model to a set of azimuthal intensity patterns. The first button selects the location of the RTDF output files. These are files for individual crystal geometries containing 2D scattering at 1° resolution up to a polar range of 90° . The “File Prefix” text box allows the user to limit the selection of RTDF files by their prefix. Usually, this will be left blank, in order to use all files.

The minimum and maximum polar angles are then set, along with the azimuthal resolution. The button “Run RTDF to AS conversion” performs the conversion to azimuthal intensity patterns using the `rtdf2as_forgui.m` file.

A mask file should also be created with the same polar and azimuthal settings as the azimuthal intensity patterns. This can be done for either the Xillix camera (used in the laboratory rig) or the SID-3 instrument as selected in the “Mask Type” box. The function for this is `createASmask_forgui.m`.

To apply a shadow to an azimuthal bin mask, the “Apply shadow to AS...” button prompts the user for a binary image from the camera with shadowed pixels marked. This is combined with a mask file (for which the user is also prompted) and a shadowed mask file is produced.

The button “AS to FFT conversion” converts the azimuthal intensity pattern to the FFT data used in the fitting program. `as2fftnorm_forgui.m` performs this computation.

A. 4.2 “Image processing”

This section of the GUI takes images from the laboratory or SID-3 instrument and bins them into an azimuthal intensity pattern and FFT data set. It loads the image files according to a directory and the beginning of the filename (“Location of image files” and “File prefix”).

The choice of “Image Type” identifies which type of mask should be opened. “Subtract mean?” refers to the option of subtracting the mean intensity of all pixels from each pixel in order to remove noise from the pattern.

“Select AS bin mask” and optionally “Select Shadow mask” allow the user to apply a shadowed azimuthal intensity pattern to the image.

The alpha rotation angle of the crystal on the plate should be measured manually and entered in the box entitled “Crystal alpha rotation.” This angle will then be stored in the subsequent data files.

“Run AS” and “Run FFT” create the azimuthal intensity patterns and FFT data respectively. The relevant Matlab files are `img2as_mask_forgui.m` and `as2fftnorm_forgui.m`.

Appendix B: Viewing of fitted results

This appendix shows a GUI built in Matlab for the purpose of viewing the nature of fits obtained by the fitting program. It is capable of loading the same input file as would be passed to the fitting program (Chapter A. 3) and the associated output file, then comparing the test pattern and the best fit reference pattern. The filename of the GUI is `viewer_2ds.m`.

Figure 63 shows a screenshot of the application. The “program directory” button (point 1) allows the directory containing the program, reference database and images of modelled scattering patterns to be manually selected. This allows the application to be moved from one computer to another, although the size of the database and images is approximately 230 GB.

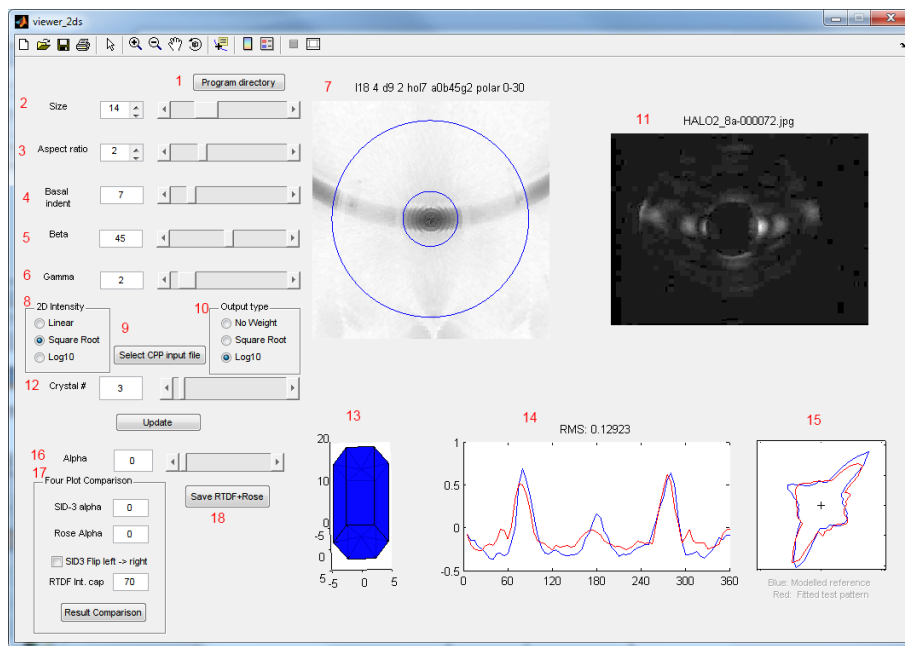


Figure 63 - Screenshot of GUI used to compare test data with best fit result

Points 2-6 indicate the size (μm), aspect ratio, basal indentation (% of length) beta and gamma Euler angles (in degrees) of the displayed data. These can be manually adjusted to any combination present in the database.

A 2D representation of the modelled scattering pattern is shown at point 7. The blue rings represent the limits of the polar range of the SID-3 instrument; 7° and 25° . The title of the plot shows the length ($18.4\mu\text{m}$), diameter ($9.2\mu\text{m}$), basal indentation (7%), alpha (0°), beta (45°), gamma (2°), Euler angles of the best fit modelled crystal and the minimum and maximum displayed scattering angles ($0\text{-}30^\circ$). This is also the filename of the image file. Saving each scattering pattern as a separate file (as opposed to loading the model output and rendering an image) dramatically increases the speed at which the patterns can be displayed.

Point 8 adjusts the scaling of the modelled reference scattering pattern in point 7.

The “Select CPP input file” (point 9) refers to the file passed to the fitting program, and displays a standard dialogue to select the file. In conjunction with the selection made in point 10, the program will then load the input data, and the best fit modelled data, as well as an image from the SID-3 instrument if available. The image will be displayed at point 11, labelled with the filename of the SID-3 file. This operation will cause the sliders and values in points 2-6 to update to the best fit of the first crystal in the input file. The appropriate modelled image is also shown, scaled as per manual selection in the “2D selection” box (point 7).

A 3D representation of the crystal is displayed at point 13, with axis in μm , with the incident beam normal to the screen, and passing from front to back. A line plot comparing logarithmically scaled data is shown at point 14, labelled with the RMS difference between test and reference patterns as calculated by the fitting program, scaled as per the selection in the “Output type” box (point 10). Square root scaled data is shown in a rose plot at point 15.

The “Crystal #” slider (point 12) indicates which crystal from the input file is displayed.

The alpha rotation (point 16) allows the logarithmically and square root scaled reference patterns to be rotated about the alpha Euler angle with respect to the test pattern. The RMS is re-calculated as per the scaling type selected in the “Output type” box (point 10).

The “Four Plot Comparison” (point 17) box creates plots such as the one in Figure 64. The rotation of the SID-3 image and the rose plot can be altered using “SID-3 alpha” and “Rose alpha” respectively. It is also possible to mirror the SID-3 image vertically, and cap the intensity of the modelled data to a percentage of its original value.

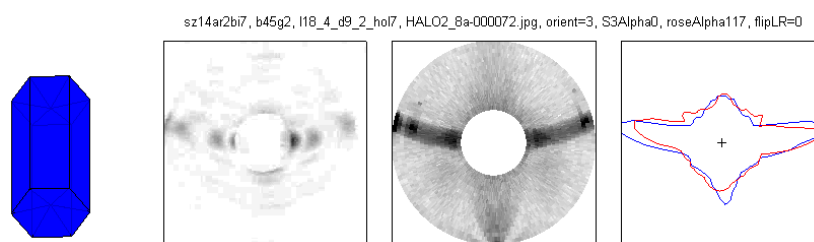


Figure 64 - Example of output from GUI

Finally, the “Save RTDF+Rose” button (point 18) allows a superposition of the 2D modelled pattern and the associated square root scaled rose pattern to be saved, such as that in Figure 65.

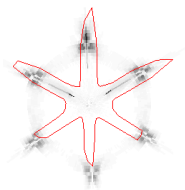


Figure 65 - Example of superposition of rose pattern and 2D modelled scattering

Appendix C: Laser characterisation

The laser used is a Melles Griot 05-LOR-161 helium neon LASER. The wavelength is 612nm, the power 4mW. In order to be able to focus the beam onto the crystal, the location of the internal beam waist was determined such that the external focus produced by an arbitrary lens can be calculated using the formulae developed by Self [86]. To determine the internal beam waist position, the external focus from a lens of known focal length was found experimentally, using the setup described in Figure 66 below.

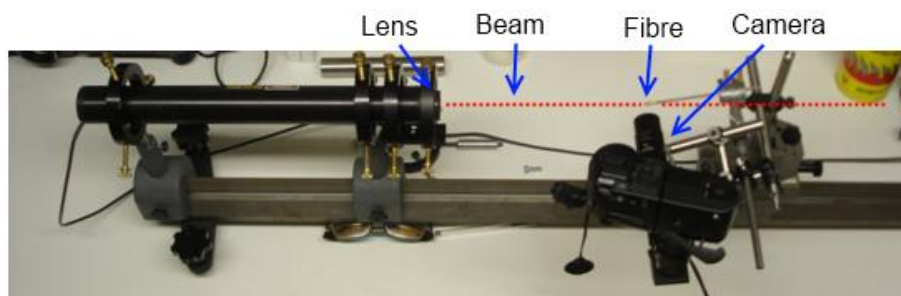


Figure 66 - Laboratory set up to measure focus of laser

To measure the diameter of the beam along its length, the laser was orientated so it was horizontal and parallel to the optical bar. Then a stand was erected on a translational stage, for a digital camera with a microscope lens. A 50 μ m diameter fibre was positioned in the camera's field of view, and held stationary with respect to the lens. By moving the camera and the fibre together, the fibre was positioned in the laser beam. The translation of the mount was then used to move the fibre along the beam, whilst observing the illuminated length of fibre.

List of figures

Figure 1 - The ray paths which cause 22° (left) and 46° (right) halos [9]	13
Figure 2 - SID-2 Instrument with electronics exposed.	16
Figure 3 - Diagram of SID-2 optical path. Red arrow indicates the incoming particle. Light blue lines indicate the path from scattering volume to trigger detectors. Green cone indicates the captured forward scattered light.	17
Figure 4 - SID-2 (left) SID-2H (right) detector layouts showing inner and outer rings of azimuthal bins.....	17
Figure 5 - Electrostatic Ejection setup: Crystal is ejected from needle to SEM grid through the scattering volume of the SID2 laser while being observed by microscope	18
Figure 6 - Laboratory setup used to nebulise a suspension of microspheres for calibration of SID-2 detector	19
Figure 7 – Mean response of SID-2 instrument to spherical particles.....	20
Figure 8 - A selection of ice analogues imaged by SEM.....	22
Figure 9 – Schematic showing laboratory rig layout.....	23
Figure 10 – Three images of crystal sem11_cry04. Left: SEM image with basal facet shown. Middle: SEM image from directly above. Right: Optical image for measurement.....	24
Figure 11 - Comparison of SEM11_cry04 (left) measurement and RTDF model (right). From point A the main arc extends via C (46° halo peak) and B (22° halo peak) through the image centre. Point D indicates the position of light diffracted through a basal facet.	25
Figure 12 - Comparison of RTDF (red) and laboratory (blue) azimuthal patterns at narrow polar angle ranges. Top: Polar angle 13°. Bottom: Polar angle 23°. Left: linear intensity pattern. Middle: Square root scaling of intensity pattern. Right: Log10 scaling of intensity pattern.	26
Figure 13 - Comparison of phase functions for RTDF, laboratory and Fraunhofer for crystal SEM11 cry04 .	26
Figure 14 - Comparison between imaged (blue) and modelled (green) scattering pattern along the main arc.	27
Figure 15 - Crystal dimensions. Basal indentation is referred to as a percentage of the length. Length and diameter are both referred to in micrometers.	29
Figure 16 - Rotating the mask with respect to the pattern causes local peaks to be spread over more than one bin, and vice versa	30
Figure 17 - Comparison of scattering pattern intensity scaling. Left: Linear. Middle: Square root. Right: Log10.....	31
Figure 18 – Euler angles of rotation in order of execution	31
Figure 19 - Ray path of bright spot at 20° at 10° beta orientation.....	32
Figure 20 – Geometric optics representation to demonstrate that increasing the visible cross section of one side facet increases the scattered intensity on the opposite side.....	34
Figure 21 - Comparison of two views of the same column at different beta orientation angles. Red lines indicate region of border of the cross section from basal facets. Incident beam normal to the page, passing from front to back. X, Y and Z are width, depth and height in laboratory frame in microns.....	34
Figure 22 - Examples of scattering patterns from crystals with basal indentations. Taken by SID-3 at the ACI03 experiment	37
Figure 23 - Low aspect ratio crystals with basal indentation acts as a concave lens.....	37
Figure 24 - Scattering pattern from 38µm crystal with aspect ratio 0.3 and basal indentation of 28% (left) and 49% (right).....	38
Figure 25 - Mean fitting error plotted against distance from nearest bin in fitting space.....	41
Figure 26- Example of 6µm, unity AR, compact crystal - fitted using azimuthal pattern matching.....	42

Figure 27 - Example of 25 μ m, 3 AR, flat crystal - variation of 0.16 from nearest reference bin, fitted using azimuthal pattern matching	42
Figure 28 - Off-orientation patterns fitted to the low orientation resolution azimuthal pattern reference set. ...	43
Figure 29 - Off orientation comparison with high orientation resolution azimuthal pattern fitting set.	44
Figure 30 - Mean error for asymmetry function fitting over range of azimuthal resolutions and polar ranges	46
Figure 31 - Example of modelled crystal fitted by asymmetry factor comparison with an azimuthal resolution of 20 $^{\circ}$, and a polar range of 9 $^{\circ}$ -20 $^{\circ}$. The error of fitting is 6.	46
Figure 32 - Example of fitting of column to the reference database based on discrimination by moment invariants.....	48
Figure 33 - from left to right – 2D scattering pattern from RTDF modelled column (rings represent area recorded by the SID-2 detector), polar plot of square root intensity of SID-2 pattern, normalised FFT spectrum of polar plot.....	49
Figure 34 - Comparison of mean error while fitting a test data set to using different measures of best fit.	50
Figure 35 – Comparison of mean error in fitting over different azimuthal resolutions and polar ranges using log10 scaled AIP fitting	50
Figure 36 - Comparison of mean error in fitting over different azimuthal resolutions and polar ranges using square root scaled AIP fitting.....	51
Figure 37 - Comparison of accuracy of orientation determination for various azimuthal resolutions and polar ranges fitted with logarithmic (left) and square root (right) intensity scaling.....	52
Figure 38 - Results of FFT pattern fitting of SEM11_cry04 to reference database. The Δd is 0.39, and error is 5.2.	55
Figure 39 – Results of direct pattern matching for SEM11_cry04. The Δd is 0.39, and error is 4.3.....	55
Figure 40 - Comparison of fitting error (blue) and orientation error (red) for SEM11_cry04 and modelled equivalent fitted using 15 $^{\circ}$ azimuthal and FFT methods with and without shadowed region.....	56
Figure 41 – Fitting (blue) and orientation (red) error for fitting of laboratory data binned into 5 $^{\circ}$ and 10 $^{\circ}$ wide azimuthal bins for azimuthal and FFT fitting.....	57
Figure 42 -SEM (left) and SEM (right) images of crystal SEM02_cryN1	58
Figure 43 - Comparison of laboratory measured scattering pattern with modelled. 5 $^{\circ}$ azimuthal resolution, and no square root or mean subtraction. Blue is modelled, black is lab. Row 1 is full pattern, 2 is a close up of the centre, 3 is scaled by square root 4 is mean subtracted and square rooted.	59
Figure 44 – SEM02_cryN1 data fitting before (top) and after mean subtraction and square root corrections (bottom)	60
Figure 45 – As Figure 44 for modelled representation of SEM02_cryN1	62
Figure 46 - PHIPS images from HALO 02, experiment 8.	62
Figure 47 – SID-3 data compared to a best fit pattern from a 10 μ m, 5.5 aspect ratio column with no basal indentation. Left to right: Representation of crystal as seen by incident beam; Image from SID-3 instrument; RTDF modelled representation of best fit pattern, logarithmically scaled; Comparison of experimental (red) and modelled (blue) rose plots.	63
Figure 48 – As Figure 47 but for a 14 μ m crystal with an aspect ratio of 8 and basal intent of 14%.....	63
Figure 49 - As Figure 47 but for a 10 μ m, compact crystal with 14% basal indentation.....	64
Figure 50 - As Figure 47 but for an 18 μ m compact with 7% basal indentation.....	64
Figure 51 – As Figure 47 but for a (top) 14 μ m, 0.5AR plate, with 49% basal indentation $\beta=35^{\circ}$ and (bottom) a 22 μ m, 0.125AR plate with flat basal facets	64
Figure 52 - As Figure 47 but for a 38 μ m compact with 49% basal indentation	65
Figure 53 – SID As Figure 47 but for a 38 μ m compact with no basal indentation, with $\beta=45^{\circ}$	65

Figure 54 – Rejected patterns. Left: example of oversaturated scattering pattern. Right: scattering from large aerosol or rough ice particle.	66
Figure 55 - As Figure 47 but for as an example of fitting noisy data	66
Figure 56 – Fitting of data from HALO 2, experiment 8 using 5° bin with AIP fitting method with polar range of 7° to 25 °	67
Figure 57 – Identical data source as Figure 56 using the SID-2H detector mask.....	67
Figure 58 – Relationship of mean size, aspect ratio and basal indentation to percentage of image saturated. Dotted lines indicate the mean plus or minus the standard deviation.	67
Figure 59 – Top: Fitting of unsaturated data from HALO 2, experiment 8 using 5° bin with AIP fitting method with polar range of 7° to 25 °. Bottom: The same data with 6.6% of each scattering pattern saturated.	68
Figure 60 - Process involved in gathering scattering patterns from ice analogue crystals.....	72
Figure 61 - Process involved in creating reference database	74
Figure 62 - GUI used to process and fit data.....	76
Figure 63 - Screenshot of GUI used to compare test data with best fit result	78
Figure 64 - Exemple of output from GUI	79
Figure 65 - Example of superposition of rose pattern and 2D modelled scattering	79
Figure 66 - Laboratory set up to measure focus of laser	80

Bibliography

- [1] J.P. Fugal, R.A. Shaw, E.W. Saw, and A.V. Sergeev, "Airborne Digital Holographic System for Cloud Particle Measurements," *Applied Optics*, vol. 43, Nov. 2004, pp. 5987-5995.
- [2] P. Amsler, O. Stetzer, M. Schnaiter, E. Hesse, S. Benz, O. Moehler, and U. Lohmann, "Ice crystal habits from cloud chamber studies obtained by in-line holographic microscopy related to depolarization measurements," *Applied Optics*, vol. 48, Oct. 2009, pp. 5811-5822.
- [3] R.L. Myers, *The basics of physics*, Greenwood Publishing Group, 2006.
- [4] L.(Vinci), *The notebooks of Leonardo da Vinci*, Babylon Dreams, 1977.
- [5] E. Hecht, *Optics*, Pearson Education, Limited, 2001.
- [6] T. Young and P. Kelland, *A Course of Lectures on Natural Philosophy and the Mechanical Arts: pt. I. Mechanics. pt. II. Hydrodynamics. pt. III. Physics*, Printed for Taylor and Walton, 1845.
- [7] M. Born, E. Wolf, and A.B. Bhatia, *Principles of Optics*, 1999.
- [8] T. Young and P. Kelland, *A Course of Lectures on Natural Philosophy and the Mechanical Arts*, 1845.
- [9] C.F. Bohren and D.R. Huffman, *Absorption and scattering of light by small particles*, 1983.
- [10] A.L. Givan, *Flow cytometry*, John Wiley and Sons, 2001.
- [11] H. Nakadate, E. Sekizuka, and H. Minamitani, "Validity of particle-counting method using laser-light scattering for detecting platelet aggregation in diabetic patients," *Electronics and Communications in Japan*, vol. 92, 2009, pp. 1-8.
- [12] P.P. Banada, K. Huff, E. Bae, B. Rajwa, A. Aroonual, B. Bayraktar, A. Adil, J.P. Robinson, E.D. Hirleman, and A.K. Bhunia, "Label-free detection of multiple bacterial pathogens using light-scattering sensor," *Biosensors and Bioelectronics*, vol. 24, Feb. 2009, pp. 1685-1692.
- [13] A. Khotanzad and Y. Hong, "Invariant image recognition by Zernike moments," *Pattern Analysis and Machine Intelligence, IEEE Transactions on*, vol. 12, 1990, pp. 489-497.
- [14] R.M. Haralick, K. Shanmugam, and I. Dinstein, "Textural Features for Image Classification," *IEEE Transactions on Systems, Man, and Cybernetics*, vol. 3, 1973, pp. 610-621.
- [15] P. Li and J.R. Flenley, "Pollen texture identification using neural networks," *Grana*, vol. 38, 1999, p. 59.
- [16] R. Sivaramakrishna, K.A. Powell, M.L. Lieber, W.A. Chilcote, and R. Shekhar, "Texture analysis of lesions in breast ultrasound images," *Computerized Medical Imaging and Graphics*, vol. 26, Sep. , pp. 303-307.
- [17] Warren Stanley, "Realisation of an Optical Tomography System using an Amplitude Modulation Technique," University of Hertfordshire, 2003.
- [18] S. Messenger, L.P. Keller, F.J. Stadermann, R.M. Walker, and E. Zinner, "Samples of Stars Beyond the Solar System: Silicate Grains in Interplanetary Dust," *Science*, vol. 300, Apr. 2003, pp. 105-108.
- [19] J. Worms, J. Renard, E. Hadamcik, A. Levasseur-Regourd, and J. Gayet, "Results of the PROGRA2 Experiment: An Experimental Study in Microgravity of Scattered Polarized Light by Dust Particles with Large Size Parameter," *Icarus*, vol. 142, Nov. 1999, pp. 281-297.
- [20] K. Grogan, S.F. Dermott, and D.D. Durda, "The Size-Frequency Distribution of the Zodiacal Cloud: Evidence from the Solar System Dust Bands," *Icarus*, vol. 152, Aug. 2001, pp. 251-267.
- [21] I. Chung and D. Dunn-Rankin, "In Situ Light Scattering Measurements of Mainstream and Sidestream Cigarette Smoke," *Aerosol Science and Technology*, vol. 24, 1996, p. 85.
- [22] J.M. Steinke and A.P. Shepherd, "Comparison of Mie theory and the light scattering of red

- blood cells,” *Applied Optics*, vol. 27, Oct. 1988, pp. 4027-4033.
- [23] R.A. Haugerud, D.J. Harding, S.Y. Johnson, J.L. Harless, C.S. Weaver, and B.L. Sherrod, “High-Resolution Lidar Topography of the Puget Lowland, Washington —A Bonanza for Earth Science,” *GSA Today*, vol. 13, Jun. 2003, pp. 4-10.
- [24] H.J. Zwally, B. Schutz, W. Abdalati, J. Abshire, C. Bentley, A. Brenner, J. Bufton, J. Dezio, D. Hancock, D. Harding, T. Herring, B. Minster, K. Quinn, S. Palm, J. Spinhirne, and R. Thomas, “ICESat's laser measurements of polar ice, atmosphere, ocean, and land,” *Journal of Geodynamics*, vol. 34, 2002, pp. 405-445.
- [25] K. Lim, P. Treitz, M. Wulder, B. St-Onge, and M. Flood, “LiDAR remote sensing of forest structure,” *Progress in Physical Geography*, vol. 27, Mar. 2003, pp. 88-106.
- [26] M.A. Lefsky, W.B. Cohen, S.A. Acker, G.G. Parker, T.A. Spies, and D. Harding, “Lidar Remote Sensing of the Canopy Structure and Biophysical Properties of Douglas-Fir Western Hemlock Forests,” *Remote Sensing of Environment*, vol. 70, Dec. 1999, pp. 339-361.
- [27] K. Aydin, T. Seliga, and V. Balaji, “Remote Sensing of Hail with a Dual Linear Polarization Radar,” *Journal of Applied Meteorology*, vol. 25, Oct. 1986, pp. 1475-1484.
- [28] M. Babin, A. Morel, V. Fournier-Sicre, F. Fell, and D. Stramski, “Light Scattering Properties of Marine Particles in Coastal and Open Ocean Waters as Related to the Particle Mass Concentration,” *Limnology and Oceanography*, vol. 48, Mar. 2003, pp. 843-859.
- [29] E. Hadamcik, J. Renard, G. Alcouffe, G. Cernogora, A. Levasseur-Regourd, and C. Szopa, “Laboratory light-scattering measurements with Titan's aerosols analogues produced by a dusty plasma,” *Planetary and Space Science*, vol. 57, Nov. 2009, pp. 1631-1641.
- [30] P. Kaye, E. Hirst, and Z. Wang-Thomas, “Neural-network-based spatial light-scattering instrument for hazardous airborne fiber detection,” *Applied Optics*, vol. 36, 1997, pp. 6149-6156.
- [31] L. Howard, *Seven Lectures on Meteorology*, 1843.
- [32] D.K. Lynch, K. Sassen, D.O.C. Starr, and G. Stephens, *Cirrus*, 2002.
- [33] ISO - International Organization for Standardization and ISO - International Organization for Standardization, “ISO - International Organization for Standardization.”
- [34] R.J. Cotton, S. Benz, P.R. Field, O. Möhler, and M. Schnaiter, “Technical Note: A numerical test-bed for detailed ice nucleation studies in the AIDA cloud simulation chamber,” *Atmos. Chem. Phys.*, vol. 7, Jan. 2007, pp. 243-256.
- [35] C.P.R. Saunders and A.S. Hosseini, “A laboratory study of the effect of velocity on Hallett-Mossop ice crystal multiplication,” *Atmospheric Research*, vol. 59-60, Oct. , pp. 3-14.
- [36] D.P. Wylie, W.P. Menzel, H.M. Woolf, and K.I. Strabala, “Four Years of Global Cirrus Cloud Statistics Using HIRS,” *Journal of Climate*, vol. 7, Dec. 1994, pp. 1972-1986.
- [37] A.J. Baran, “A review of the light scattering properties of cirrus,” *Journal of Quantitative Spectroscopy and Radiative Transfer*, vol. 110, Feb. 2009, pp. 1239-1260.
- [38] A.J. Heymsfield and J. Iaquinta, “Cirrus Crystal Terminal Velocities,” *Journal of the Atmospheric Sciences*, vol. 57, Apr. 2000, pp. 916-938.
- [39] V. Suomi, “The radiation balance of the Earth from a satellite,” *Ann. IGY*, vol. 1, 1958, pp. 331-340.
- [40] “VANGUARD 2 Satellite details 1959-001A NORAD 11,” <http://www.n2yo.com/satellite/?s=11>, 2009.
- [41] OECD, *Space technologies and climate change*, OECD Publishing, 2008.
- [42] H. Weickmann, “Die Eisphase in der Atmosphäre,” *H Weickmann - Berichte des Deutschen Wetterdienstes in der US-Zone*, vol. 6, 1947, pp. 49-50.
- [43] R.P. Lawson, A.V. Korolev, S.G. Cober, T. Huang, J.W. Strapp, and G.A. Isaac, “Improved measurements of the drop size distribution of a freezing drizzle event,” *Atmospheric Research*, vol. 47-48, Jun. 1998, pp. 181-191.

- [44] A.J. Heymsfield and G.M. McFarquhar, "High Albedos of Cirrus in the Tropical Pacific Warm Pool: Microphysical Interpretations from CEPEX and from Kwajalein, Marshall Islands," *Journal of the Atmospheric Sciences*, vol. 53, Sep. 1996, pp. 2424-2451.
- [45] R. Schoen, M. Schnaiter, Z. J. Ulanowski, & O. Moehler, "Ein neuartiges Geraet zur beruehrungsfreien Abbildung von Eiskristallen," *70th Ann. Meeting German Physical Society*, 2006.
- [46] J.W. Strapp, F. Albers, A. Reuter, A.V. Korolev, U. Maixner, E. Rashke, and Z. Vukovic, "Laboratory Measurements of the Response of a PMS OAP-2DC," *Journal of Atmospheric and Oceanic Technology*, vol. 18, 2001, pp. 1150-1170.
- [47] "Cloud Droplet Probe (CDP) Manual," 2010.
- [48] P.J. Connolly, M.J. Flynn, Z. Ulanowski, T.W. Choullarton, M.W. Gallagher, and K.N. Bower, "Calibration of the Cloud Particle Imager Probes Using Calibration Beads and Ice Crystal Analogs: The Depth of Field," *Journal of Atmospheric and Oceanic Technology*, vol. 24, 2007, pp. 1860-1879.
- [49] J. Brenguier, T. Bourriane, A.A. Coelho, J. Isbert, R. Peytavi, D. Trevarin, and P. Weschler, "Improvements of Droplet Size Distribution Measurements with the Fast-FSSP (Forward Scattering Spectrometer Probe)," *Journal of Atmospheric and Oceanic Technology*, vol. 15, 1998, pp. 1077-1090.
- [50] A.V. Korolev, J.W. Strapp, and G.A. Isaac, "Evaluation of the Accuracy of PMS Optical Array Probes," *Journal of Atmospheric and Oceanic Technology*, vol. 15, 1998, pp. 708-720.
- [51] J. Shen, "Algorithm of Numerical Calculation on Lorentz Mie Theory," *PIERS Online*, vol. 1, 2005, pp. 691-694.
- [52] K. Liou, *An introduction to atmospheric radiation*, Academic Press, 2002.
- [53] E.M. Purcell and C.R. Pennypacker, "Scattering and Absorption of Light by Nonspherical Dielectric Grains," *Astrophysical Journal*, vol. 186, Dec. 1973, pp. 705-714.
- [54] P.C. Waterman, "Symmetry, Unitarity, and Geometry in Electromagnetic Scattering," *Physical Review D*, vol. 3, Feb. 1971, p. 825.
- [55] S. Havemann, A.J. Baran, and J.M. Edwards, "Implementation of the T-matrix method on a massively parallel machine: a comparison of hexagonal ice cylinder single-scattering properties using the T-matrix and improved geometric optics methods," *Journal of Quantitative Spectroscopy and Radiative Transfer*, vol. 79-80, 2003, pp. 707-720.
- [56] M.I. Mishchenko, J.W. Hovenier, and L.D. Travis, *Light scattering by nonspherical particles*, Academic Press, 2000.
- [57] K. Muinonen, "Scattering of light by crystals: a modified Kirchhoff approximation," *Applied Optics*, vol. 28, 1989, pp. 3044-3050.
- [58] P. Yang and K.N. Liou, "Geometric-optics integral-equation method for light scattering by nonspherical ice crystals," *Applied Optics*, vol. 35, Nov. 1996, pp. 6568-6584.
- [59] E. Hesse and Z. Ulanowski, "Scattering from long prisms computed using ray tracing combined with diffraction on facets," *Journal of Quantitative Spectroscopy and Radiative Transfer*, vol. 79-80, 2002, pp. 721-732.
- [60] E. Hesse, "Modelling diffraction during ray tracing using the concept of energy flow lines," *Journal of Quantitative Spectroscopy and Radiative Transfer*, vol. 109, May. 2008, pp. 1374-1383.
- [61] E. Hesse, A.J.M. Clarke, Z. Ulanowski, and P.H. Kaye, "Light scattering by ice crystals modelled using the Ray Tracing with Diffraction on Facets method," *Geophys. Res. Abstracts*, vol. 9, 2007.
- [62] R.D. Prosser, "The interpretation of diffraction and interference in terms of energy flow," *International Journal of Theoretical Physics*, vol. 15, Mar. 1976, pp. 169-180.
- [63] E. Hesse, D. Mc Call, Z. Ulanowski, C. Stopford, and P. Kaye, "Application of RTDF to

- particles with curved surfaces,” *Journal of Quantitative Spectroscopy and Radiative Transfer*, vol. 110, 2009, pp. 1599-1603.
- [64] R. Cotton, S. Osborne, Z. Ulanowski, E. Hirst, P.H. Kaye, and R.S. Greenaway, “The ability of the Small Ice Detector (SID-2) to characterise cloud particle and aerosol morphologies obtained during flights of the FAAM BAe-146 research aircraft,” *Journal of Atmospheric and Oceanic Technology*, vol. preprint, Aug. 2009, pp. 0000-0000.
- [65] P. R. Field, A. J. Heymsfield, and A. Bansemer, “Shattering and Particle Interarrival Times Measured by Optical Array Probes in Ice Clouds,” Feb. 2010.
- [66] Z. Ulanowski, “personal communication.”
- [67] P.H. Kaye, E. Hirst, R.S. Greenaway, Z. Ulanowski, E. Hesse, P.J. DeMott, C. Saunders, and P. Connolly, “Classifying atmospheric ice crystals by spatial light scattering,” *Opt. Lett.*, vol. 33, 2008, pp. 1545–1547.
- [68] N.J. Bacon and B.D. Swanson, “Laboratory Measurements of Light Scattering by Single Levitated Ice Crystals,” *Journal of the Atmospheric Sciences*, 2000, pp. 2094-2104.
- [69] Z. Ulanowski, E. Hesse, P.H. Kaye, and A.J. Baran, “Light scattering by complex ice-analogue crystals,” *J. Quantit. Spectr. Rad. Transf.*, vol. 100, 2006, pp. 382-392.
- [70] Z. Ulanowski, E. Hesse, P.H. Kaye, A.J. Baran, and R. Chandrasekhar, “Scattering of light from atmospheric ice analogues,” *Journal of Quantitative Spectroscopic Radiative Transfer*, 2003, pp. 1091-1102.
- [71] A.J. Clarke, E. Hesse, Z. Ulanowski, and P.H. Kaye, “A 3D implementation of ray tracing combined with diffraction on facets: Verification and a potential application,” *Journal of Quantitative Spectroscopy and Radiative Transfer*, vol. 100, 2006, pp. 103-114.
- [72] Z. Ulanowski, “Ice analog halos,” *Applied Optics*, vol. 44, 2005, pp. 5754-5758.
- [73] W. Wong, W. Siu, and K. Lam, “Generation of moment invariants and their uses for character recognition,” *Pattern Recognition Letters*, vol. 16, Feb. 1995, pp. 115-123.
- [74] Y. Zhu, L. De Silva, and C. Ko, “Using moment invariants and HMM in facial expression recognition,” *Pattern Recognition Letters*, vol. 23, Jan. 2002, pp. 83-91.
- [75] S. Cadieux, F. Michaud, and F. Lalonde, “Intelligent system for automated fish sorting and counting,” *Intelligent Robots and Systems, 2000. (IROS 2000). Proceedings. 2000 IEEE/RSJ International Conference on*, 2000, pp. 1279-1284 vol.2.
- [76] S.A. Dudani, K.J. Breeding, and R.B. McGhee, “Aircraft Identification by Moment Invariants,” *Computers, IEEE Transactions on*, vol. C-26, 1977, pp. 39-46.
- [77] P.H. Kaye, J.E. Barton, E. Hirst, and J.M. Clark, “Simultaneous Light Scattering and Intrinsic Fluorescence Measurement for the Classification of Airborne Particles,” *Applied Optics*, vol. 39, Jul. 2000, pp. 3738-3745.
- [78] Ming-Kuei Hu, “Visual pattern recognition by moment invariants,” *Information Theory, IRE Transactions on*, vol. 8, 1962, pp. 179-187.
- [79] J. Flusser, “On the independence of rotation moment invariants,” *Pattern Recognition*, vol. 33, Sep. 2000, pp. 1405-1410.
- [80] J. Flusser and T. Suk, “Rotation Moment Invariants for Recognition of Symmetric Objects,” *Image Processing, IEEE Transactions on*, vol. 15, 2006, pp. 3784-3790.
- [81] James W. Cooley and John W. Tukey, “An Algorithm for the Machine Calculation of Complex Fourier Series,” *Mathematics of Computation*, vol. 19, Apr. 1965, pp. 297-301.
- [82] Z. Ulanowski, “Characterization of Small Ice Crystals Using Frequency Analysis of Azimuthal Scattering Patterns,” Jun. 2007.
- [83] Z. Ulanowski, J. Bailey, P.W. Lucas, J.H. Hough, and E. Hirst, “Alignment of atmospheric mineral dust due to electric field,” *Atmospheric Chemistry & Physics*, vol. 7, Dec. 2007, pp. 6161-6173.
- [84] M. Schnaiter, “The Ice Cloud Characterisation Campaign HALO-02,” May. 2009.

- [85] R. Schön, M. Schnaiter, Z. Ulanowski, S. Benz, O. Möhler, S. Vogt, R. Wagner, and U. Schurath, "(submitted) PHIPS – A novel instrument for ice particle imaging," *Journal of Atmospheric and Oceanic Technology*.
- [86] S.A. Self, "Focusing of spherical Gaussian beams," *Applied Optics*, vol. 22, Mar. 1983, pp. 658-661.